Laser-based temperature pressure & species concentration measurements in combusting and non-combusting flows

A thesis submitted for the degree of Doctor of Philosophy

Andrew Luers



Lady Margaret Hall, University of Oxford

Michaelmas Term 2017

Laser-based temperature, pressure & species concentration measurements in combusting and non-combusting flows

Andrew Luers
Lady Margaret Hall

A thesis submitted in partial fulfilment of the requirement for the degree of Doctor of Philosophy of the University of Oxford.

Michaelmas Term, 2017

Abstract

The development of Laser Induced Thermal Grating Spectroscopy (LITGS) and Degenerate Four-Wave Mixing (DFWM) techniques for measurements in combusting and non-combusting flows is presented. The two techniques are used simultaneously with nitric oxide (NO) as an absorbing species. Signals generated by degenerate and non-degenerate probes are studied for NO in N_2 buffer gas up to 4 bar, using a pulsed laser system to excite the $(0,0)\gamma$-bands of NO at 226.21 nm. Contributions to the signal from scattering off the coherent or population grating of DFWM are distinguished from the scattering off the thermal grating of LITGS.

A systematic study of LITGS in NO is presented as a means of thermometry in air-fed combustion. LITGS signals from combustion-generated NO in a laminar, pre-mixed $CH_4/O_2/N_2$ flame on an in-house constructed slot burner are used to derive temperature values as a function of O_2 concentration and position in the flame at 1 bar and 2.5 bar total pressure. Temperature values, consistent with the calculated adiabatic flame temperature, are derived from averaged LITGS signals over 50-100 single shots at 10 Hz repetition rate in the range of 1600 K - 2400 K with a pressure-dependent uncertainty of $\pm 1.8\%$ at 1 bar to $\pm 1.4\%$ at 2.5 bar. Based on observed signal-to-noise ratios the minimum detectable concentration of NO in the flame is estimated to be 80 ppm for a 5 second measurement time at 10 Hz repetition rate.

LITGS signal shape is used to simultaneously derive pressure and temperature. Pressures are found to match measured gauge pressure well at ambient conditions along the full range of pressures measured from 1 to 5 bar and an extension of the technique is discussed for use in a high pressure combustion environment.

Publications based on this work

Flame thermometry using laser-induced grating spectroscopy of nitric oxide, Luers, A., Sahlberg, AL., Hochgreb, S., Ewart, P. Appl Phys. B (2018) 124:43.

Pressure measurements in combusting and non-combusting gases using laser induced grating spectroscopy. A. Luers, A-L Sahlberg, C. Willman, B.A.O. Williams and P. Ewart, in preparation

"High precision measurement of combustion parameters in flames and engines using Laser Induced Grating Scattering, LIGS" A Luers, A-L Sahlberg, F Foerster, C Willman, B Williams and P Ewart in Light, Energy and the Environment Congress, Boulder, CO. USA 6 - 9 November 2017.

For Amabel and Aston.

Acknowledgements

There are a number of people whom I would like to thank for their support of this work.

First and foremost I thank Professor Paul Ewart for providing the opportunity for me to undertake this research and for his frequent guidance and practical support of the work as well as his enthusiasm and kindness which made it so enjoyable.

I would also like to thank Dr Chris Willman, Dr Anna-Lena Sahlberg and Professor Ben Williams for their support and collaboration, as well as the other members of the group, Dr Shea O'Hagan, Dr Felix Foerster and Dr Henry Northern.

I would like to thank Professor Simone Hochgreb and her group from Cambridge University for their collaboration throughout the project.

Lastly I would like to thank the Engineering and Physical Sciences Research Council and the Oxford Physics Department for their financial support. This work was supported by grant number EP/K02924X/1 from the EPSRC (UK).

Contents

1 Introduction **1**
- 1.1 Combustion in gas turbine engines . . . 1
- 1.2 Thermometry, barometry and species concentration . . . 3
- 1.3 Optical diagnostics . . . 4
- 1.4 Goals and structure of thesis . . . 5

2 Background **8**
- 2.1 Overview . . . 8
- 2.2 Gas turbine engine diagnostics . . . 8
- 2.3 Optical sensing . . . 12
  - 2.3.1 Linear techniques . . . 12
  - 2.3.2 Non-linear techniques . . . 15
- 2.4 Summary . . . 29

3 Physics and applications of DFWM and LITGS **30**
- 3.1 Overview . . . 30
- 3.2 Degenerate Four Wave Mixing (DFWM) . . . 31
  - 3.2.1 Physics of DFWM . . . 31
  - 3.2.2 Non-perturbative DFWM model . . . 33
  - 3.2.3 A computational tool using the BLE model . . . 35
  - 3.2.4 DFWM in combustion temperature and species measurements 38
- 3.3 Laser Induced Thermal Grating Spectroscopy (LITGS) . . . 40
  - 3.3.1 Physics of LITGS . . . 40
  - 3.3.2 LITGS signal analysis . . . 48
  - 3.3.3 LITGS in spectroscopy . . . 51
- 3.4 Summary . . . 53

4 Experimental setup & considerations **54**
- 4.1 Optical layout . . . 55
  - 4.1.1 Excitation beam . . . 55
  - 4.1.2 DFWM and LITGS pump and probe beam arrangement . . 59

4.1.3 Interaction region . . . 60
4.1.4 Signal detection and recording . . . 65
4.2 Laser system selection . . . 66
4.2.1 Optical Parametric Oscillator (OPO) . . . 66
4.2.2 Dye laser . . . 67
4.2.3 Dye selection . . . 69
4.3 Target species: nitric oxide . . . 71
4.4 Experimental combustion environment . . . 72
4.5 Alignment and operation . . . 74
4.6 Summary . . . 76

5 Combined DFWM and LITGS in nitric oxide 77
5.1 Introduction . . . 77
5.2 Background . . . 78
5.3 DFWM and LITGS contributions to signal . . . 79
5.3.1 Saturation of DFWM process . . . 82
5.3.2 Combined DFWM & LITGS and qualitative simulations . . . 85
5.4 Combined DFWM and CW LITGS . . . 91
5.5 Effect of DFWM probe on CW LITGS signal . . . 92
5.6 Summary . . . 95

6 LITGS in nitric oxide in non-combusting gas mixtures 97
6.1 Introduction . . . 97
6.2 LITGS thermometry in NO . . . 98
6.2.1 Derived temperatures from FFT of LITGS signal . . . 98
6.2.2 Derived temperature in NO in an optical cell . . . 99
6.2.3 Temperature measurement uncertainty . . . 100
6.3 NO species concentration effects on LITGS signal . . . 109
6.4 LITGS barometry in NO . . . 112
6.4.1 Pressure derived from fitted model . . . 112
6.4.2 Pressure derived from signal decay . . . 116
6.5 Summary . . . 119

7 LITGS in nitric oxide in a combusting flow 122
7.1 Introduction . . . 122
7.2 Flame temperature measurements . . . 123
7.2.1 Measurement error . . . 123
7.2.2 NO concentration effects on signal . . . 130
7.2.3 Flame barometry . . . 132
7.3 Summary . . . 135

8 Conclusions and future work **137**
8.1 Summary and conclusions 137
8.1.1 Simultaneous DFWM and LITGS 137
8.1.2 Temperature, pressure and concentration measurements in NO 138
8.2 Future work 139
8.2.1 Temperature calibration and further error reduction 139
8.2.2 High repetition rate measurements 140
8.2.3 Multipoint measurements 140
8.2.4 Pressure and concentration measurement 140

List of Abbreviations

A&L Abrams and Lind

ASE Amplified spontaneous emission

BBO Beta Barium Borate

BLE Bratfalean Lloyd and Ewart

BPG Backward pump geometry

CARS Coherent anti-stokes Raman scattering

DFWM Degenerate four-wave Mixing

DNI Direct numerical integration

DPSS Diode-pumped solid state

EPA Environmental Protection Agency

ERE-CARS Electronically resonantly enhanced coherent anti-stokes Raman scattering

FFT Fast Fourier Transform

FPG Forward pump geometry

HAB Height above burner

ICLAS Intra-cavity laser absorption spectroscopy

KDP Potassium dideuterium phosphate

LIEGS Laser-induced electrostrictive grating spectroscopy

LIF Laser induced fluorescence

LITA Laser induced thermal acoustics

LITGS Laser-induced thermal grating spectroscopy

MUMAS Multi-mode absorption spectroscopy

OPO Optical Parametric Oscillator

PMT Photomultiplier Tube

ppm Parts per million

PS Polarization spectroscopy

Re Reynolds number

SFG Sum Frequency Generation

SHG Second harmonic generation

SLM Single longitudinal mode

TDLAS Tunable diode laser absorption spectroscopy

Chapter 1

Introduction

1.1 Combustion in gas turbine engines

Since the industrial revolution, combustion, used to power transportation, heating, lighting, movement of water, and digital communications, has become an essential enabler of much of daily life. Today, combustion of organic materials is responsible for over 60% of electricity production(15 TWh), with an even higher percentage used in home heating, and combustion is responsible for nearly 99% of transportation via cars, shipping, and air travel [1]. The welcome invention and rapidly increasing deployment of non-combusting sources of renewable energy and electric vehicles promises to somewhat reduce our dependence on combustion and the harmful emissions that go along with it. However during that transition and even beyond it, combustion will continue to play a large role in our society. Today renewable energy constitutes only about 15% of total electricity production, much of that from hydropower, and is expected to grow to about 30% by 2050 according to the

US Energy Information Administration (EIA) [1]. Furthermore, the energy mix of the future envisions renewable combustion processes - the burning of biomass and hydrogen - as a way to provide flexibility to grid operators and when high energy density is required - e.g. for air transportation.

Modern gas turbine engines contribute over 20% of global electricity production and are the means of propulsion for all but the very lightest aircraft . Their use is expected to grow by $1.5 - 3\%$ annually for the next decade. In developing countries such as India, where energy generation is doubling in capacity every 5-6 years, the growth in the adoption and use of gas turbine engines is even more dramatic [2]. The ubiquitous role of combustion, and gas turbines in particular, in our society makes it important to understand these combustion processes so that improvements can continue to be made to performance efficiency and harmful emissions reduction and to enable the use of more sustainable fuels.

In the field of gas turbines, a particular problem is that of acoustic instabilities and nitric oxide reduction. There is currently a tradeoff between safe operation and avoiding these instabilities and the formation of harmful nitric oxides* which cause health and environmental problems. To break this tradeoff a careful study of the dynamics within combustors must be made so that designers can achieve safe operations at operating conditions which reduce NO_x.

*referred to as NO_x and consisting of NO and NO_2

1.2 Thermometry, barometry and species concentration

Measurement of parameters such as temperature, pressure and species concentration are critical to understanding the chemical reactions that occur in combustion. Temperature is important, for example, for determining reaction rates and thus production of post reaction species. In combustion processes where mechanical work in some form is the desired output, relative temperatures of inputs and outputs define the thermodynamic efficiency. Heat transfer to surfaces is often an important consideration and temperature influences the flow dynamics within a system. Measurements of pressure are important as many industrial combustion processes operate over a range of pressures and dangerous instabilities can materialise as pressure fluctuations. Species concentration measurements are useful in validating combustion models and ensuring emissions requirements are met.

Traditionally, measurements of these parameters have been done with physical sensors which are able to measure averages of the bulk properties at boundaries. For example, in the case of combustion flows, wall based hot-film sensors or static pressure gauges or exit based total pressure transducers are used to make measurements of these parameters. These techniques are insufficient for many modern needs. Physical probes have survivability limitations in harsh environments and often perturb the parameters they are measuring. In addition, they often lack accuracy, precision and spatial and temporal resolution to provide the information needed to better understand and control combustion processes.

1.3 Optical diagnostics

Optical based sensors have attractive benefits and have made significant contributions to combustion diagnostics [3, 4]. Typical optical techniques involve measuring light emissions from a combustion process or, since the advent of lasers, measuring light absorption or scattering. A special field of optical diagnostics uses non-linear optics which, while more challenging to setup and operate than other optical techniques, has further benefits that will be described in detail in the next chapter.

While these techniques have been successfully applied in combustion environments, there continue to exist many combustion problems which still require more work. One example of this, and the ultimate aim toward which this work is directed, is the precise measurement of temperature in a turbulent combustion flow within a gas turbine engine. Measurements are required of temperature uniformity around the nozzle guide vanes, an important measure of gas turbine performance [5–7]. The direct measure of temperature amplitude fluctuations are also needed as they can provide a measure of the onset of hot spots, called entropy spots, as a source of pressure fluctuations that lead to acoustic instabilities [8–10]. Because these occur over a range of pressures and take the form of pressure gradients within the flow, the simultaneous capture of pressure information would be useful. Likewise there is a need to link temperature to species and obtain an estimate of instantaneous NO species concentration. Collectively, these measurements will provide statistical information required by designers to improve gas turbine designs for stability and reduced NO emissions.

A step along the way is to be able to measure local temperature to sufficient

precision to identify entropy spots in the flow and provide a measurement tool to study these effects in laboratory conditions that could then be extended to turbulent flames and engines. NO is used as the target measurement species due to the link between NO concentration and temperature but also as it is a combustion species and so readily available, in contrast to more traditional seeding techniques which would introduce a special 'tracer' as the target species. In the high temperatures of a gas turbine engines, these tracers would be consumed in the combustion process. NO also has the advantage of being a relatively stable combustion product, compared with radicals such as OH.

1.4 Goals and structure of thesis

The goal of the present work is to develop a measurement approach for use in a combustion chamber where regions of high temperature propagate downstream in a way that thermoacoustic instabilities could be created by such perturbations. These measurements are made by way of a combustion species (NO) that is linked to the thermoacoustic instabilities by temperature. We use two non-linear diagnostic techniques in the process, Degenerate Four-Wave Mixing (DFWM) and Laser-Induced Thermal Grating Spectroscopy (LITGS) and provide a deeper understanding of the interaction between them and indication of how they might be used together. The structure of this thesis is the following:

- Ch 2: background of optical diagnostics and rationale for selection of the techniques employed in this work, DFWM and LITGS.
- Ch3: a brief description of the physics of DFWM and LITGS and a review

of relevant previous work upon which the present study builds, including advancement of work on a non-perturbative DFWM model.

- Ch 4: a discussion of the experimental setup that was built as part of this effort and to which the rest of the work will frequently refer and experimental considerations important to the success of the work.

- Ch 5: a demonstration of the transition from a DFWM-dominated to a LITGS-dominated effect and identification of regimes in which both effects are present. These effects are rendered visible and details are provided beyond what has been seen before and it is demonstrated how these techniques could be used to complement one-another.

- Ch 6: temperature measurements are made using LITGS in NO in a non-combusting environment as a proof of concept and calibration for flame-based measurements. Temperature precisions are explored as well as the ability to simultaneously extract pressure and NO species concentration information from the signal.

- Ch 7: an extension of LITGS in NO to a pressurised flame environment is demonstrated and the ability to measure temperature to a high degree of precision as well as identify the effects of temperature on NO concentration and the ability to extract pressure information from flame signals.

- Ch 8: a summary of the findings and discussion of what will follow and how this work complements other on-going work to build toward a tool to achieve high-speed, multi-point highly precise and spatially resolved temperature

measurements in the turbulent flow of a gas turbine combustor.

Chapter 2

Background

2.1 Overview

This chapter begins by explaining the need for optical sensing in gas turbine engine diagnostics as well as the requirements of a diagnostic device. A brief overview of linear and non-linear techniques is presented and the advantages of non-linear techniques for the present application are discussed. Finally, degenerate four-wave mixing (DFWM) and laser-induced thermal grating spectroscopy (LITGS) are introduced as two methods which separately and combined can meet many of the requirements for gas turbine combustion diagnostics and the goals of this research.

2.2 Gas turbine engine diagnostics

A key design parameter for combustors of gas turbine engines is the prevention of thermoacoustic instabilities (see for example [11]). Thermoacoustic instabilities occur in a combustion environment via a resonant coupling between thermal events

and natural acoustic modes in a confined chamber. An unsteady heat release can drive acoustic waves within the chamber. These waves reflect and influence their own source, the heat release. This regenerative mechanism can lead to positive feedback, ultimately causing destructive instability within the chamber in the form of exponentially growing pressure fluctuations. Lord Rayleigh was the first to describe a criteria for the onset of acoustic instabilities as:

> If heat be periodically communicated to, and abstracted from, a mass of air vibrating in a cylinder bounded by a piston, the effect produced will depend upon the phase of the vibration at which the transfer of heat takes place. If heat be given to the air at the moment of greatest condensation or be taken from it at the moment of greatest rarefaction, the vibration is encouraged [12].

In gas turbine engines, these instabilities result in growing heat release, pressure oscillations and vibrations. These in turn lead to any of the following:

- thrust oscillations
- increased engine noise
- severe vibrations which interfere with control-system operations
- enhanced heat transfer and thermal stresses to combustor walls
- oscillatory mechanical loads that result in fatigue of system components
- flame blowoff or flashback
- premature component wear

The problem of acoustic instabilities is exacerbated in modern, lean, pre-mixed gas turbines which are designed to reduce NO_x emissions. NO_x are harmful pollutants which have been identified as a leading cause of acid rain, ozone depletion,* and smog, and can lead to pulmonary oedema if inhaled. As a result, they have been classified as extremely hazardous substances by the U.S. Environmental Protection Agency (EPA) and other regulatory bodies and subject to strict regulations.†

There remains regulatory pressure to continue to reduce NO_x emissions levels in modern gas turbine combustors. These are therefore being designed to produce a leaner fuel-air mixture than is typical in a conventional diffusion flame combustor. The high airflow reduces flame temperature and in turn the NO_x formation rate - which is an exponential function of temperature. For example, a local change of $50K$ can lead to a change of 70% in thermal NO formation rates at typical combustion temperatures [14]. However these combustors are, as a result, more sensitive to fuel flow rate and therefore to pressure fluctuations [15]. To address these competing priorities of emissions reduction and eliminating instabilities, there has been a growing interest to understand the physics involved and to mitigate the negative effects through design as well as passive and active feedback control. For example, work is being done to better understand the indirect combustion noise in which hot gas spots (or entropy spots) are produced and convect and lead to the production of acoustic waves as they travel through turbine vanes or exhaust nozzles and which may then couple with the acoustics of the system [10]. These

*For example, NO can upset the balance of O_3 formation when O_3, which is a slow formation process anyway, is combined with NO to form NO_2 and O_2.

†In 1973 the EPA published the first emissions standards for NO_x in terms of maximum allowable output per unit of thrust per hour in a standard approach-landing-taxi-taxi-takeoff cycle[13].

unsteady indirect noise effects are being simulated via the creation of synthetic entropy spots in a tube [16].

In the example cited above, as well as more broadly to validate emission prediction models and inform design parameters, precise spatially and temporally resolved temperature statistics are critical. The onset of instabilities and the formation of NO_x are highly non-linear processes and require statistical information on deviations from the mean in order to make accurate predictions. In addition to precise temperature measurements, ideally, measurements of the associated local pressure fluctuations would be captured, to help further characterise acoustic perturbations, as well as NO formation rates.

However, sufficiently reliable statistical temperature information, and associated pressure and species concentration data is unavailable today. Traditional diagnostic tools for measuring temperature, pressure or species concentration have limitations which make them inadequate. Traditional combustion measurement devices include, for example, thermocouples, pressure transducers and exhaust gas analysers. When used in-situ, these physical probes interfere with the region being measured and alter the parameter under investigation - for example thermocouples introduce a heat loss mechanism into the flow. Current methods for temperature measurements in gas turbine combustors with precision in the region of 10%, corresponding to uncertainties of 200 K at combustion temperatures of 2000 K, lack the required precision. In addition, probe lag times are insufficient to provide the required temporal resolution. For pressure measurements, traditional probes are typically wall- or exit-mounted and provide averaged data across the combustion chamber, thus lacking the spatial resolution required. It is not possible to measure NO

formation with existing probes [17].

The ideal measurement tool would provide the following: temperature measurements with precisions of 1% or better and with spatial resolutions of a few millimetres* and temporal resolution on the microsecond scale, while being non-intrusive to the flow and capable of probing different regions within the flow. Ideally, measurements would also provide instantaneous pressure and NO species concentration information as well.

Optical techniques, especially non-linear optical techniques, hold promise to deliver these requirements [18]. These techniques are considered below, with emphasis on their potential to provide the necessary temperature information to better characterise combustor instabilities, while also considering the effects of pressure and concentration changes on temperature measurements as well as their potential to simultaneously provide pressure and species concentration information.

2.3 Optical sensing

2.3.1 Linear techniques

Optical sensing techniques provide a direct, quantitative measure of certain properties of a gaseous sample when light from a source interacts with a medium of interest and is then detected by an appropriate sensing device.

Optical sensing takes advantage of the fact that atomic and molecular species have a characteristic absorption and emission spectrum. This provides the possibility

*turbulent gases may contain unmixed hot and cold gases on the length scale of a few millimetres or the interaction region may include a flame front with burned and unburned gases

of high-selectivity of a target species. These techniques can be nearly instantaneous as they are limited only by the speed of light and any delay in the associated electronics. They are also non-invasive and can provide measurements in harsh environments that would otherwise not be survivable by physical probes.

In the field of optical diagnostics, a distinction is typically made between linear and non-linear techniques. In linear techniques the signal is proportional to the first power of the electric field in the wave, i.e. linearly proportional. Typically these techniques involve the absorption or scattering of the incident photon.

In the field of combustion diagnostics, a number of techniques have been employed which apply these basic principles. These can be grouped into:

- Absorption techniques, i.e. tunable diode laser absorption spectroscopy (TDLAS), intra-cavity laser absorption spectroscopy (ICLAS), multi-mode absorption spectroscopy (MUMAS)
- Emission techniques, i.e. laser-induced fluorescence (LIF) and variants, Chemiluminescence
- Scattering Techniques, i.e. Rayleigh scattering, Raman scattering

In absorption techniques, the Beer-Lambert law* is applied directly to estimate species concentration. Techniques like tuneable diode laser absorption spectroscopy (TDLAS) scan a diode laser over a spectral range within a flame that corresponds to the transitions (or "fingerprint") of a target species and can be used to measure

*The Beer-Lambert law relates the transmittance or absorbance of a sample to the concentration of an absorbing species via the ratio of transmitted to incident intensity at wavelength corresponding to a known transition of an absorbing species in the flame and its optical depth and absorbance.

relative temperature. This fingerprint will change as there is a thermal redistribution of population, since the distribution of population amongst levels in a molecule is strongly affected by temperature, according to the Boltzmann distribution.* The primary benefits of absorption techniques, in addition to those common to all optical techniques described above, is that they are simple to setup and operate. However they have limited spatial resolution along the propagation direction and therefore limited usefulness in flames that have important heterogenous characteristics (density and concentration), as is the case when studying entropy spots.

Emissions techniques, like chemiluminescence, involve the measurement of emitted photons from species that are present in an excited state and emit radiation as they fall to the electronic ground state. In laser induced fluorescence (LIF), a tracer species is introduced into the measurement region and a laser tuned to a resonance of that species. The spontaneously emitted photons (fluorescence) of that species are measured as the molecule returns to the ground state.

Spontaneous Raman scattering is an inelastic process in which energy is transferred from an incident photon to a molecule and the emitted photon is shifted ("Stokes" shifted or "anti-Stokes" shifted). The amount of scattered light is linearly proportional to the number density of the scattering species. By tuning to a resonance transition (resonant Raman scattering) the signal is strengthened and, experimentally, this is similar to LIF.

Fluorescence techniques have been successfully used in combustion environments, as have resonance Raman scattering [3, 4]. These techniques, however, as with any that rely on a direct measurement of intensity, are susceptible to beam steering,

*$N_2/N_1 = e^{-\frac{E_2-E_1}{kT}}$ where N_1 and N_2 are population densities in two energy levels, E_1 and E_2, k is the Boltzmann constant and T is the temperature

window fouling or unknown local quenching effects, which are more pronounced as pressure increases, and make signal interpretation difficult. Since the emitted or scattered light is incoherent and radiated into a 4π solid angle, signal collection requires significant optical access and suffers from signal-to-noise challenges. Both fluorescence and Raman techniques require very powerful lasers and eliminating background becomes difficult.

Linear optical techniques have many advantages in that they are non-invasive, provide near-instantaneous measurements, are linearly dependent on species concentration and are relatively simple to calibrate. However their limitations, including the requirement for clean, gaseous flames, significant optical access, low signal-to-noise ratios, sensitivity to laser intensity fluctuations and signals that are often difficult to interpret quantitatively owing to unknown effects of collisional quenching, make them less suitable to all combustion applications, and the harsh, turbulent environment of gas turbine combustors, in particular. For more on linear techniques, see for example [3, 4, 20].

Non-linear techniques, another class of optical sensing which produce an inherently coherent signal, are better suited to the combustion problems this research seeks to address. The remainder of this chapter will therefore focus on a review of relevant non-linear techniques with potential for thermometry, barometry and species concentration in a harsh, turbulent combustion environment.

2.3.2 Non-linear techniques

The spectroscopic techniques employed in this research are part of a general class of four-wave mixing techniques [3, 21]. Four-wave mixing describes a non-linear optical

processes in which three incident photons interact to generate a signal photon via an induced third-order polarisation of the medium. Where the beam geometries satisfy a phase matching condition, the contributions to the signal constructively interfere to produce a coherent signal. This signal propagates as a laser-like beam which can be collected far from the combustion region and from which information of temperature, species concentration, pressure or other properties of the probed medium can be derived.

While non-linear techniques are more complex to setup and interpret, their coherent signal means they have a far more modest need for optical access and higher signal-to-noise ratios. These techniques are spectroscopic in that signal intensity is greatly enhanced in a resonant transition of the medium and this allows signals to be generated even for small lower state populations, typical of radical species populations in flames.

The interaction of multiple photons in a medium simultaneously in non-linear optical diagnostic techniques is described by the higher order terms of the induced polarisation of a medium. When an intense electric field induces polarisation in a medium, the expression for polarisation may be expanded as a power series in electric field to include higher order terms:

$$P = \epsilon_0 X^{(1)}(\omega) E_1(\omega_1) + \epsilon_0 X^{(2)}(\omega) E_1(\omega_1) E_2(\omega_2) + \epsilon_0 X^{(3)}(\omega) E_1(\omega_1) E_2(\omega_2) E_3(\omega_3) + ... \tag{2.1}$$

X is the susceptibility tensor and defines the complex refractive index of the medium. X depends on frequency and decreases by many orders of magnitude

for quadratic and higher order terms and thus higher order terms can usually be ignored. However X becomes large when the incident electric field corresponds to a natural resonance frequency of the medium. Thus, in the presence of an intense electric field from a laser tuned to a resonance of the medium (as is the case in resonant four-wave mixing spectroscopy) these higher order terms become significant.

In centro-symmetric media,* the second order term is zero, leaving the 3rd order term as the first non-zero, non-linear term and so we can express the nonlinear polarisation as:

$$P_{NL}(\omega_4) = \epsilon_0 X^{(3)}_{ijkl}(\omega) E_1(\omega_1) E_2(\omega_2) E_3(\omega_3) \tag{2.2}$$

Thus, a polarisation may be created, oscillating at frequency ω_4 in response to driving fields at three different frequencies ω_1, ω_2, ω_3. This can be thought of as one field acting on a medium whose refractive index is being modified by the action of the two other fields.

The process is governed by the conservation of energy and of momentum since in most four wave mixing techniques there is no transfer of energy and momentum to the medium. Conservation of energy is achieved when the sum of the energies (and thus frequencies) of photons exchanged between the four fields is zero. This implies that the polarisation frequency ω_4 can take a range of values:

$$\omega_4 = \pm\omega_1 \pm \omega_2 \pm \omega_3 \tag{2.3}$$

*All media which have an inversion symmetry, including all gases

Conservation of momentum is required in order to form a propagating wave, as the induced electric dipoles must form a phased array such that their radiation constructively interferes. The wave vectors must therefore meet the condition below, referred to as phase matching, and this implies that the geometry of the beam alignment is important.

$$k_4 = \pm k_1 \pm k_2 \pm k_3 \tag{2.4}$$

Below is a brief comparison of four non-linear spectroscopy techniques that have been developed from this basic physics along with their benefits and limitations. Figure 2.1 shows an illustration of the energy level diagrams associated with each technique. Particular attention is given to Coherent Anti-Stokes Raman Scattering, CARS, as the main alternative to the techniques employed in this research, DFWM and LITGS. For a more detailed discussion of these and other non-linear techniques, there are a number of detailed reviews, for example [3, 22].

Coherent Anti-Stokes Raman Scattering (CARS)

Coherent Anti-Stokes Raman Scatting (CARS) was developed in 1965 and used in combustion diagnostics in the early 1970's and extensively since [23]. As a result it is an established and extensively applied technique and a number of complete reviews have been written [3, 22, 24]. Here a brief summary will be given for convenience and to demonstrate the rationale for choosing alternative techniques for the present work.

The CARS technique uses laser sources of different wavelength to produce a pump beam (ω_1), a Stokes beam (ω_2) and a second pump beam (ω_3). The beams

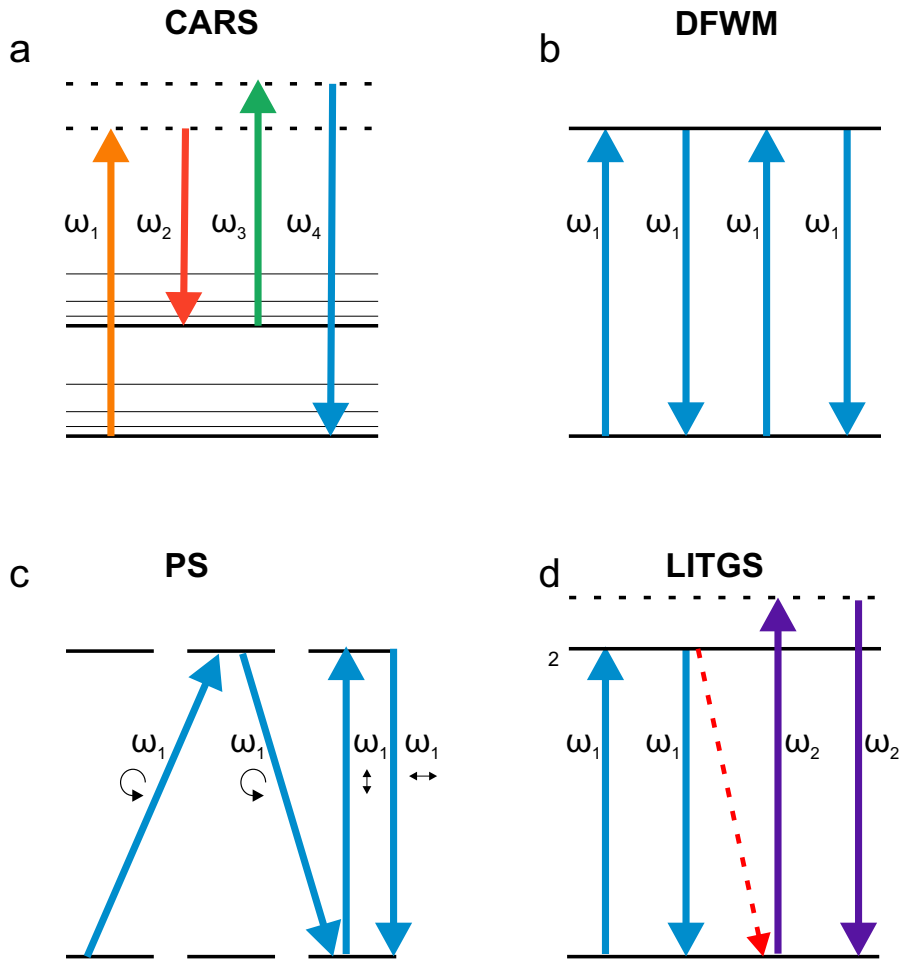


Figure 2.1: Energy level diagrams for non-linear optical diagnostic techniques discussed in this chapter showing radiative (solid lines) and non-radiative (dashed lines) transitions. The line colour and ω indicate frequency. Lines with arrows indicate polarisation.

interact within a medium to produce a signal at frequency $\omega_4 = \omega_1 - \omega_2 + \omega_3$, which is referred to as the anti-Stokes frequency. Traditional CARS is a two-photon technique so no single beam is resonant with a transition. Instead, the difference in frequency of two of the incident beams corresponds to a vibrational or rotational "Raman" transition.

The phase matching condition, described above for all parametric four-wave

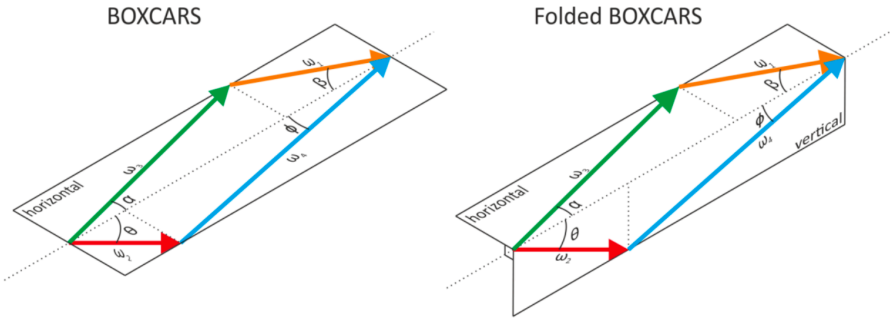


Figure 2.2: Illustration of BOXCARS and folded BOXCARS geometries for CARS where ω and the line colours represent frequency.

mixing techniques, must be met and can be achieved in multiple geometric configurations. Most common is the BOXCARS [3] or the folded BOXCARS [25] geometries, illustrated in Figure 2.2, as they result in a localised probe volume, and thus good spatial resolution.

Conceptually, the process can be described as three beams creating a third-order polarisation in the medium which radiates the signal beam. Alternatively it can be understood as two beams populating a rotational or vibrational level at their difference frequency, followed by scattering of the third beam off the scattered molecules resulting in a signal beam.

Scanning the frequency of the Stokes beam generates a CARS spectrum with intensity peaks corresponding to frequencies of rotational or vibrational* transitions in target species.† The relative intensities are proportional to thermal populations and so can be used to derive temperature by fitting of a complex theoretical spectrum. In addition to temperature, number density can be derived from signal

*vibrational energy levels have larger energy gaps and therefore smaller thermal populations above the ground state as compared with rotational levels making vibrational CARS more appropriate for flame thermometry

†Single-shot measurements are also possible with a broadband Stokes beam.

strength and therefore provide species concentration information.

Conventional CARS is a non-resonant process and so makes use of virtual levels in order to enable the transitions. The low probability of such transitions due to low effective cross section and the fact that signal amplitude is proportional to number density squared, means that a signal is usually only observed when the number density of the target species is greater than 1% in practice. This means the technique is usually applied to major species in a flame and is inappropriate for minor species such as OH, CO or NO. Resonant enhancement of the signal, however, can be achieved when the pump or Stokes frequency is resonant with an electronic transition, exciting the molecule to a real, rather than virtual level [26, 27]. This is referred to as electronically resonantly enhanced CARS (ERE-CARS) and allows for detection of minor species at ppm levels, however at the expense of a second tunable laser [28, 29].

CARS has been extended from point-measurements described above to 1-D and 2-D measurement volumes. In 1-D CARS a cylindrical lens is used to create a sheet of light for each of the beams that are then crossed to form a linear interaction region [30]. Sandia National Laboratory has developed 2-D CARS imaging by applying femto-second lasers and again crossing pump and stoke beam 'sheets' and then applying a large-diameter, phase-matched, probe that generates a CARS signal from each point within the intersection region. The signal is dispersed with a diffraction grating and imaged onto a CCD camera [31–34].

The advent of femtosecond lasers and the very high intensity pulses they produce result in improved signal-to-noise ratio when applied in CARS. The high repetition rates allow for time-resolved temperature and number density measurements bey-

ond what is possible with nanosecond lasers and since collisions are typically on picosecond timescales they are able to generate signals essentially independent of collisions rather than account for them through complicated modelling [35]

ERE-CARS has been used extensively to study the NO molecule with concentration measurements demonstrated and a detection limit of 100 ppm [28, 36]. Lucht et al measured NO concentrations in hydrogen/air flame and in a sooting acetylene/air flame and later in a hydrogen/air counter-flow flame in which they achieved measurements down to concentrations of 50 ppm and good agreement with predicted NO concentrations [29].

CARS has also been used extensively in flames to measure temperature. Initially, measurements accuracy was limited by computing power which is required for accurately modelling and fitting of spectra. As computing power evolved and models were improved by Dreier, Palmer and others, accuracies were improved [37]. Single shot accuracies of $2-5\%$ have been shown [38] and precisions of 3% [4, 39]. Precision is limited by spectral noise on the Stokes laser arising from mode intensity fluctuations. This was overcome by use of a modeless laser [40].

CARS has been applied in internal combustion engines for high precision temperature and number density measurements in O_2 and N_2 or using fuel-based tracers [41, 42]. CARS has also been applied for temperature measurements in gas turbine engines showing the feasibility of the technique is such a harsh environment [43].

CARS offers a number of advantages over physical probes and linear optical measurement techniques. The coherent signal beam means a high signal-to-noise

ratio which has meant it can be applied in sooting flames* or other harsh environments. The detection of a signal at shorter wavelengths than the pump wavelength helps to avoid possible LIF interference. Spatial resolution, which is important in engine measurements, is determined by the size of the interaction volume. In CARS the interaction volume is defined by the crossing angle and beam diameter and thus millimetre size interaction regions are possible.

There are a number of important disadvantages of the CARS technique, however. Traditional CARS is limited to major species. For minor species detection, the use of ERE-CARS is required which is challenging and expensive to implement as all excitation lasers need to be tuned to resonance. Temperatures and concentration derivations depend on accurate modelling of the CARS spectra which is complex and time consuming. And the demands for precision in modern gas turbine measurements are beyond even that afforded by CARS.

The techniques below overcome these challenges. Polarisation spectroscopy and degenerate four wave mixing achieve the sensitivity of CARS without some of the complications and laser induced thermal grating spectroscopy achieves higher precisions temperature measurements more easily.

Polarization Spectroscopy (PS)

Polarisation Spectroscopy (PS) uses only two beams - a strong pump and a weak probe. Two photons are taken from the pump beam to drive the four-wave mixing interaction. The probe beam passes through a linear polariser prior to intersecting with the pump beam and then through a cross-polariser after the intersection

*However signal to noise is a challenge due to strong non-resonant background interference from C_2

and before entering a detector. In the absence of a pump beam, the probe would be blocked from the detector by the cross-polariser. However, when the pump is introduced, which is orthogonally polarised or at a 45° angle to the probe, it produces a birefringence that perturbs the polarisation of the probe beam, resulting in partial transmission through the cross-polariser.

Polarisation Spectroscopy was introduced by Wieman [44] as an improvement upon saturation spectroscopy, offering much better signal-to-noise. PS has been used in flames to measure temperature and minor species concentration of a number of natural flame species including OH and C_2 by frequency scanning narrowband lasers [45]. It has seen applications in temporally resolved single-shot thermometry using a broadband laser source [46] and in two-dimensional flame thermometry [47].

Löfstedt et al used PS in NO to measure temperature in a premixed H_2/N_2O flame based on Boltzmann plotting of the recorded spectra and also demonstrated the possibilities of two-dimensional imaging of the NO molecule distribution [48].

While Polarisation Spectroscopy has some advantages, it has one critical drawback. In a high pressure flame measurement, optical access requires windows into the enclosed combustion region. These windows will experience pressure-induced birefringence themselves, making it difficult to distinguish between the window- and laser-induced birefringence. As a result, PS was not considered an optimal technique for the present work.

Degenerate Four-Wave Mixing (DFWM)

DFWM is a related technique to Polarisation Spectroscopy and an alternative to

resonance CARS but with the advantage of simplicity due to the fact that it can be accomplished with a single tuneable laser source, making it simpler and less costly to setup and operate [3, 22, 49].

In Degenerate Four-Wave Mixing three input beams, at the same (degenerate) frequency, are made to overlap in a suitable medium, oriented such that they mix to generate a signal beam at the same frequency. The beams form a periodic spatial variation in the excited state population of the target molecules, referred to as a population grating. A signal is generated when the frequency is resonant with an electronic transitions of the probed species.

Two geometries are typically employed, a 'forward pump geometry' (FPG) in which all beams propagate in the same direction, converging at a small angle, and a 'backward pump geometry' (BPG) or 'phase-conjugate' geometry, in which the pumps travel in opposite directions and the signal is automatically phase matched (see figure 2.3).* In the BPG, only molecules with zero velocity with respect to the incident beams will be excited. To moving molecules, the incident laser light will be Doppler shifted out of resonance and so these molecules will not contribute to the signal, and therefore the signal will be free of Doppler broadening.† In the FPG, all molecules interact with all three beams and therefore this geometry typically produces stronger signals.

As a resonant technique, DFWM has been successfully used in combustion environments for minor species detection as well as for temperature measurements of which more will be said in the next chapter [50]. Species concentration can

*the angle θ between the probe and pumps can therefore have any value in the BPG configuration

†if the laser linewidth is narrower than the Doppler width.

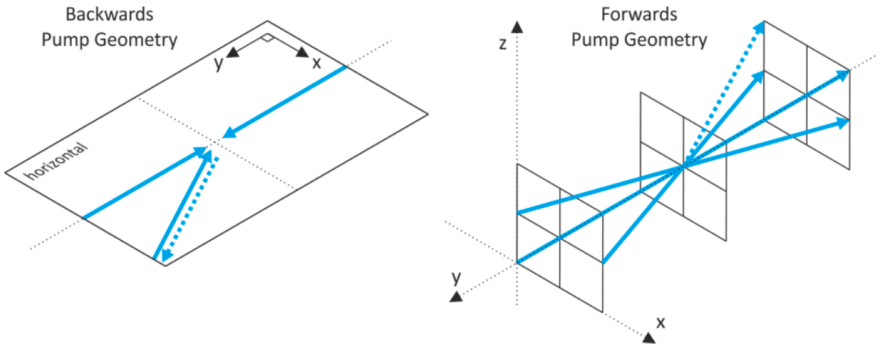


Figure 2.3: Illustration of the forward and backward pump geometries for DFWM.

be derived from signal strength. Temperature (time-averaged) is derived from DFWM by scanning the frequency of the input beams across two or more lines and comparing the relative intensities of these thermally-populated levels [51]. Single-shot measurements can be obtained by using a dual-wavelength laser or using a broadband laser.

The first model for DFWM in absorbing media was given by Abrams and Lind (A&L) [52]. This model took a perturbative, steady-state approach for the phase-conjugate geometry and made a number of simplifying assumptions, including a monochromatic source in an optically thin medium with a two-level atom and a weak (non-saturating) probe. This model, while widely used and effective in many situations, is often insufficient in combustion environments where many of the assumptions of the A&L model do not hold. In particular, a saturating probe is necessary for generating strong signals and minimising the dependance of the

signal on collision rate.* To overcome this limitation, a non-perturbative model was developed by the group [53] which was then translated to a computationally inexpensive approach in this work and is described further in the next chapter.

The benefits of DFWM, beyond the benefits common to all four-wave mixing techniques, are sub-Doppler spectral resolution and excellent spatial and temporal resolution. However, this technique requires a high power (pulsed) narrow line width laser that is frequency tuneable in regions of resonant transition of the species of interest - NO in this case. The technique performs better at low pressure. As pressure increases, molecular collision rates increase. When collisions occur the excited molecule will de-phase or de-excite by inelastic scattering, returning the molecule to the ground state and depositing the energy in the bulk gas of the medium in the form of localised heating and preventing the energy from being redistributed to the signal field and contributing to the DFWM signal.

This pressure-induced effect, while destructive to the DFWM signal, has led to the development of the next and last technique that will be described in this chapter, laser-induced thermal grating spectroscopy.

Laser Induced Thermal Grating Spectroscopy (LITGS)

Laser Induced Thermal Grating Spectroscopy (LITGS) takes advantage of the collisional quenching described above for DFWM. Two degenerate beams are crossed as in DFWM to create an interference pattern within a medium in which there is an electronic resonance with the laser frequency. Collisions rapidly de-populate the upper state, depositing the energy into the bulk gas in the form of heat, creating

*The grating contrast and thus signal strength is optimised with the pump and probe are of equal strength.

local density minima within the fringe spacing as well as launching acoustic waves which travel normal to the grating and sum to create a standing wave. The result is a periodic oscillation in density which decays via thermal diffusion and viscous damping. The density perturbation magnitude, oscillation frequency and grating evolution are dependent on the bulk properties of the medium such as temperature, pressure and species concentration. A third beam can then be scattered off of this modulating grating and record its evolution over time.

A related effect, known as laser-induced electrostrictive grating spectroscopy (LIEGS), occurs from the electric field of the interference pattern inducing a polarisation of the gas molecules which are then displaced, again creating a sudden density modulation and generating acoustic waves [54, 55]. This effect is dominant if the laser frequency is non-resonant with the target molecules but the electric field is of sufficient intensity to induce a polarisation. This effect occurs simultaneous with LITGS when the laser is tuned to a resonance of the target molecule. However it does not make a significant contribution, in this case, compared to the thermal grating produced from absorption, and is easily distinguishable as the signals of the LIEGS effect oscillate at twice the frequency as the LITGS effect.* Further theory and application of LITGS will be discussed in the next chapter.

LITGS offers distinct advantages over the other techniques described. First, with LITGS temperature is derived from the frequency of the signal oscillation. Since frequency can be measured to a high degree of precision this means that the technique can potentially provide a very precise derived temperature. This

*This is due to the fact that the stationary temperature grating is very weak in the case of LIEGS. The stationary temperature grating decays exponentially due to thermal diffusion. So in the case of LITGS the signal appears overlaid a large exponential decay while in LIEGS the signal essentially appears on a zero background.

is in contrast with techniques that rely on a measure of signal strength to derive temperature, which is often complicated by intensity noise or other factors that must be controlled. Second, the LITGS signal amplitude increases with pressure as collisions increase and thus the strength of the thermal grating increases. Since combustion takes place at high pressure within gas turbine engines this is a useful feature.

2.4 Summary

The problem of acoustic instabilities in modern gas turbine engines requires precise in-situ statistics of thermodynamic properties and of temperature in particular. Optical techniques are able to meet many requirements for gas turbine combustion diagnostics where physical probes fall short and non-linear techniques and the coherent signal they produce are ideally suited for this problem. LITGS in particular is the most promising technique for our primary goals given its industry-leading precision capability and improvement with increasing pressure. We also consider the use of LITGS and DFWM simultaneously, which has not been done before, as a possible way to measure precise and accurate species concentration information via DFWM while obtaining precise temperature information via LITGS and while taking advantage of the same experimental setup. The following chapter will discuss the physics of these techniques and relevant work done by our group and others, upon which this work builds.

Chapter 3

Physics and applications of DFWM and LITGS

3.1 Overview

This chapter provides a more detailed description of DFWM. An overview of the widely used Abrams and Lind model of the basic theory is presented followed by an alternative treatment developed by Bratfalean, Lloyd and Ewart (BLE). The present work adapts this model for use in MATLAB to enable ease of application and efficient use of computing power. Relevant applications of DFWM to concentration measurements and thermometry from the literature are then described. The chapter also provides a brief description of the physics of LITGS and relevant applications of the technique upon which this work builds.

3.2 Degenerate Four Wave Mixing (DFWM)

3.2.1 Physics of DFWM

Degenerate four wave mixing, as described briefly in the previous chapter, involves three frequency-matched input beams, which are made to overlap in a suitable nonlinear medium to produce a fourth signal beam of the same frequency such that:

$$\omega_4 = \omega_1 = \omega_2 = \omega_3. \tag{3.1}$$

This process can be represented with a grating picture. While various experimental geometries are possible, in the forward folded BOXCARS phase-matching geometry (geometry that is employed in this research), three fields propagate forward, converging at a small angle to each other. Two of the beams can be considered to form an interference pattern. The spatial modulation in the resulting light field leads to a grating-like modulation of the complex refractive index and is referred to as a coherent population grating. The spacing between grating planes, Λ, is given by:

$$\Lambda = \frac{\lambda_{pump}}{2\sin(\frac{\theta}{2})}. \tag{3.2}$$

Where λ_{pump} is the wavelength of the light and θ is an arbitrary angle of intersection between the wave vectors. A third beam is then scattered off of the grating formed by the first two to generate a signal. The intensity and line shape

of the resultant signal is a function of saturation and absorption of the medium, laser bandwidth, polarisation effects, effects of collisions and atomic motion.

The Abrams & Lind theory of DFWM

The physics of DFWM is illustrated by deriving $X^3(\omega)$ in the case of degenerate fields interacting with a two-level atom - following the widely used Abrams and Lind (A&L) approach [52, 56]. They make a number of simplifying assumptions including a monochromatic laser field interacting with a weakly absorbing medium of two-level atoms and a weak probe. Using a perturbation theory approach they derive an expression for the spectrally integrated intensity of the signal beam with the following proportionalities in two intensity limits:

$$I_{sig}^{int} \propto \frac{\mid \mu_{21}^8 \mid N^2 k^2 T_1^2 T_2^3}{(1 + 4I_{pump}/I_{sat})^{5/2}} I_{pump}^2 I_{probe} \quad I_{pump} \ll I_{sat}(0) \tag{3.3}$$

$$I_{sig}^{int} \propto \mid \mu_{21}^3 \mid N^2 k^2 T_1^{-1/2} T_2^{1/2} I_{pump}^{-1/2} I_{probe} \quad I_{pump} \gg I_{sat}(0) \tag{3.4}$$

Here μ_{21} is the electronic dipole moment involved in the transition from the excited state 2 to the ground state 1. T_1 is the decay time of the population excitation (longitudinal relaxation time) and T_2 is the decay time of the coherence (transverse relaxation time). N is the atomic number density and k is the magnitude of the wave vector at frequency ω. I_{pump} and I_{probe} are the intensities of the pump and probe respectively and $I_{sat}(0)$ is the line centre saturation intensity.

The key point of the above expression for the purposes of detection spectroscopy is that the signal intensity scales with N^2. This is an intrinsic feature of DFWM

and its coherent nature. The polarisation and therefore the signal electric field amplitude add coherently from the atoms in the ensemble and will therefore be proportional to the atomic number density N. The signal intensity is proportional to the square of the electric field and is therefore proportional to the number density squared. The N^2 signal dependence means that the signal can be interpreted in terms of species concentration it is thus potentially useful for diagnostic purposes.

3.2.2 Non-perturbative DFWM model

As mentioned in the previous chapter, while the perturbative A&L model, and associated simplifying assumptions, has proven sufficient to model many useful scenarios, it often falls short in combustion environments. In particular, strong, saturating pump and probe beams are needed in practice to obtain useful signals and limit the effects of collision rate on the signal. In addition, assuming a Doppler-free and monochromatic source are often insufficient to reproduce the signal spectrum obtained in experimental conditions.

Reichardt and Lucht developed a more compete treatment using a direct numerical integration (DNI) approach to solve the four-wave mixing polarisation density matrix equations [57]. In doing so they are able to account for the effects of atomic motion and produce solutions for arbitrary pump and probe energies and for finite pulse duration. They demonstrated the ability to overcome many of the A&L model limitations as well as good agreement with experimental results [57–60]. The primary limitation of the DNI model, however, is that it is computationally expensive.

Bratfalean, Lloyd and Ewart (BLE) developed a non-perturbative, analytical

model for DFWM [53]. This model accounts for saturating probe beams and for Doppler broadening inherent in the forward BOXCAR geometry and can be extended to broadband lasers sources and used for single-shot thermometry in the case of non-saturating beams. It ultimately yields the following, relatively easy-to-compute, expression for the amplitude of the signal.

$$\begin{aligned} A_4 = & \frac{-\alpha_0(i(\delta + T_2\Delta_D))E_sL}{2\epsilon_0\pi N_0} \exp\left[-ln(2)\left(\frac{2\Delta_D}{\omega_D}\right)^2\right] \\ & \times \sum \frac{(2m-1)!I_{pump}^m I_{probe}^{m-1/2}2^m}{m!(m-1)!(R(\Delta_D)^{2m}} \left(-\mathscr{I}_1(b,m) + \frac{2mI_3\mathscr{I}_2(b,m)}{(m+1)R(\Delta_D)}\right) \end{aligned} \tag{3.5}$$

Key terms in this expression have the following meanings: α_0 is a collection of terms including dipole moment for the transition, number density of the molecule and T_2 relaxation time; Δ_D is the Doppler shift between the molecule frame and lab frame for molecules moving with a component of their velocity u_x in the direction of the propagation of the input beams (assumed to be co-linear); ω_D is the Doppler width; δ is the normalisation detuning; L is the interaction region length; I_{probe} and I_{pump} are the normalised probe and pump intensities respectively. $\mathscr{I}_1$ and $\mathscr{I}_2$ are integrals describing the spatial interference pattern determined by the geometry of the pumps and probe, which are constant for a given experimental setup and so can be pre-calculated. R and b are a collection of terms given below.

$$
\begin{aligned}
\mathscr{I}_1(b,m) &= \int_0^\pi \frac{(1+cos(x))^m}{(1+bcos(x))^{2m}}dx \\
\mathscr{I}_2(b,m) &= \int_0^\pi \frac{(1+cos(x))^m}{(1+bcos(x))^{2m+1}}dx \\
R &= 1+(\delta+T_2\Delta_D)^2+2I_{pump}+I_{probe} \\
b &= 2I_{pump}/(1+(\delta+T_2\Delta_D)^2+2I_{pump}+I_{probe})
\end{aligned}
\tag{3.6}
$$

This model has been shown to have good agreement with a full numerical solution and with experimental data with C_2 [61, 62]. Figures 3.1 and 3.2 show that the expression is in good agreement with the A&L model in the limit of a non-saturating probe but disagrees, as expected, with a strong, saturating probe and provides a more accurate line shape and fit to experimental data. [61]

3.2.3 A computational tool using the BLE model

While the analytical expression of equation 3.5 is complicated, it can be translated into a computational environment and calculated quickly with a personal computer, in contrast to the DNI model. This enables it to be used for fitting spectral simulations to experimental data quickly and easily. The expression was originally encoded in Fortran, which ultimately became obsolete. An effort was made in the present work to develop the expression into a new model using MATLAB and so enable other research groups, which currently rely on the more approximate theory developed by Abrams and Lind or the computationally expensive DNI approach, to have access to a fast and accurate tool.

The code was made more efficient and flexible by removing redundant or unnecessary steps that are required in Fortran but can be done more efficiently in

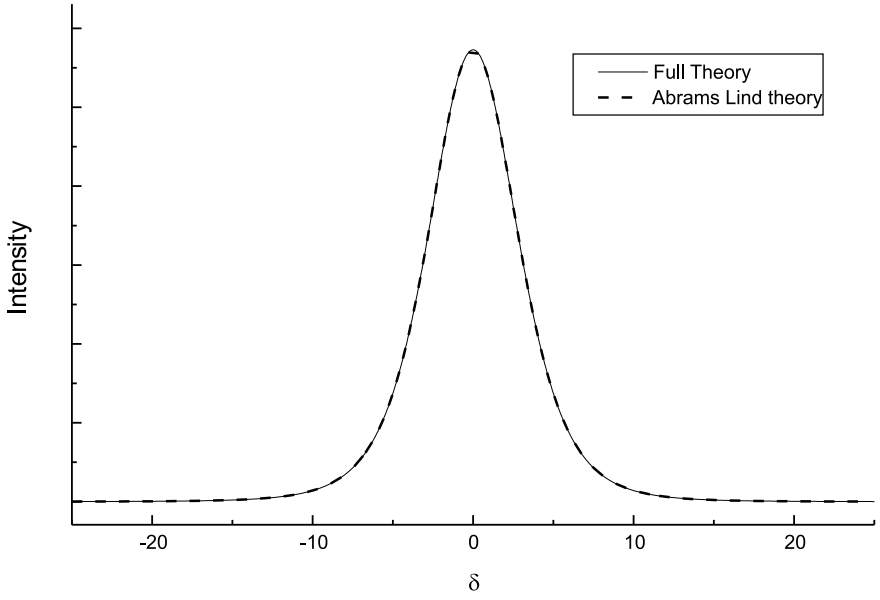


Figure 3.1: Comparison of A&L theory with BLE theory for saturating pump fields but weak probe field, $I_{probe}/I_{sat} = 0.01$

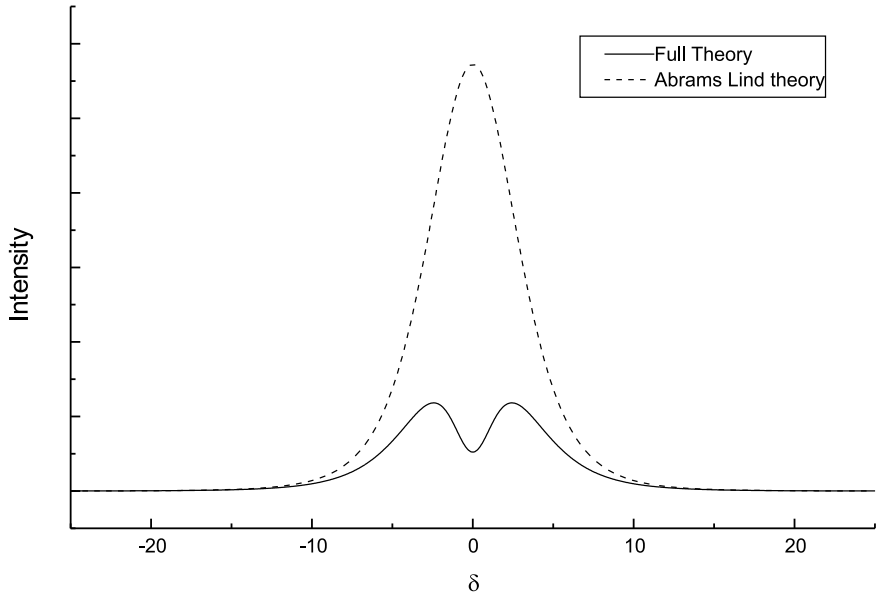


Figure 3.2: Comparison of A&L theory with BLE theory for saturating pump and probe fields $I_{probe}/I_{sat} = 10$ in this case)

MATLAB, including moving calculations outside of loops and taking advantage of MATLAB's greater flexibility to work with vectors. This significantly reduced the code run-time to seconds. The code was modularised into individual functions, making it more adaptable to add additional molecules, fitting functions and to be used by a broader research community.

MATLAB-based simulation of DFWM OH spectrum

The simulated signal is created by first establishing a number of parameters used throughout the calculations including wavelength range, saturation intensity, temperature, transverse relaxation time, and ratio of pump to probe energy. The molecular properties are then read in from a pre-populated file, including the location and ground state energies of the transition lines as given by Dieke and Crosswhite [63] and Höhnl-London factors, which relate to the line strength values, from Goldman and Gillis [64]. Next, the code reads in files with the pre-calculated values of the integrals $\mathscr{I}_1$ and $\mathscr{I}_2$. This was necessary in Fortran in order to reduce calculation time. In MATLAB however these integrals could be calculated within the code rather than pre-calculated and read-in.

The signal amplitude for points near the specified transition lines are calculated according to Equation 3.5, starting at the peak and moving outward to both higher and lower wavelength points in discrete, specified steps, until the contribution of the next step is less than 0.1% of the peak value. The intensity for these points is then calculated from the modulus. The resulting spectrum is convolved with an instrument function to account for the bandwidth of the laser.

When fitting data, the experimental start and end wavelengths of the scan and

resolution of the points are used to specify the simulation points and the power of the laser is used to set I_{pump} and I_{probe}. A least squares fitting is done using standard MATLAB functions.

OH spectra simulation

The code has been developed initially for the OH radical - a common combustion product that has been used extensively in DFWM experiments. OH has strong electronic transitions and its spectral properties are well understood. In this case, a strong electronic band near 300 nm, the $A^2\Sigma - X^2\Pi(0,0)$ band, was used.

A DFWM experimental spectrum was recorded by [65] who used a phase conjugate geometry (thus removing Doppler effects) and a methane-air flame with saturating pump and probe beams. The pump beams were generated by a Nd:YAG-pumped dye laser and KDP second harmonic generation (SHG) crystal (see [65] for experimental details). Figure 3.3 shows that the updated MATLAB code is able to generate an accurate simulated signal when compared with experimental data. The code has also been developed for C_2 (adapted from the work of Lloyd) and could be extended to other molecules.

3.2.4 DFWM in combustion temperature and species measurements

DFWM has been used extensively in combustion for temperature and species concentration measurements. The first application of DFWM to a combustion species was in 1986 by Ewart and O'Leary in OH in a methane flame [50]. They suggested the possibility of using DFWM to obtain flame temperature from measurements of

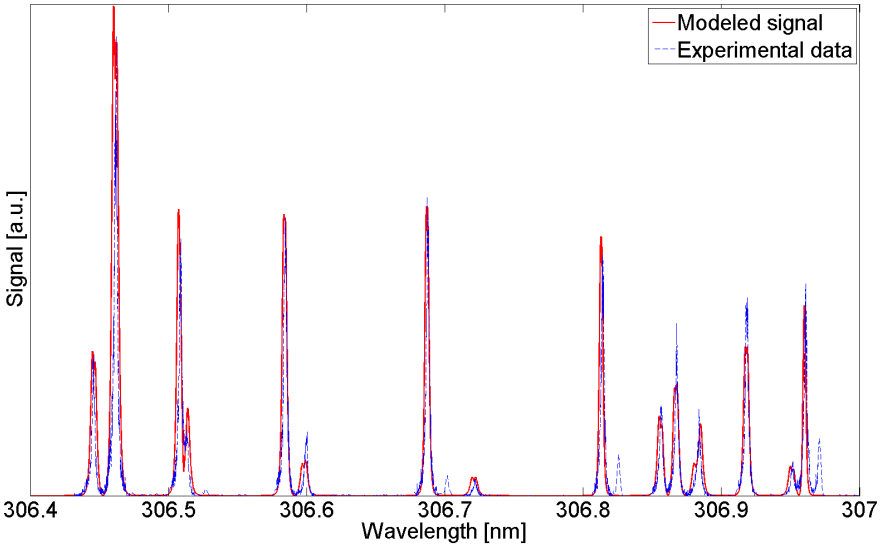


Figure 3.3: Simulation of DFWM *OH* spectrum produced by BLE model with updated MATLAB code, compared with experimental data

the relative intensities of rotational lines (as shown above) as well as measurements of spatial distribution of molecules.

Thermometry of flames using DFWM spectra of OH was demonstrated for time-averaged point measurements [51]. Point measurements have been extended to 1-D and then to 2-D maps by use of a cylindrical lens used to form sheets of light from the pump and probe beams which then form a planar interaction region [66, 67]. Single-shot measurements using broadband laser excitation rather than scanning have also been demonstrated [68]. This allows for real-time, rather than averaged temperature measurements. A dual-wavelength laser providing light centred at two distinct wavelengths within a single pulse has also been demonstrated as an alternative approach for single-shot measurements [47].

DFWM has been used in concentration measurements, the focus of this work. [45, 50, 66, 69]. In particular, DFWM has been used to detect NO in flames [70]

and measurement of relative concentrations of NO in a firing spark-ignition engine have also been demonstrated [71, 72].

3.3 Laser Induced Thermal Grating Spectroscopy (LITGS)

3.3.1 Physics of LITGS

Qualitative description

In DFWM, collisional quenching can lead to an additional process in which a thermal grating is created in the same location as the population grating, as described briefly in the previous chapter. A probe beam can then be scattered off of this thermal grating in an analogous way to DFWM and provide useful information about the bulk properties of the medium - foremost being high precision local temperature measurements. This is known as laser induced thermal grating spectroscopy and has become a useful spectroscopic technique in its own right. A illustrative schematic of the technique is shown in figure 3.4.

As in DFWM, the interference pattern of degenerate pump beams resonantly excites target molecules in an interaction region. Collisional quenching of the excited molecules leads to rapid local deposits of kinetic energy in the bulk gas within the fringe spacing. This in turn leads to the creation of local density perturbations via two distinct mechanisms: First, the deposit of kinetic energy, in the form of heat, in the location of high laser intensity creates local density minima. This forms a thermal grating which decays exponentially due to thermal

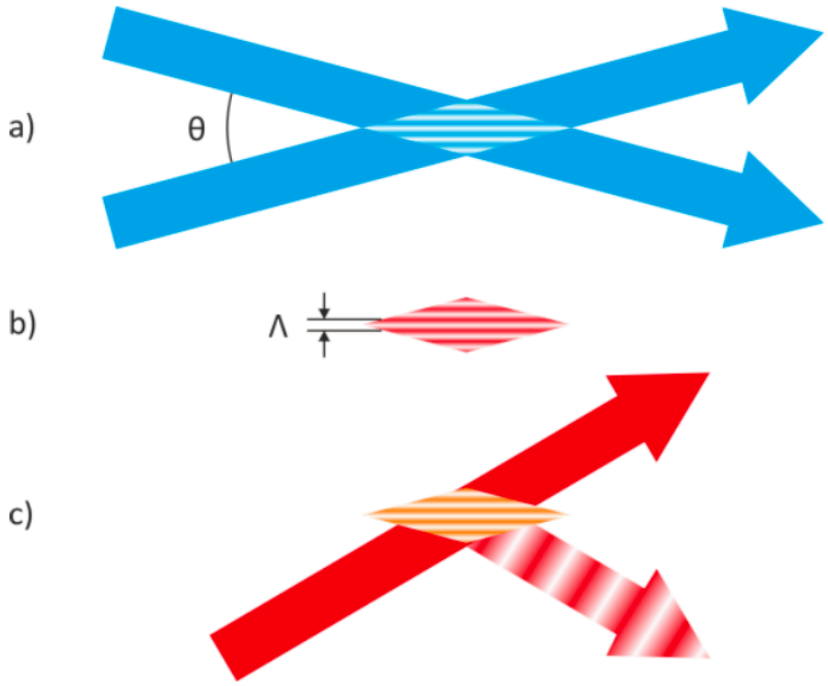


Figure 3.4: Schematic of (a) formation of the fringe pattern from crossing degenerate pump beams, (b) thermalisation of energy leading to local heating and formation of an oscillating density perturbation and (c) monitoring of the oscillating density perturbation (thermal grating) via a probe beam scattered due to the resulting change in index of refraction.

diffusion. Second, the sudden change in pressure launches two counter-propagating plane acoustic waves which travel normal to the temperature grating planes at the local sound speed. This results in a standing wave oscillation referred to as an acoustic grating and decays due to viscous damping. The resulting total density perturbation is a standing wave oscillation superimposed on a stationary thermal grating, as the acoustic wave comes in and out of phase to interfere constructively and destructively with the thermal grating [73]. Figure 3.5 illustrates the evolution of the combined density perturbations in time.

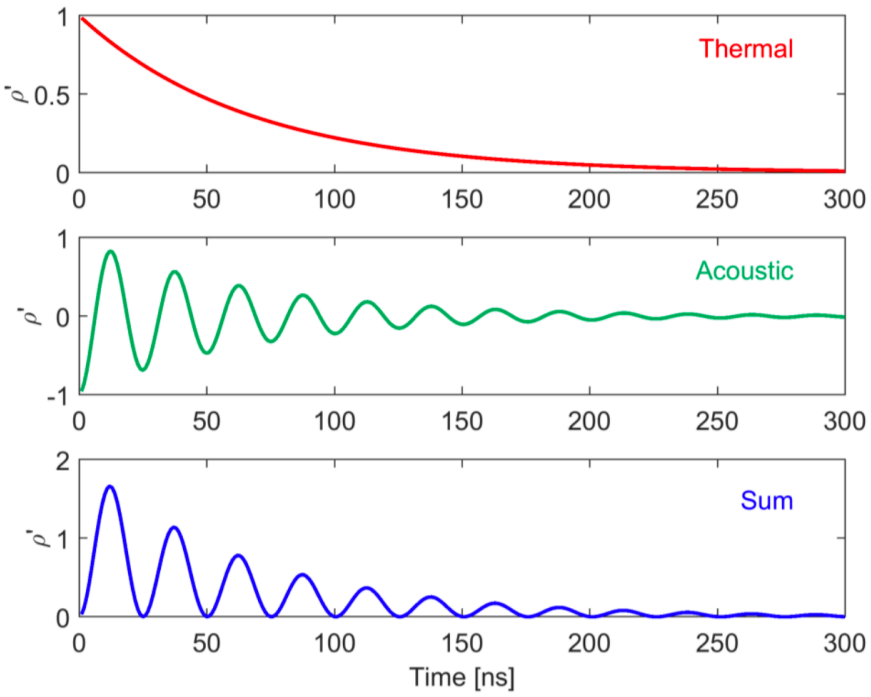


Figure 3.5: Evolution of the LITGS density perturbation over time in the case of an instantaneous excitation pulse

The dynamics of this grating may then be detected by scatting a third "probe" beam and recording its evolution in time and thus the underlying bulk parameters of the medium which define it. The probe wavelength, angle of incidence and grating spacing must satisfy the Bragg equation:*

$$\lambda_{probe} = 2\Lambda sin\phi. \tag{3.7}$$

Where ϕ is the scattering angle and the grating spacing is given by equation 3.2. The signal measures oscillations in grating over time and appears as a rapidly

*Bragg equation form for diffraction order zero

increasing intensity followed by an oscillatory exponential decay. Importantly, temperature can then be derived from the sound speed of the gas in the interaction region. The frequency, f, of acoustic standing wave oscillations is given in terms of the local sound speed, c_s by equation 3.8:

$$f = \frac{c_s}{\Lambda}, \tag{3.8}$$

The value of f can be obtained from the Fourier transform of the LITGS signal. The inverse of equation 3.8 represents the time for the acoustic wave to travel between grating planes and is referred to as the inter-fringe transit time, τ. Assuming that we can treat the medium in the interaction as an ideal gas and that the composition of the gas can be reasonably estimated, the local sound speed is given by:

$$c_s = \sqrt{\frac{\gamma k_B T}{m}}, \tag{3.9}$$

where γ is the ratio of specific heats at constant volume and pressure, m is the mean molecular mass of the gas, k_B is Boltzmann's constant and from this we can derive the temperature, T:

$$T = \frac{m\Lambda^2}{\gamma k_B} f^2. \tag{3.10}$$

The fact that temperature is derived from the frequency, rather than the signal intensity, makes LITGS a highly precise technique. Intensity-based techniques, by contrast, must account for variations in detector noise, laser intensity fluctuations, species concentrations, etc. The measure of frequency is improved with increasing

number of oscillatory peaks. Quenching rate, pressure and gas composition all affect the number of peaks. For a given species, higher pressure leads to slower diffusion speed and thus slower decay of the thermal grating and thus a higher precision measurement [74].

Theory of LITGS

Here a brief summary of the theory of LITGS is presented for convenience and to illustrate some of the underlying physics and important parameters that are discussed in later chapters. For further detail see the source papers or summaries (ie, [22, 73, 75, 76]).

Models of the LITGS process have been developed based on the solution of linearised hydrodynamic equations governing the evolution of the induced gratings and show excellent agreement with experimental observations where the relevant gas dynamic parameters are known or can be estimated with reasonable accuracy. The theory was developed by Paul *et al* [73]. Essentially the same processes were identified as Laser Induced Thermal Acoustics (LITA) by Cummings as a means of measuring gas dynamics or thermodynamic properties of gases [75]. The summary below follows Paul's formulation.

Paul describes a single-rate as well as a two-rate quenching model. While both are a simplification to the actual underlying physical quenching process, the two-rate model (which has a "fast" and "slow" component) was shown to provide a significantly better match to experimental results. The two-rate model is incorporated into signal modelling described later in this thesis. However for simplification, the single-rate model is summarised below.

The theory seeks to describe the effects of heating on the gas dynamics due to the quenching within the intensity maxima of the fringes, in particular the evolution of the density perturbation with time. The problem is treated as one-dimensional by assuming infinite grating planes, which is justified if the acoustic waves don't propagate significantly outside of the interaction region defined by the crossing pump beams, which is typically the case experimentally. We can assume local thermal equilibrium since the mean free path is much shorter than the grating spacing and the mean time between molecular collisions is much smaller than the pulse duration and decay time. The problem is also assumed to be inviscid (i.e., large Reynolds number, Re) As a result of these assumptions, the problem can be characterised by linearised hydrodynamic equations*.

$$\frac{\partial \rho'}{\partial \zeta} + \frac{\partial u'}{\partial \xi} = 0 \tag{3.11}$$

$$\frac{\partial u'}{\partial \zeta} + \frac{1}{\gamma}\frac{\partial P'}{\partial \xi} - \frac{4}{3Re}\frac{\partial^2 u'}{\partial \xi^2} = 0 \tag{3.12}$$

$$\frac{1}{\gamma}\frac{\partial P'}{\partial \zeta} - \frac{\partial \rho'}{\partial \zeta} - \frac{1}{RePr}\left(\frac{\partial^2 P'}{\partial \xi^2} - \frac{\partial^2 \rho'}{\partial \xi^2}\right) = \phi_{ext} = \frac{\gamma - 1}{\gamma}\frac{\epsilon h \nu_a Q \Lambda}{c_0}\frac{N^*(\zeta, \xi)}{P_0} \tag{3.13}$$

Equation 3.11 is the continuity equation and is set to zero as there is no loss or creation of mass. Equation 3.12 is the momentum transport equation and is set zero as there is assumed to be no net force on the molecules. This assumption holds

*Linearising here means expanding parameters (in this case density, velocity and pressure) about an equilibrium point and discarding any terms which are higher order than linear in the perturbation.

if the field strengths are low enough so as not to cause electrostriction. In the case of stronger fields, the force due to electrostriction would need to be included here. Equation 3.13 is the energy transport equation and is the result of the transfer of internal molecular energy to heating. This equation has a spatial dependance due to the spatially varying fringe pattern and a time dependance due to the excited state population decaying over time due to non-radiative processes.

The equations have been made dimensionless using a characteristic length and time. $\zeta = c_0 t/\Lambda$ and $\xi = x/\Lambda$ are normalised time and length parameters, where Λ is again the fringe spacing and c_0 is the isentropic sound speed in the absence of a grating. $\rho'(x,t) = \Delta\rho(x,t)/\rho_0$, where ρ_0 is the unperturbed density value and $\Delta\rho$ is the change in density. P is the pressure and u is the flow speed through the grating planes. The linearised ideal gas law, $P' = \rho' + T'$, and the equation of state for the enthalpy of an ideal compressible medium, $h = c_v T + PV$, are used in the above equations as written, where h is enthalpy, c_v is the specific heat at constant volume, T is temperature and V is volume ϵ is the fraction of the energy stored internally in the molecule that is released as heat, after absorbing a photon of energy $h\nu_a$. γ is the ratio of specific heat capacities, c_p/c_v. N^* is the excited state population number density, and varies as a function of x and t, or in the dimensionless formulation, ξ and ζ. Q is the quenching rate, and ϕ_{ext} is the external driving term which is perturbing the system.

The Reynolds number, Re, which describes the relative magnitudes of the inertia and the viscosity of the flow, is defined as $Re = c_0\Lambda\rho_0/\mu$, where μ is the dynamic viscosity. Low Reynolds numbers, where viscous forces dominate, indicate laminar flow fields. High Reynolds numbers, where the inertia of the flow dominates,

indicate turbulent flow fields. The Prandtl number, Pr, is defined as $Pr = c_p\mu/K$ where K is the thermal conductivity. The Prandtl number relates viscous diffusion and thermal diffusion. A small Prandtl number indicates a flow where the thermal diffusion rate is high, leading to thermal boundary layers which are thick relative to velocity boundary layers.*

Assuming the problem described by equations 3.11 - 3.13 is irrotational and separable into space (ξ) and time (ζ) terms, it reduces to one wave equation which is solvable by Fourier transforms in space and Laplace transforms in time. The solution for the normalised density perturbation is then given by:

$$\rho' \propto \cos(2\pi\xi) Z(\zeta) \tag{3.14}$$

Here $Z(\zeta)$ is the temporal response and is the convolution of the impulse response function, $W(\zeta)$, the temporal profile of the laser pulse, $G(\zeta)$, and the temporal profile of the quenching process, $M(\zeta)$.

$$Z(\zeta) \propto W(\zeta) \star G(\zeta) \star M(\zeta) \tag{3.15}$$

$W(\zeta)$, the instantaneous impulse response function is given by:

$$W(\zeta) \propto a_1 e^{s_1\zeta} - 2a_2 e^{-b_1\zeta} \cos(b_2\zeta + \phi) \tag{3.16}$$

Here $a_1, a_2, b_1, b_2, s1$ and ϕ are constants which depend on γ, Re, Pr and are found as part of the solution to be:

*Over the range of temperatures and pressure in this work, Pr is approximately constant at 0.7. The Prandtl number for air varies by only 2% between $500 - 1000$ K and $1 - 10$ bar [77]

$$s_1\zeta = -\frac{(2\pi)^2}{RePr}\zeta = -\frac{4\pi^2 K}{\Lambda^2 \rho_0 c_p}t \tag{3.17}$$

$$b_1\zeta = -\frac{(2\pi)^2}{RePr}\frac{\left(\gamma - 1 + \frac{4Pr}{3}\right)}{2}\zeta = -\frac{4\pi^2 K}{\Lambda^2 \rho_0 c_p}\frac{\left(\gamma - 1 + \frac{4c_p\mu}{3K}\right)}{2}t \tag{3.18}$$

$$b_2\zeta = 2\pi\zeta = 2\pi\frac{c_s}{\Lambda}t \tag{3.19}$$

The first term of $W(\zeta)$ represents the stationary thermal component of the grating described earlier, which decays with $-s_1 c_s/\Lambda$. The second term represents a standing wave formed by the two counter-propagating acoustic waves and decays with $b_1 c_s/\Lambda$. Experimentally, s_1 and b_1 are found to be of similar order and result in the acoustic and thermal components of the density perturbation decaying at similar rates [78]. From the above, a complete solution for a thermal grating can then be obtained.

3.3.2 LITGS signal analysis

As shown in the above discussion, the LITGS signal contains information about the local environment. If gas dynamic parameters can be reasonably assumed to be known then temperature, pressure or species concentration (absorber number density or quencher number density) can be derived. Or, conversely, if these are known then the gas dynamic parameters can be found, i.e., see reference [79].

Temperatures analysis

The temperature can be derived from the oscillation frequency, f, via derivation of speed of sound, c_s, given by Equations 3.8 - 3.10. Assuming the grating spacing, Λ, is known, the sound speed can be calculated from the gas composition according to Equation 3.9.

Two major sources of uncertainty in temperature measurements are the grating spacing, and gas composition. Determining grating spacing, Λ from geometric alignment is prone to significant error. This can be easily overcome, however, by performing calibration measurements at a known temperature and gas composition. Λ can then be derived and applied to future measurements so long as the pump beam alignment is not changed. The uncertainty due to grating spacing is therefore reduced to the knowledge of the calibrated temperature measurement.

At a given temperature, the local sound speed is set by the mean molecular mass, m, and ratio of specific heats, γ. In a test cell this can be known with high accuracy. In a combustion environment this is known with less certainty. In a laminar flame at stoichiometric conditions, the situation described in chapter 7, kinetic models can be used to calculate the concentrations of combustion products in the burnt gas. In more complex combustion environments, uncertainty increases. However it has been shown elsewhere that highly accurate and precise temperature measurements can still be made in such environments and the error can be limited [78, 80, 81].

Oscillation frequency recovery can be another significant source of uncertainty for weak signals or signals with rapid decay which offer few oscillations (i.e., signals

produced in high temperature and low pressure environments). Any uncertainty or systematic error in deriving frequency will translate into errors in derived temperature, amplified by the quadratic relationship between frequency and temperature. Fitting of LITGS signals can help to quantify and reduce error and will be further discussed in chapter 6.*

If the interaction region, defined by the volume created by the overlap of the pump and probe beams, cuts across a non-uniform temperature gradient, contributions to the signal from hot and cold regions will sum resulting in a signal of more than one oscillation frequency. This can potentially be overcome by modelling and fitting multiple signals using tomographic modelling to extract multiple temperatures [83] or by ensuring a small interaction region to avoid multiple temperature regions.

Pressure analysis

The decay rate of the signal depends on the rate of diffusion of molecules following the initial density perturbation. Assuming an ideal gas, the diffusion coefficient is proportional to the mean free path and mean velocity of the molecules. The diffusion rate is therefore directly proportional to pressure and proportional to the 3/2 power of temperature. As a result, for known temperatures, the time constant of the underlying exponential decay of a signal can be used to derive pressure. A simulated signal can be fit to the data following Paul et al and solving for Re and the inter-fringe transit time, τ. From these parameters pressure can be derived so long as there can be reasonable knowledge of the gas kinetic parameters -

*See also [82] for a detailed discussion.

density, viscosity, heat capacity and thermal conductivity. See [84, 85] for additional background and this will be further explored in Chapters 6 and 7.

Target species number density

Number density of resonant absorber species in the interaction region will determine the amount of energy absorbed and heat deposition and therefore of the density perturbation and signal strength [86]. Integration of the total signal intensity will therefore provide a measure of target molecule number density. However there are many contributions to signal intensity which would need to be controlled in order to do so. These include, among other factors, laser pump and probe intensity, pump laser spectral width, temperature, pressure and absorption cross section of the target species. Therefore extracting concentration information is subject to signifiant difficulty and sources of error but in principle is possible using LITGS. As there are few alternatives for instantaneous concentration measurements in ambient pressure and combustion environments and because concentration can potentially be obtained simultaneously with temperature and pressure information with no additional experimental cost, this is explored briefly in the present work.

3.3.3 LITGS in spectroscopy

LITGS signals were first identified in four-wave mixing experiments with NO and OH in flames [73, 74, 87]. The application of these effects for measurements of gas dynamic parameters and temperature was first recognised and demonstrated by Cummings and co-workers as Laser Induced Thermal Acoustics (LITA) [88]. Cummings was able to derive the temperature of laboratory air from time-averaged

LITA signals arising from absorption by trace amounts of NO_2. The potential for measurement of other gas-dynamic and thermodynamic measurements was also soon recognised [55, 89], including pressure [90], concentration [91–93] and velocity [94].

The first demonstration of temperature and pressure measurements using LITGS in a flame were carried out by Latzel et al [95]. High precision temperature measurements of the order of 2% were recorded from cell-based measurements. Brown et al showed that thermometry of sooting flames was possible using LITGS [96].

More recently, the high precision available from LITGS thermometry of under 0.1% has led to increased interest in the technique [85]. LITGS has been used for fuel-air mixing measurements [97], multi-point temperatures in gas flows [98], shock-tube studies [99] and time-resolved transient temperature and pressure variations using a high-repetition rate laser [100]. In-cylinder temperatures of a firing spark ignition engine were measured with high, single-shot, precision by Williams et al. using the fourth harmonic of a Nd:YAG laser at 266 nm to produce the grating in fuel vapour [80]. High precision measurements of temperature were recently demonstrated for in-cylinder measurements in the same engine showing resolution of evaporative cooling effects for direct injection strategies [82]. Hell et al have used the fundamental output of a Nd:YAG laser at 1064 nm as the pump beams for LITA with a pulsed probe beam, to measure temperatures in methane/air and H_2/air flames as well as a hot supersonic H_2 /air free jet [99]. Finally, Sahlberg et al. have demonstrated LITGS thermometry of flames using mid-IR pumps around 3000nm and a cw probe laser at 457 nm to generate LITGS signals from combustion

generated H_2O [101].

3.4 Summary

This chapter has provided a review of the theory of DFWM and LITGS techniques and how they can be used to derive useful information from a remote interaction region. A non-perturbative model for DFWM, developed previously by BLE, was updated and expanded into a useable form for the OH molecule in this work. A brief summary of the application of these techniques to temperature, pressure and concentration measurements in combustion environments was presented. The work that follows builds upon this work to further investigate the interaction between these two techniques and apply them for a new use, that of investigating temperature, pressure and NO concentration in a combustion environment for eventual application within a turbulent combustion environment like that of a gas turbine engine.

Chapter 4

Experimental setup & considerations

This chapter describes the experimental setup that was developed for and used throughout this work. An overview is given of the primary optical layout, as well as variations for different experimental configurations. The choice of laser system is discussed in some detail as this proved critical to success and some important limitations were identified by using two different laser systems - an optical parametric oscillator (OPO) and a dye laser. The physical properties of nitric oxide, the target species of this work, are described as relates to its interaction in DFWM and LITGS processes, as is the pressurised combustion chambers in which NO molecules were probed. Finally, the alignment and operation procedures are described.

4.1 Optical layout

The key components of the experimental layout of this work involve the following:

- production of an excitation wavelength resonant with our target species, NO
- DFWM and LITGS pump and probe beam arrangement
- the test region (i.e. an optical cell and pressurised burner in this case)
- signal detection and recording

The majority of experiments were conducted with a single setup that enabled both DFWM and LITGS to be performed simultaneously. The forward BOXCARS geometry was employed throughout this work. Figure 4.1 illustrates the full setup.

4.1.1 Excitation beam

A resonance wavelength of Nitric Oxide, 226 nm, was used for the excitation or 'pump' beams throughout this work. This wavelength was produced via a sum-frequency mixing process. The second harmonic of a flashlamp-pumped solid state Nd:YAG (Continuum, Precision II Powerlite), produced 180 mJ of 532 nm light per 7 ns pulse at a repetition rate of 10 Hz and was used to pump a dye laser to produce up to approximately 18 mJ of 623 nm light, a conversion efficiency of about 10%. This wavelength was chosen as dyes exist that produce this which are relatively easy to work with and long-lived. This wavelength was mixed with the third harmonic of the Nd:YAG (355 nm) to produce our desired output, which

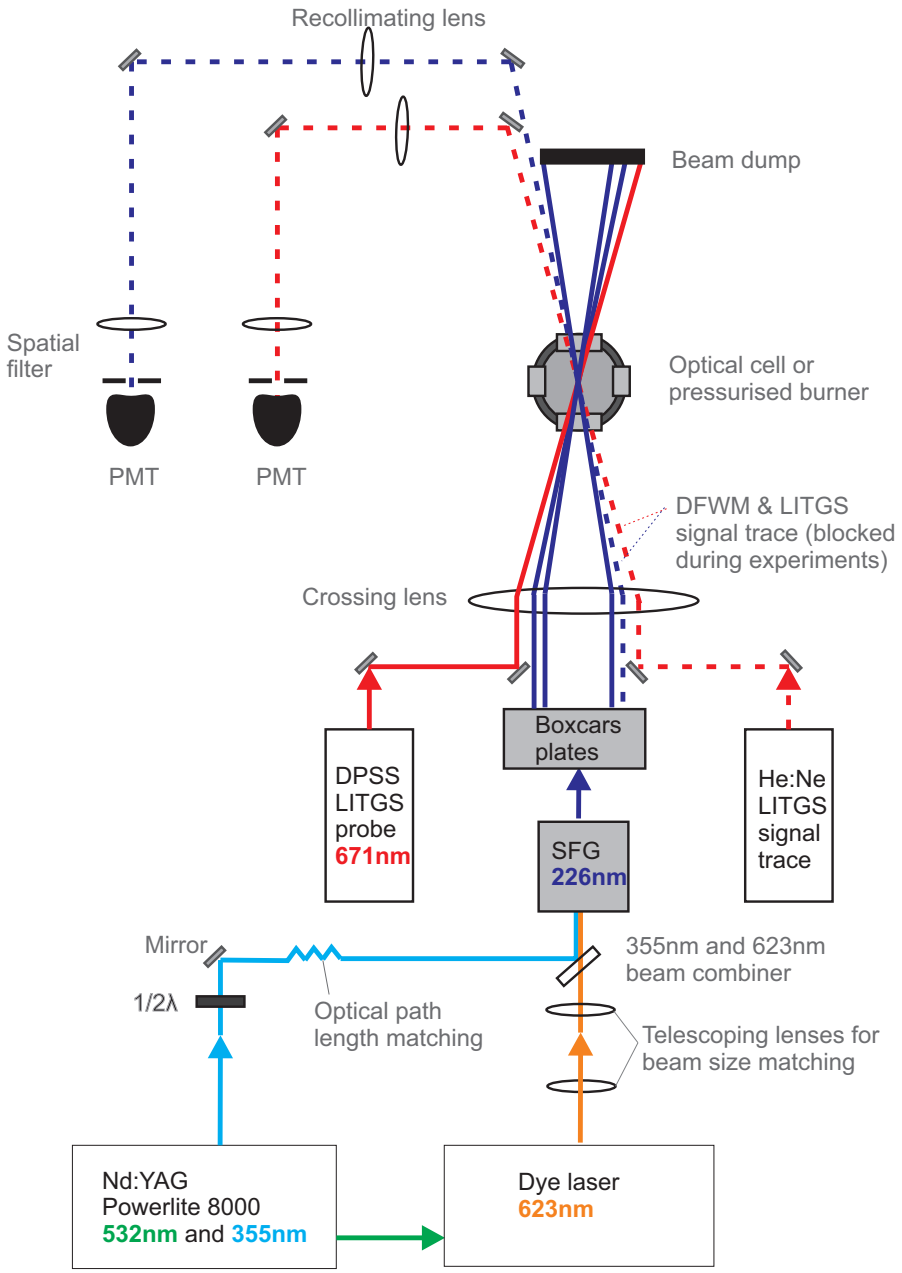


Figure 4.1: Schematic of the experimental setup developed and used in this work including lasers, optics, test cells and detectors for simultaneous DFWM and LITGS signal production. This setup, with minor variations, was built for and used throughout the entirety of this work.

is also relatively easy to produce, has a narrow line-width and abundant energy, delivering about 20 mJ per pulse in this case.

The 355 nm and 623 nm beams were path-length matched to ensure temporal overlap and size-matched using lenses to ensure efficient use of all of the available energy and to better match wave fronts to optimise interaction efficiency. A half wave plate was used to change the polarisation of the 355 nm beam from horizontal to vertical to match the polarisation of the 623 nm beam. The beams were then made to mix in a sum-frequency generation (SFG) β-Barium Borate (BBO) crystal* which produced a maximum of 3 mJ of 226 nm light. Further losses from optics between the mixing crystal and the interaction region meant there was a maximum of 1.5 mJ available at the interaction region. In practice between 80 μJ to 1 mJ was used in experiments.

The wavelength of the second harmonic of the NdYAG was measured with a pulsed wavemeter (Burleigh WA-4500) and found to be 532.2214 nm ($\pm$0.00005). From this, the third harmonic was calculated to be 354.8133 nm. The output of the dye laser was tuned until a strong resonance with NO found. This wavelength was then measured to be 623.43 nm ($\pm$0.005)†. Combined these produce a wavelength of 226.12 nm from the SFG crystal. This is the wavelength that was used in the majority of experiments that follow. Figure 4.2 shows this wavelength relative to the simulated absorption spectra of NO given by LIFSim [111]. As can be seen, this wavelength falls within a range of dense, strong lines for the NO molecule.

*Bluebean Optical Tech, BBO Type 159.1/0 deg, P-coating

†The Burleigh wavemeter has two Etalons which enable it to provide two different resolution ranges. For the diode-seeded Nd:YAG we were able to use the more sensitive "Etalon B" and thus obtain a greater precision in wavelength. For the Dye laser, which has a broader spectral width, the wavemeter was unable to resolve the wavelength to the same precision.

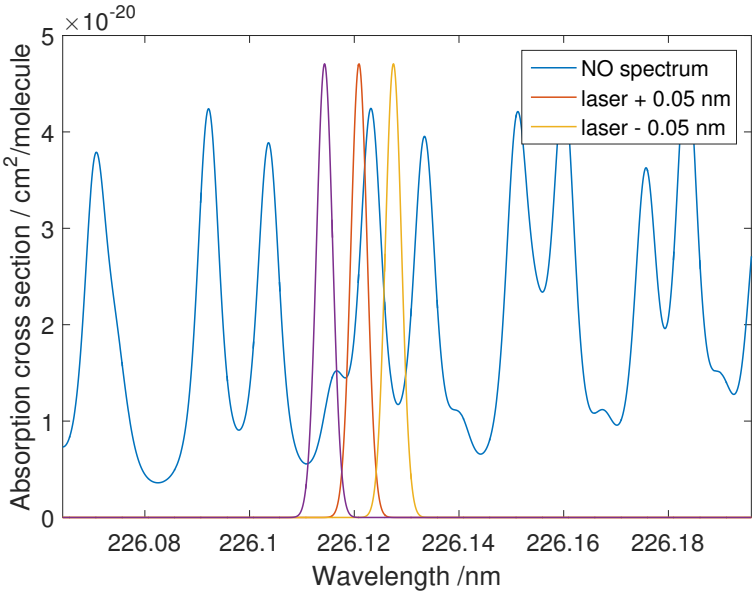


Figure 4.2: Estimated laser pulse and NO transition lines at atmospheric conditions.

Scanning was possible with this system over this range of lines from approximately 225.5 nm to 227 nm.

Single longitudinal mode (SLM) operation of the Nd:YAG laser was enabled by seeding the Nd:YAG oscillator with a cw SLM input (Continuum SI-200) and, when combined with the modeless dye laser, produced a relatively narrow line width 226 nm beam. Using an Fabry-Perot etalon, and measuring the distance between fringe spacings, the line width was found to be 0.3 cm^{-1} or 0.0015 nm at 226 nm. This narrow line width proved critical to the success of flame-based experiments. When the seeder was turned off, the signal strength would drop by nearly an order of magnitude. When using an OPO, with a line width of $2 - 5$ cm^{-1}, a signal in a flame proved illusive, as will be described further below.

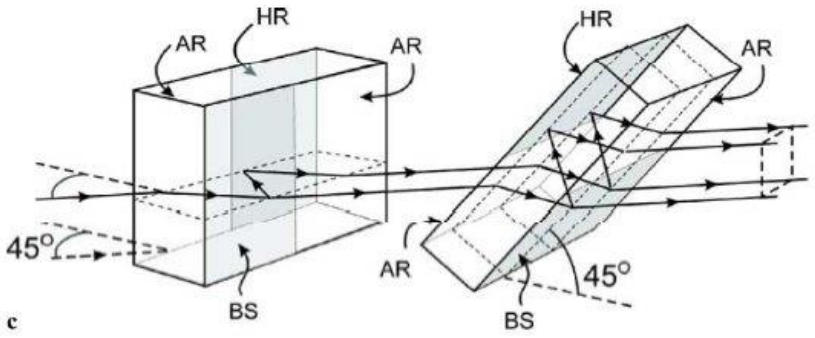


Figure 4.3: Illustration of the beam splitter plate assembly used to generate four degenerate, parallel beams from a single input beam at 226 nm. Two beam splitters, each with an anti-reflection (AR) and high-reflection (HR) coatings and oriented in orthogonal planes, produce four parallel output beams. The single beam is incident to the first plate at an angle of 45 degrees and the AR and HR surfaces serve to produce two parallel beams in the horizontal plane. These two beams are then split by the second plate in the vertical plane.

4.1.2 DFWM and LITGS pump and probe beam arrangement

Custom designed BOXCARS plates were used to divide a single beam to produce degenerate pump and probe beams for DFWM with a wavelength of 226 nm [71, 72, 102]. These consist of two thick quartz blocks, placed at incident angles of 45 degrees to the incoming beam, which partially reflect the beam and thus generate four parallel, equally spaced beams. See figure 4.3.

In DFWM, as described in the previous chapter, three of the beams interact in the mixing process. The fourth beam is used for alignment purposes as it traces out the direction of the expected signal beam but is then blocked during the experiment

and data acquisition. A 750 mm focal length lens was used to cross and focus the beams into the interaction region. The beam spacing and focal length were chosen such that the beams cross at an appropriate angle to satisfy the phase matching condition.

To conduct LITGS experiments, two of the beams described above served as pump beams while the other two are blocked. Two additional lasers are introduced for LITGS. A 1 Watt, CW diode-pumped solid state (DPSS) laser operating at 671 nm served as a probe of the thermal grating (CNI model MLL-FN-671-1W). A Helium-Neon laser was aligned to trace out the expected LITGS signal path and was then blocked during experiments and data acquisition. These beams were again made to cross via the 750 mm focal length lens. The probe beam spacing was determined such that the probe is incident to the grating at the Bragg angle and so optimise efficiency of the scattering and thus signal strength.

4.1.3 Interaction region

Where the pump beams cross, they define an "interaction region". The size of the interaction region sets the spatial resolution of the technique. The length of the interaction region is established by the crossing angle (θ) and the diameter (d) of the beams. The crossing angle also determines the interference fringe spacing (Λ) and thus, for LITGS the interfringe transit time (τ) and signal frequency (f), as described in the previous chapter.

For LITGS there are important tradeoffs to be considered between desired spatial resolution, signal quality and experimental requirements or limitations. The interaction length (l) can be made smaller (and thus spatial resolution along the

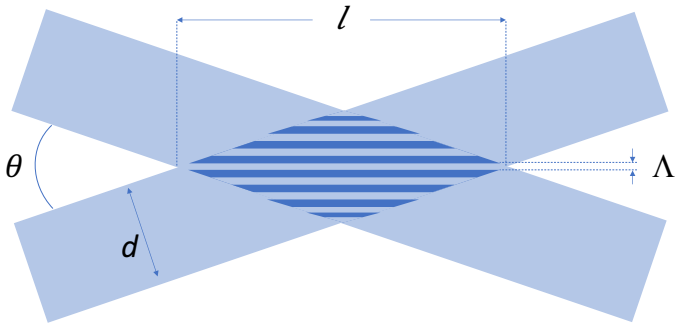


Figure 4.4: Illustration of the grating formed in the interaction region, of length l as two beams of diameter d cross at an angle θ. A grating is formed with grating spacing Λ.

optical axis improved) by reducing beam diameter and increasing crossing angle. This is desirable in the case of turbulent combustion diagnostics where unsteady flow features can be at the millimetre scale.

Conversely, however, the interference fringe spacing and number of fringes can be increased by increasing beam size and decreasing angle. Sufficient fringe spacing and number of fringes are important in order to optimise signal contrast and number of oscillations, which in turn improves confidence in determining signal frequency and thus temperature. In practice this means the signal oscillation period should be sufficiently shorter than the signal damping time. The damping time, $t_{damping}$, is given by:

$$t_{damping} = \frac{\Lambda^2}{2\pi}\frac{1}{\chi} \tag{4.1}$$

where Λ is the grating spacing and χ is the thermal diffusivity and is given by:

$$\chi = \frac{k}{\rho c_p} \tag{4.2}$$

k is the thermal conductivity, ρ is the gas density and c_p is the specific heat at constant pressure.

At higher temperatures χ increases and therefore the damping time decreases. The oscillation frequency also increases with temperature as was described in a previous chapter, but does so more slowly. Therefore a geometry (and associated fringe spacing) which may produce a strong signal at room temperature may be insufficient at higher temperatures. For a more detailed discussion of beam configuration considerations see, for example, [86].

Practical constraints also play a role. Optical access constraints may limit what crossing angles are possible, for example. Energy density requirements may necessitate smaller beams at the interaction point depending on how much total energy is available in the beams or, conversely, may necessitate larger beams and lower energy density to avoid damaging optics.*

All of these factors influenced the geometry chosen in the present work. Several different geometric configurations were used and these are described below.

Combined DFWM and LITGS geometry

For the combined DFWM and LITGS work, described in chapter 5, the geometry of beams was chosen such that a grating spacing of 12μm would be achieved.

*the LITGS signal amplitude is proportional to the square of the pump energy for non-saturating beams

Energy density considerations led to the use of beams that were focused, rather than collimated, into the interaction region so that small diameter beams would be produced and maximise the energy density within the interaction region.* The beam spacing was 13.5 mm, which was set by the design of the BOXCARS plates described above. A 750 mm fused silica lens was used to focus and cross the beams into the interaction region. The beam sizes were approximately matched and measured to be 590 μm for the 226 nm beams and 615 μm for the 671 nm probe beam ($\pm$30 μm).

LITGS only geometry

For the LITGS-only work described in chapters 6 and 7, in the optical cell and pressurised burner respectively, the BOXCARS plates were removed. Instead a beam-splitter was used to generate the two 226 nm pump beams. This was done to reduce energy losses from the two additional beams that the BOXCARS plates generate and from the additional quartz surfaces and allowed greater flexibility in geometry of setup. Again, a focused geometry was used and a 750 mm crossing lens. The grating was 14 μm for much of the work conducted in the chamber described in Chapter 6. However for the pressurised burner, a larger grating spacing was deemed necessary to improve the signal. Here a 21 μm grating spacing was used, achieved by changing the pump beam spacing and thus crossing angle.

*A collimated geometry where the pump beam is defocused and then collimated through the crossing lens, would have advantages but it was found that, with the total beam energy available, smaller diameter beams were required than was practically achievable with collimation, especially when operating within a flame.

Defocused geometry for pressure measurements

Chapter 6 describes estimates of pressure derived from LITGS signals. This was done by measuring the signal decay rate which is a function of pressure. A competing source of signal decay, however, can be the sound waves moving outside of the interaction region (see, for example, [79]). The transit time, $t_{transit}$, is defined by the width of the interaction region divided by the local sound speed and by geometric analysis is given by:

$$t_{transit} = \frac{2r}{\sqrt{2}c_s} \tag{4.3}$$

Where r is the radius of the beam volume and c_s is the sound speed. At room temperature and with a nitrogen buffer gas in the chamber, c_s is 350 m/s and the signal decay is observed to be 1μs. The beam diameter was thus chosen such that the transit time is greater than the observed decay and thus we can have confidence that the signal decay is a result of the pressure effects only. To achieve this, the pump beams were defocused by a lens upstream of the crossing lens. The crossing lens then served to collimate as well as cross the beams.* This not only results in larger beams but also has the advantage of plane wave fronts at the interaction region and removes the need to re-collimate the beams after the interaction region, which can be a large contributor to noise in the signal beam path. The pump beams were measured to be 1.48 mm ($\pm$0.2 mm) and probe beam, again size-matched with the pumps for energy efficiency, was measured to be 1.60 mm.

*In the case of convex lenses, this requires the spacing between the defocusing lens and crossing lens to be the sum of their focal lengths

4.1.4 Signal detection and recording

The pump and probe beams were blocked downstream of the interaction region. The signal beams were allowed to propagate for several meters to take advantage of the coherence of the signal and help to reduce noise. Further noise reduction measures included a series of apertures, spatial filters and shielding around the detectors. In the case of LITGS, a high-transmission, narrow bandpass filter for 671 nm was used to block scattered pump light which would otherwise be detected as a peak just prior to the first LITGS peak. Ultimately signal to noise ratios of 10:1 or greater were achieved in all cases.

For signal detection, two Hammamatsu photomultiplier tubes (PMT) were used [103]. These were chosen for their fast response time, high sensitivity and large active area, sufficient to capture the entire beam. Care was taken to remain within the linear response regime of the detector both by controlling gain and via optical attenuation of the signal, such that the PMT accurately records variations in intensity of the signal and is not saturated.*

In order to determine an appropriate gain setting and optical attenuation to avoid saturation, the linearity of response to signal strength was investigated. Figure 4.5 shows a non-linear response for signals above about 850 mV where the shape of the signal is affected by PMT saturation. In practice care was taken to keep signal strength well below this level. A consistent gain value was used within each data set as the PMT gain changes the time response of the detector.

*I.e. the relationship between intensity of the incident light and magnitude of the signal remains linear. The PMT can become saturated when the current demand on the final dynode stages is too great and the effective gain is reduced for the strongest sections of an incident signal.

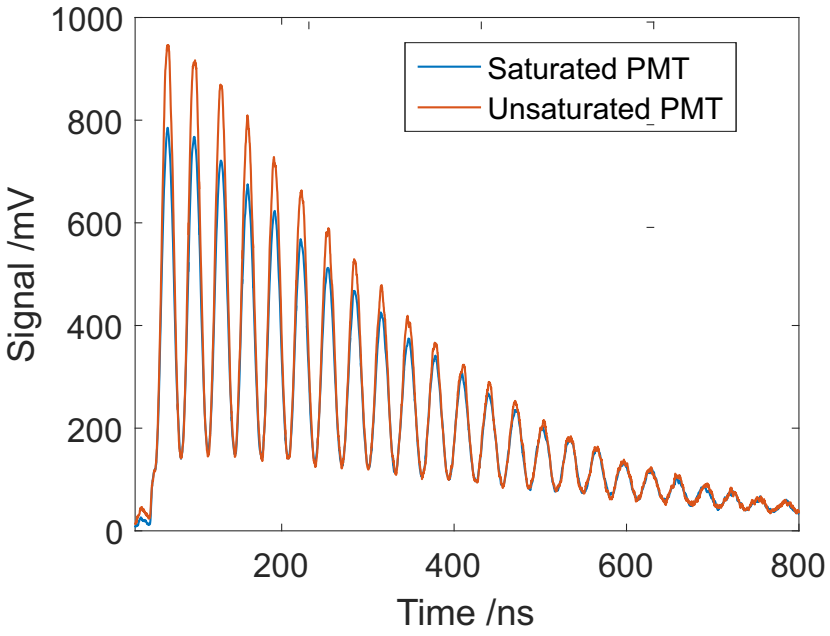


Figure 4.5: Signal with a saturated and unsaturated PMT. Saturation changes signal shape.

4.2 Laser system selection

4.2.1 Optical Parametric Oscillator (OPO)

Prior to using the dye laser mentioned above, all experiment were first conduced with a Continuum Horizon Optical Parametric Oscillator (OPO). In the OPO the gain medium is a non-linear crystal which is pumped by the third harmonic of the Powerlite Nd:YAG laser described above. The non-linear $\chi^{(2)}$ interaction of the 355 nm pump beam with a non-linear medium results in the generation of two beams such that the phase matching and energy conservation conditions as described for

the $\chi^{(3)}$ process earlier, are met* [21]. The advantages of the Horizon OPO are that, once setup and aligned, it is easy to operate across its broad tunability range (192 nm-2750 nm). This made it convenient to investigate various flame products and experimental setups, including DFWM in OH in a flame at 308 nm and H_2O in a vapour flow at 1400 nm and 1900 nm, in addition to DFWM and LITGS in NO.

It was intended that the present work described in this thesis would utilize the OPO as the pump laser, and indeed the combined DFWM and LITGS work of chapter 5 and much of the chamber based work of chapter 6 was first conducted with the OPO. However, achieving a signal in a flame targeting resonances of NO, OH or H_2O did not prove possible. We ascribe this to the poor beam quality and broad spectral width of $2-5$ cm^{-1} of the OPO. Therefore the OPO was replaced with a dye laser which, while more complex, had the advantage of being narrow band and with good beam quality and resulted in an order of magnitude increase in spectral power for the same beam size and energy as compared with the OPO.

4.2.2 Dye laser

The dye laser system used in the experiments of this work is a modeless laser designed by Ewart [104]. While the primary motivation for moving to a dye laser system was to achieve a beam with a narrower band while retaining sufficient energy, this dye laser also produces a beam which does not feature a discrete longitudinal mode structure. The absence of longitudinal mode structure is achieved by virtue of the absence of a resonant cavity. Instead, a travelling wave pulse of amplified

*the beams are referred to as the "signal" (higher frequency beam) and "idler" (lower frequency beam)

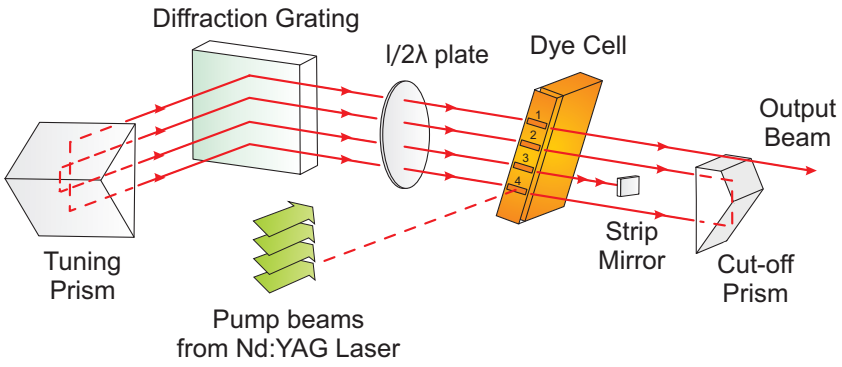


Figure 4.6: Optical layout of the narrowband modeless dye laser.

spontaneous emission (ASE) is passed through spectrally narrowing elements (ie, a diffraction grating and tuning prism) and amplifying regions. As a result this laser system provides a narrow bandwidth of 0.3 cm^{-1} (10 GHz)* without mode structure. It also provides a low divergence, tunability and good efficiency.

A conceptual diagram of the modeless dye laser is shown in figure 4.6. The second harmonic of an Nd:YAG laser (described previously) is used to produce a pump beam which is introduced into the system. A cylindrical lens and four-faceted prism divide the pump beam into four horizontal strips which pump the dye in a cell and produce spontaneous emission emanating from each strip. A mirror is used to retroflect emission from strip 3, which is returned to the dye cell to become further amplified and "seed" the laser. This amplified light passes to a high-dispersion diffraction grating† which results in high dispersion of the beam's frequency components. Components with desired frequencies are made to travel normal to a tuning prism and are reflected to be further amplified while other components fail to travel along the beam path. The tuning prism displaces the

*This can be significantly narrowed by diode laser seeding and has been in other cases (see for example [62, 105, 106] but was not necessary for the work presented here.

†2400 lines/mm

beam with selected frequencies vertically and then back to strip 2 in the dye cell. The light is reflected back to the diffraction grating and tuning prism. This happens two more times through strips 4 and 1, amplifying the selected frequency each time, before the beam is finally passed out of the system. Further amplification is achieved by a preamplifier and amplifier, which are longitudinally pumped by the 532 nm light from the Nd:YAG laser to increase the pulse energy but which also improves the beam quality.

The diffraction efficiency of the grating is optimised when the beam is P-polarized. Given the orientation of the diffraction grating, this would mean horizontally polarised light from the beam. However, the second harmonic of the Nd:YAG is vertically polarised and maximum amplification occurs in the dye if the dye laser light is also vertically polarised. A half wave plate is used, therefore, to change the polarisation of the beam to horizontal just prior to the diffraction grating and then back to vertical before the dye cell.

The angle of the diffraction grating allows for adjustment of the spectral width. Rotating the tuning-prism by way of a stepper motor allows for selection of frequency. Tuning is possible over the spectral range available from the dye fluorescence. For further detail on the modeless dye laser see [46, 50, 62, 105–110].

4.2.3 Dye selection

A combination of dye plus solvent were chosen such that the maximum amplification from the laser would occur at a wavelength that, once mixed with the 355 nm light from the Nd:YAG, would fall within a range of strong absorption lines for the NO molecule (approximately $225.5 - 227$ nm in this case [111]). Therefore, the range

of suitable dye laser wavelengths falls within $619 - 630$ nm.

A number of dye-solvent combinations were tested before a suitable combination was found. Table 4.1 below shows the expected and achieved peak wavelengths with a number of dye solvent combinations. From the literature, DCM* dissolved in methanol seemed an appropriate choice or, alternatively, Rhodamine 640 dissolved in either ethanol or methanol [112, 113]. Our experience, however, was that DCM in methanol or ethanol produced a peak near 635 nm, outside of the range of interest for this work. By adjusting the grating and tuning prism a minimum wavelength of 625 nm was achieved, however, the energy available was insufficiently low. Rhodamine 640 in methanol produced a peak near 609 nm with a range of 602 nm-620 nm but again with very low energy available at 620 nm and therefore also outside of the range of interest for this work. Rhodamine 640 in ethanol produced a peak at 612 nm and a range of 600-625 nm. 10 mJ was produced at 612 nm which dropped to 2 mJ at 620 nm. By increasing concentration the peak was shifted to 616 nm but this still produced insufficient energy at the desired wavelengths.

The desired wavelength was ultimately achieved with DCM in propanol† which produced a peak wavelength near 622 nm. The combined DFWM and LITGS experiments of Chapter 5 and pressure measurements of Chapter 6 were conducted with this dye-solvent combination. Later, in an attempt to produce greater energy, it was found that Rhodamine 640 dissolved in propylene carbonate also produced a peak near 620 nm and with slightly greater energy efficiency. This combination was used for all other LITGS measurements in the optical cell in Chapter 6 and

*4-dicyanomethylene-2-methyl-6-p-dimethyl-amino-styryl-4H-pyran

†The DCM powder was first dissolved in a few millilitres of propylene carbonate due to its better solubility

Table 4.1: Dyes and their expected peak excitation wavelengths versus peak wavelength discovered in the present work.

Dye	**Solvent**	**Expected peak λ**	**Achieved peak λ**
DCM	Methanol	621.5 nm	635 nm
DCM	Ethanol	614 nm	635 nm
DCM	Proponal	607 nm	622 nm
Rhodamine 640	Methanol	620 nm	609 nm
Rhodamine 640	Ethanol	620 nm	612 nm
Rhodamine 640	Porpylene Carbonate	n/a	615 nm

the flame experiments of Chapter 7.

4.3 Target species: nitric oxide

Nitric Oxide (NO) served as the target species for all experiments described in this thesis. As mentioned in previous sections, NO is an important minor species in combustion because of its negative environmental impacts. It also serves as the trace species in the flame, removing the need for seeding - which would be impractical at the high flame temperatures of this work.

The primary pathway of NO formation in a gas turbine engine (the 'thermal' pathway) is due to the reaction of nitrogen with oxygen in the high-temperature zones of the combustor [114, 115].

$N_2 + O \leftrightarrow NO + N$,

$N + O_2 \leftrightarrow NO + O$,

$N + OH \leftrightarrow NO + H$,

These convert N_2 to NO at a rate largely controlled by the first reaction which is endothermic and requires a very large activation energy. As a result this reaction only proceeds at a very high temperature. Concentrations of NO within the

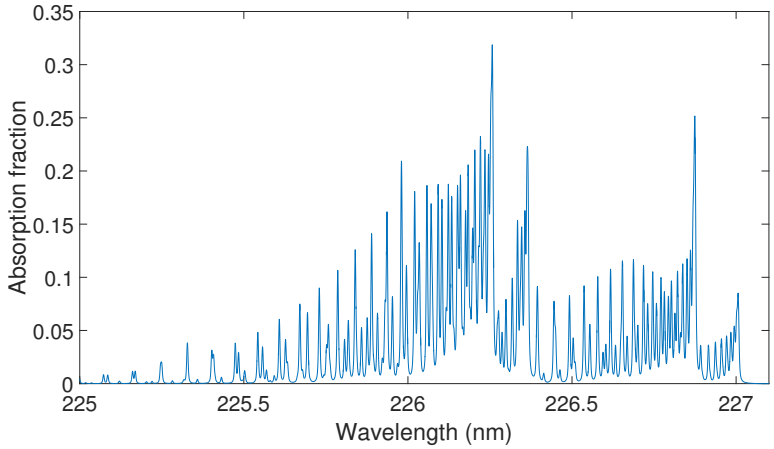


Figure 4.7: NO absorption spectrum at 296 K and 1 bar total pressure simulated with LIFSim [111].

combustion environments explored in this research are expected to be on order of one hundred parts-per-million (ppm). However, as mentioned in chapter 2, NO formation rate is non-linear with temperature and increases rapidly at high temperature.

The techniques employed in this work are greatly enhanced when the pump laser wavelength is resonant with transitions of the target species, in this case NO. Laser light at a wavelength of 226 nm was selected because it corresponds with the $\gamma(0,0)$ band of NO, the first electronically excited state, without excitation of vibrational states. Figure 4.7 show a simulation of the absorption spectrum between $224.5 - 227.5$ nm.

4.4 Experimental combustion environment

Flame measurements were conduced in a pre-mixed methane flame in a water-cooled pressurised chamber (Figure 4.8). A low-pressure chamber was adapted

for high-pressure operation and tested up to 20 bar. In practice measurements were taken between $1 - 5$ bar. The chamber was fitted with smaller radius, thicker quartz windows and high pressure seals. An exhaust needle valve and pressure transducer enabled pressure control.

A pressurised burner offered several advantages for this work. Higher pressures enable stronger, longer-lasting LITGS signals. This setup allowed pressure to be varied and thus enabled the study of the effects of pressure on temperature measurements. The setup also facilitated experiments to use LITGS signals to extract pressure measurements directly. Finally, working at higher pressures enabled us to begin to work in conditions more similar to a gas turbine combustor which operates under high pressure.*

The flame within the chamber was a stoichiometric $CH_4/O_2/N_2$ flame in a custom made 40 mm by 0.5 mm slot burner. The burner's longitudinal axis was aligned with the direction of the pump and probe beams and was designed to ensure the full interaction region fell within a relatively uniform flame zone. The flow was controlled with three mass flow controllers† which enabled independent control of the relative concentration of each gas. Stoichiometric conditions were used for all measurements, however, the ratio of O_2 as a percent of total mole fraction was varied from 20% to 40%. This was done in order to vary the flame temperature and thus the NO concentration and therefore explore LITGS measurements over a range of temperatures and NO concentrations.

*combustor pressures have increased over time from 5 to 50 bar and above [116]
†MKS 1179A, Aalboarg GFC 67, Hastings instruments

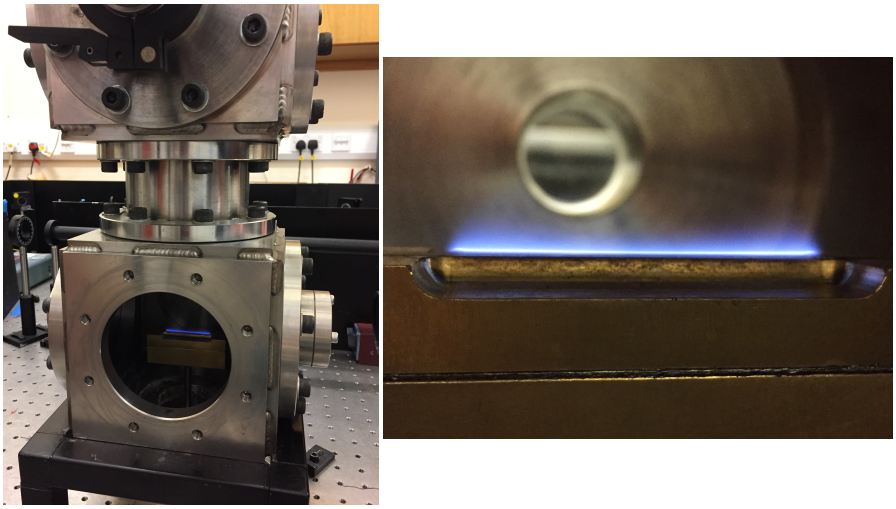


Figure 4.8: Picture of the pressurised chamber and slot burner.

4.5 Alignment and operation

Alignment is critical for achieving strong, stable signals and good measurements for both LITGS and DFWM [117]. Matching beam sizes and spatial overlap, is particularly important. Beam size matching was described above. For DFWM, spatial overlap is achieved quite easily with the BOXCARS plates and crossing lens. The beam spacing is set by the BOXCARS design and the crossing angle is determined by the focal length of the crossing lens. In DFWM in the forward geometry the phase matching condition is satisfied as all beams cross at the same angle. Since the beams are equally spaced by the BOXCARS plates, this condition will be automatically satisfied by a crossing lens of any focal length.

For LITGS two masks are used to align parallel pump, probe and signal trace beams with the correct spacing, calculated such that the desired crossing angles will be achieved when they pass through the crossing lens.* The crossing lens will

*I.e. the desired grating spacing and spatial resolution in the case of the pump beams, the

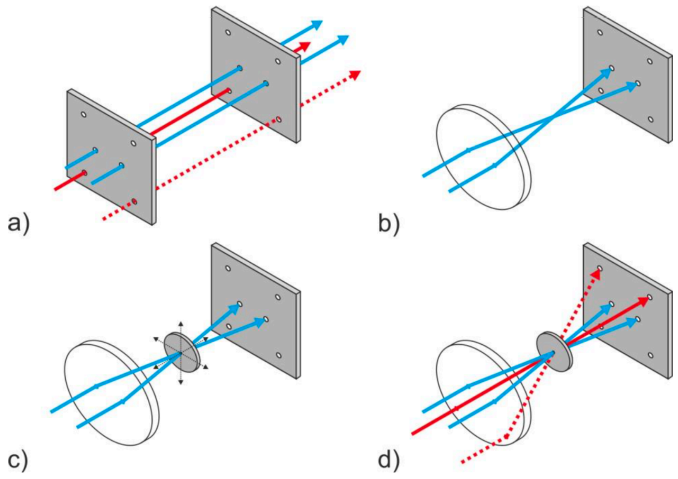


Figure 4.9: Example of alignment procedures for LITGS to ensure beams have a good spatial overlap at the desired angle of intersection. (a) Pump, probe and trance beams are aligned parallel using two masks. (b) The crossing lens is introduced and aligned such that the pump beams are incident with the same point on the second mask. (c) A small pin hole is placed at the crossing point of the two pump beams. (d) The probe and trace are adjusted such that they travel through the pin-hole and are incident with the same points on the second mask.

have a different focal length for the 226 nm beams and the 671 nm probe and signal trace beams due to dispersion, and thus different crossing point. The mask, therefore, serves only as a rough approximation of alignment and this variation must be corrected for.

This correction and other fine tuning is achieved by use of a small pinhole (on order of beam diameter) on a X-Y-Z translation stage placed at the crossing point of the pump beams. This location is determined quite carefully by translating through the crossing point and observing both beams propagating through the

Bragg angle in the case of the probe and the expected signal propagation vector in the case of the signal trace.

pinhole together. The probe and trace beams are then adjusted to both pass through this same point while also arriving at the correct reference marks on the mask. The signal trace is then used to align the expected signal path onto the detector.

A relatively high NO concentration in a optical cell at high pressure is used when first aligning the system to provide a strong signal. Further fine tuning adjustments are then made to the beam steering mirrors to further optimise the signal before moving to realistic experimental conditions in the optical cell or pressurised flame.

4.6 Summary

In this chapter the experimental design and validation were described. The choice of laser system in particular proved critical to success, with the narrow line width of the dye laser enabling LITGS signals to be achieved in a flame which were not possible with the broader line width of the OPO. Considerations of PMT linearity, choice of dye and alignment sensitivity also proved important to the success of the work. While the core setup remained consistent throughout, there were several variations made for specific experimental goals. This setup served as the basis for the results of Chapters 5-7 and will be frequently referred to in those chapters.

Chapter 5

Combined DFWM and LITGS in nitric oxide

5.1 Introduction

Here, for the first time, we consider the use of DFWM and LITGS techniques simultaneously to conduct complementary or calibrating measurements. The transition from a DFWM- to LITGS-dominated effect in the time domain is first demonstrated. We illustrate the competition effects of the two processes when applied simultaneously and show how one effect can be distinguished from the other. DFWM and continuous-wave (CW) LITGS are used simultaneously and we demonstrate an effect of the DFWM probe on the LITGS signal strength. The simultaneous operation of both techniques is demonstrated in NO and potential applications are discussed.

5.2 Background

The most relevant prior work to the current study is that conducted by Danehy *et al* at Sandia National Laboratory [73]. They conducted an extensive study of the extent to which signals from thermal gratings (LITGS signals) contributed to measured signal intensities in DFWM experiments in NO and OH. Thermal gratings were observed to dominate the signal generation in high-density (i.e. cold, high pressure) environments whereas the signal from population gratings, the molecular coherence, dominated in low-density (i.e. hot, low-pressure) environments. At intermediate conditions the LITGS and DFWM signal amplitudes could be comparable.

The relative contributions of the two processes were studied by variation of the collisional quenching rate responsible for energy transfer to the thermal grating using different mixtures of the buffer gases N_2 and CO_2 which have quenching rates for NO differing by several orders of magnitude. They noted also that the temporal behaviour of the two processes was different. The coherent DFWM process decayed rapidly by collisional dephasing leading to a signal that followed closely the time duration of the pump and probe pulses whereas the LITGS signal from the thermal grating decayed on a much longer timescale determined by molecular diffusion and viscous damping. These studies were conducted using a pulsed probe laser and the time evolution of the LITGS signals was mapped by stepping the delay of the probe pulse relative to the excitation pump pulses. They noted that the LITGS signal could be completely distinguished from the DFWM signal simply by delaying the probe pulse until after the pump pulses had terminated at which time

the molecular coherence had decayed to zero.

In the present work the focus is on how these two techniques may be used simultaneously. In the future this could lead to applications, for example, of temperature measurements from LITGS signals and simultaneous species concentration measurements from DFWM signals. First, we illustrate the transition from population-dominated (DFWM) signals to thermal grating-dominated signals by observing the time behaviour of the four-wave mixing signal produced by a degenerate probe. Secondly we show directly the competition between the two processes when the thermal grating is monitored by a non-resonant cw probe incident at the Bragg angle. The use of a continuous wave probe, rather than pulsed, allows us to more readily obtain a frequency from the LITGS signal for use in determining temperatures.

5.3 DFWM and LITGS contributions to signal

Figure 5.1 shows normalised, time-resolved DFWM signals generated in NO at a range of pressures from 20 mbar to 4 bar, using N_2 as a buffer gas to increase the total pressure, and using 226 nm light as described in chapter 4. At relatively low pressures, below 200 mbar, the signal is contemporaneous with the pump pulses and has the same shape, duration and peak timing, characterised by an approximately symmetric Gaussian shape. As pressure increases, the associated increase in molecular collision rate serves to more quickly depopulate the upper state of the excited NO molecules. This results in fewer molecules in the coherent superposition state available to participate in the parametric DFWM process while

at the same time creating a stronger thermal grating in the bulk gas. This can be observed in the higher pressure signals in the figure in which the peak shifts later in time by several nanoseconds and the shape broadens and becomes asymmetric, consistent with the thermal grating contribution which results in a relatively slow rise and fast decay. The collisional quenching process and formation of the thermal grating in the LITGS process is slower to develop than the coherent interaction of the DFWM process.

More and more of the DFWM probe beam photons scatter off the grating in the LITGS process as pressure increases rather than participating in the DFWM process. The data shows that above about 500 mbar N_2 pressure the signal is dominated by the thermal grating contribution. Increasing the quenching rate beyond this level results in no significant additional effect on the resulting signal.

When signal strength is measured against pressure (Figure 5.2) the total signal strength can be seen to decrease with increased pressure and then to level off. In this case, the fully DFWM-dominated signal at low pressure produces a larger signal than the fully LITGS-dominated signal at high pressure. At intermediate pressures, as the signal from the LITGS effect becomes of comparable strength the total combined signal strength drops in relative intensity. For the case of non-saturating pump beams, the DFWM signal is proportional to the square of the population relaxation time (T_1^2) and to the coherence de-phasing time to the fourth power (T_2^4). Both T_1 and T_2 are inversely proportional to pressure and thus this leads to an overall pressure dependence of P^{-6} [74]. By contrast, the LITGS signal strength increases with pressure.

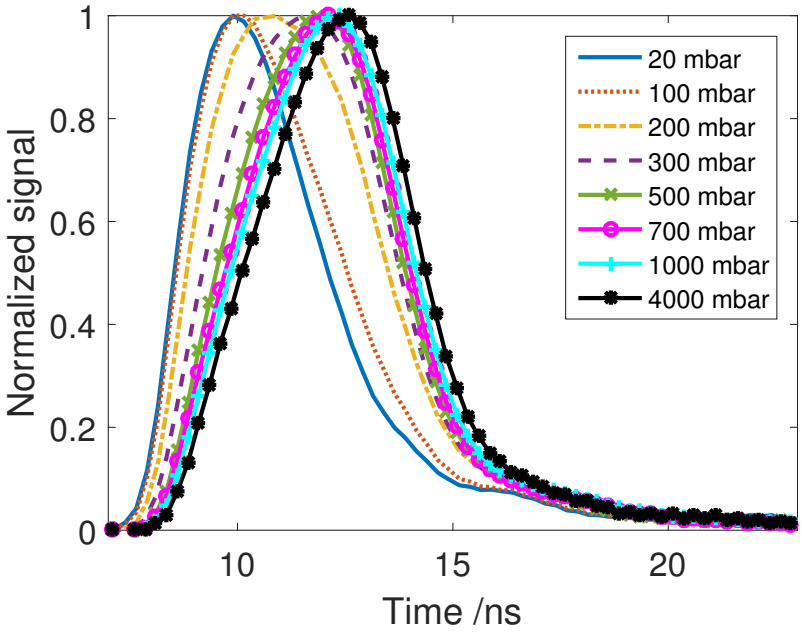


Figure 5.1: Time-resolved DFWM signals in nitric oxide (NO), from 20 mbar to 4 bar total pressure, normalised to peak intensity at different pressures (average of 100 shots). The signal shape broadens and peak location shifts in time as the signal changes from DFWM-dominated to LITGS-dominated.

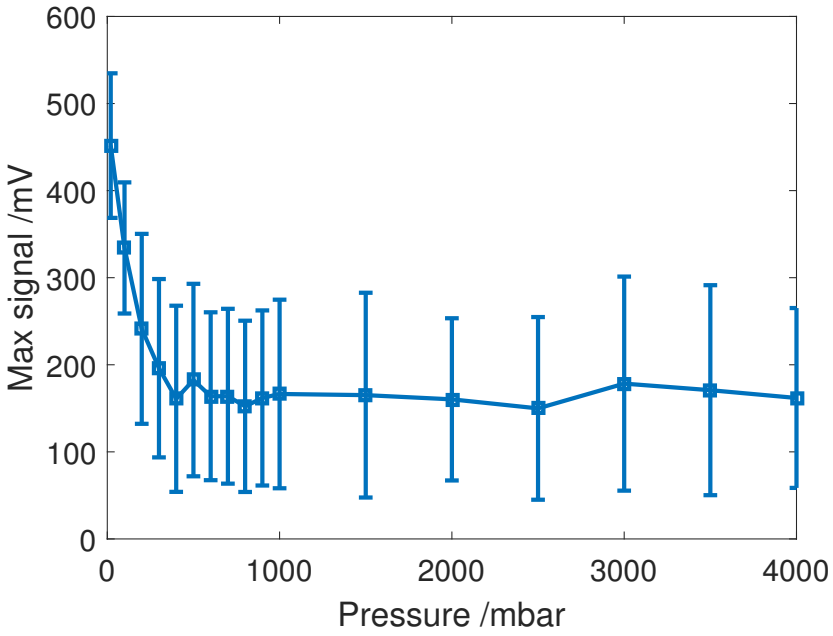


Figure 5.2: Signal strength drops with the transition from from DFWM to LITGS regime, then stabilises.

5.3.1 Saturation of DFWM process

The pressure effects on DFWM signals can be somewhat offset if the upper state populations of the target molecules are saturated by the pump beams. In this way, a pure DFWM signal can be retained at higher pressure, as the saturation can make up for the de-phasing of the collisions. This can be useful in enabling the simultaneous use of DFWM and LITGS at higher pressures.

The signals in Figure 5.1 are unsaturated. Figure 5.3 shows a DFWM signal at a given pressure and NO concentration but with increased total pump and probe energy. As energy increases, the signal broadens in time as the DFWM process becomes saturated.

Polynomial fits to plots of pump energy versus maximum signal are shown in

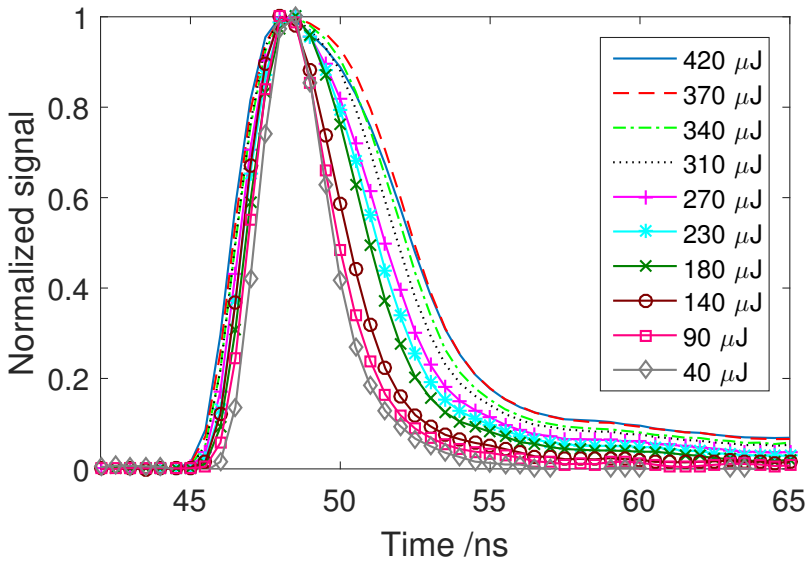


Figure 5.3: Time-averaged DFWM signals at fixed pressure and concentration but with increasing pump and probe energy from $40 - 420\mu$J.

Figure 5.4. These show that below approximately 150 μJ, where the signal is nearly quadratic with laser intensity, is a less saturated regime for pump energies whereas above this energy the process becomes partially saturated and the signal can be seen to become linearly proportional to the pump energy.

Saturation intensity estimate

The saturation intensity is a measure of the optical power per unit area required for achieving significant saturation of an absorber and is given by:

$$I_{sat} = \frac{\hbar\omega}{\sigma\tau} \tag{5.1}$$

ω is the frequency, σ is the absorption cross section and τ is the collision time. The saturation intensity here is roughly estimated to be on order of $6.8 \times 10^{11} W/m^2$

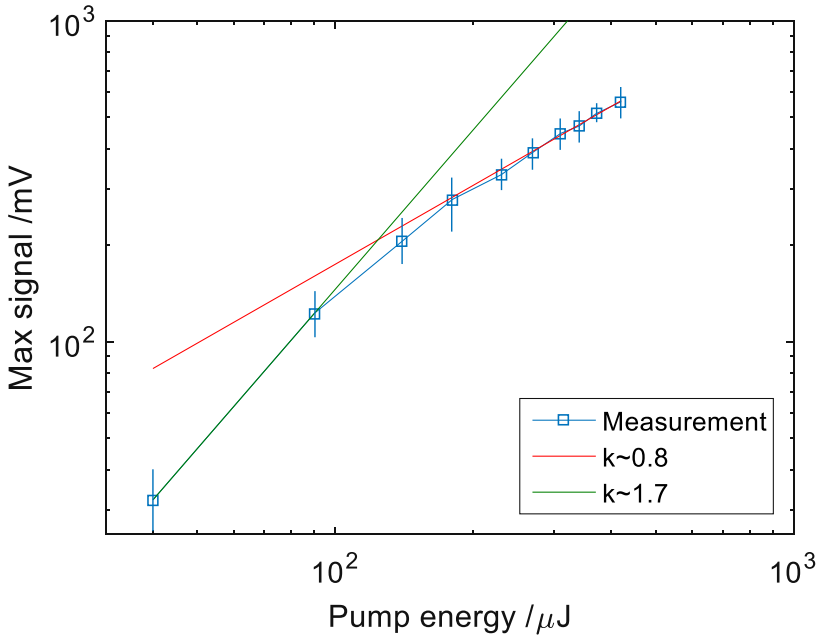


Figure 5.4: Polynomial fits to plots of pump energy vs maximum signal indicate saturated and unsaturated regimes.

at atmospheric conditions. Multiplying I_{sat} by the area of the beam and pulse duration gives an approximate saturation energy of 650 μJ. Several simplifying assumptions were made in this estimate which together mean this is likely to represent an over estimate of the actual saturation intensity.* From Figure 5.3 it can be seen that the transition begins to become partially saturated above 140 μJ and so in practice pump energies were kept below this level for unsaturated experiments.

*Simplifying assumptions include the following: A square wave pulse, perfect alignment of the laser wavelength and transition peak and a sufficiently narrow laser line width such that all energy is deposited within the spectral width of the transition. The laser line width is measured to be $0.2 - 0.3\ cm^{-1}$ which appears to be on order of the width of the NO transition at these conditions, according to LifSim [111]. This estimate also assumes that the life-time is dominated by quenching collisions and thus τ can be equated with the collision rate, which is likely to be the case for pressures explored in this work [118].

DFWM signal with increasing pressure and saturating beams

Figure 5.5 shows DFWM signals with increasing total pressure, similar to figure 5.1 but with pump intensities which are sufficient to at least partially saturate the excitation of the molecular coherence at lower pressure.

In the normalised signals of Figure 5.5 it is seen that at lower pressures saturation leads to a broadening of the signal pulse in time and the effects of collisions are partially compensated by the high pumping rate. Consequently higher pressures are required to cause the thermal grating to dominate the coherent population contribution. A significant contribution from DFWM is apparent at pressures of $500 - 700$ mbar in the saturated case relative to the unsaturated case in Figure 5.1.

As pressure increases more energy is required to continue to saturate as described above. With higher pump energy, therefore, this shift in transition could be further delayed as pressure increases. Limitations of optics damage thresholds prevented this from being pursued in this case, however this could be overcome with a change in setup to use larger diameter beams prior to the crossing lens or optics with higher damage thresholds.

5.3.2 Combined DFWM & LITGS and qualitative simulations

For intermediate pressures where there are approximately equal contributions to signal from both the DFWM effect (population-dominated) and LITGS effect (thermal grating-dominated), signals are produced which exhibit attributes of each. Signals were generated in a cell with 20 mbar of NO and N_2 pressures in the range

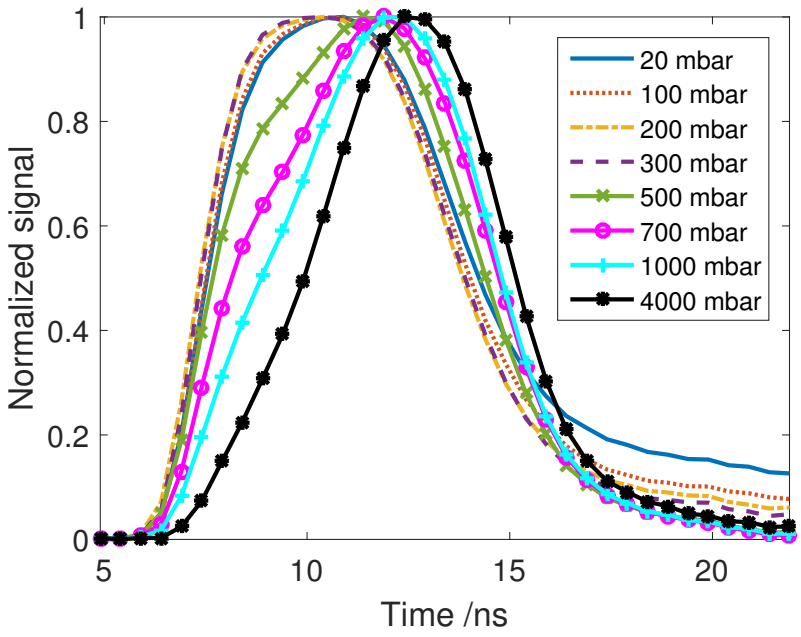


Figure 5.5: Time profile of DFWM signals in NO recorded with a pulsed probe simultaneous with the pump pulses and with partially saturated signals for varying total pressure of N_2.

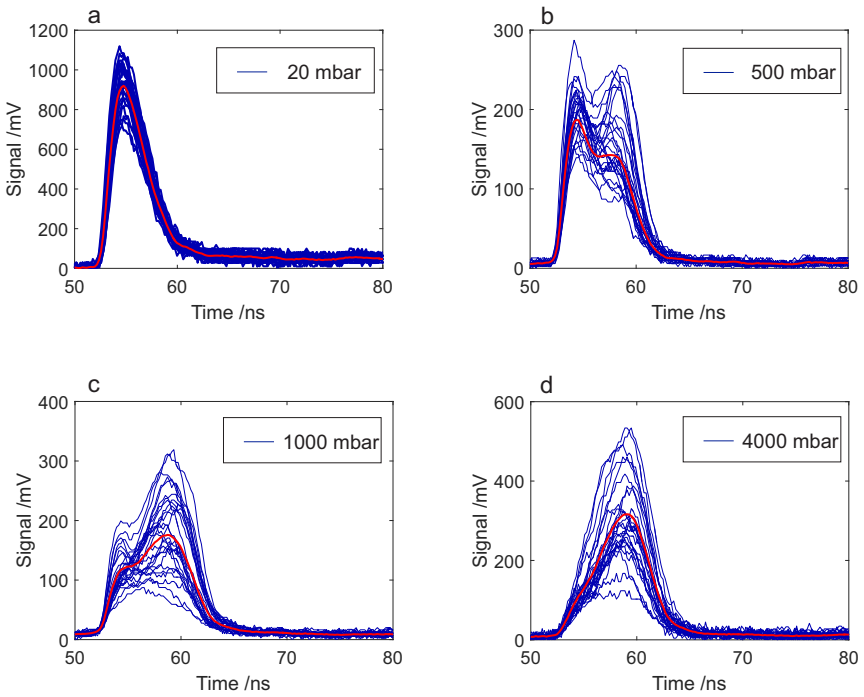


Figure 5.6: 50 single DFWM shots in blue with average overlaid in red recorded at four different total pressures using non-saturating laser intensity.

of $0 - 3$ bar. Figure 5.6 shows the evolution of the signal across this intermediate range of pressures for 50 individual shots and overlaid with the average signal. The temporal behaviour of the signal generated by the pulsed degenerate probe shows the effect of both grating contributions. In the range of pressures between 200 mbar and 700 mbar we observe a shoulder or double-peaked signal exhibiting the combined behaviour.

Figure 5.7 shows the average signals only plotted for a select range of pressures where the pure DFWM and LITGS effects are clearly visible in the very low and very high pressure cases and the shoulder or double peak behaviour is present in the intermediate pressures.

Combined DFWM and LITGS signals have been modelled heuristically by

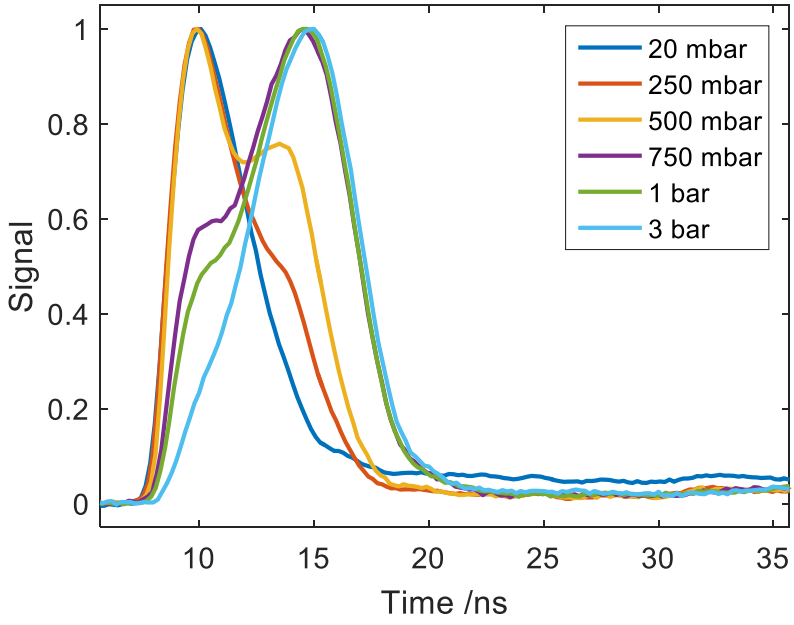


Figure 5.7: Average DFWM signals at different total pressures in the optical cell, demonstrating the change in shape as the signal transitions from DFWM-dominated to LITGS-dominated.

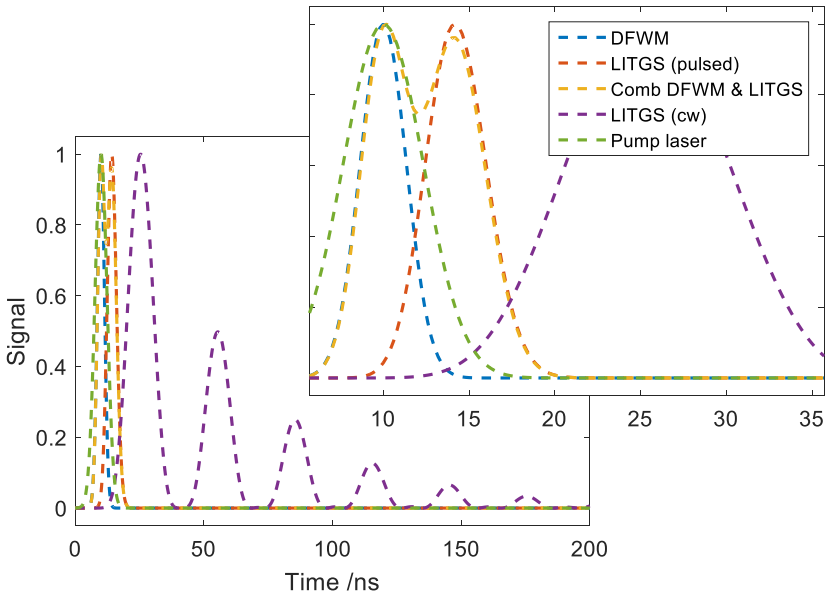


Figure 5.8: Simulation of a DFWM signal using the approach of Abrams and Lind and of a LITGS signal using the approach of Paul et al.

combining contributions from DFWM and LITGS in the time domain, to compare against our experimental results. The DFWM signal was modeled using the approach of Abrams and Lind [52] and the LITGS signal was simulated using the model of Paul *et al* [73]. Combining these models enables a fitting to the intermediate pressures which exhibit comparable DFWM and LITGS contributions to the signal (figure 5.8).

Figure 5.9 shows this model fit to experimental data. The relative signal strengths were adjusted to obtain the best fit as shown by the red dotted line relative to the experimental profiles indicated by the blue solid line. The onset of the LITGS contribution is clearly evident in the growth of the second peak at around 15 ns delay relative to the origin.

The ratio of DFWM contribution to LITGS contribution was simply chosen for

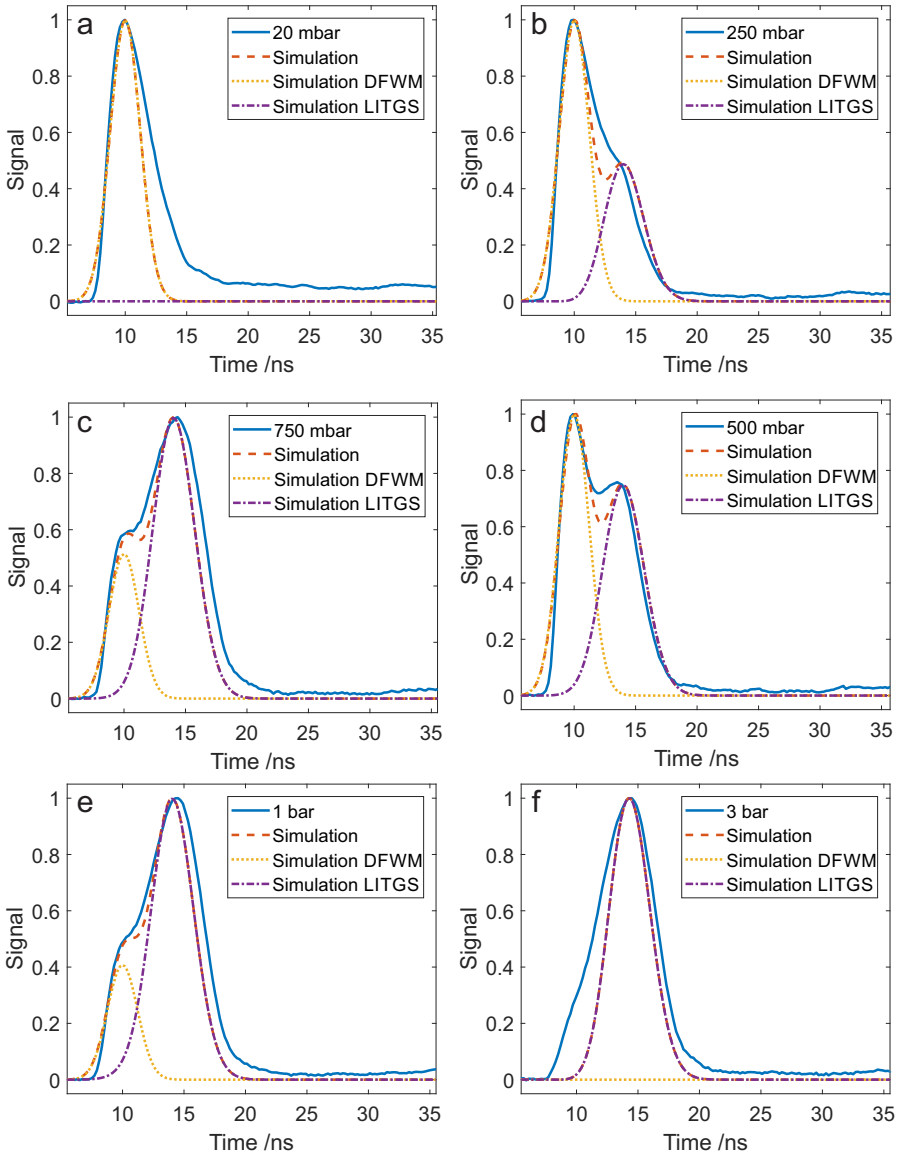


Figure 5.9: Experimental time profiles of DFWM signals (solid blue line) in 20 mbar of NO and with increasing pressure of N_2 from 0-3 bar (figures a-f). Simulated signals (dashed red line) are the result of the addition of the simulated DFWM contirbution (dashed yellow line) and a simulated LITGS contribution (dashed purple line). Note that at the lowest pressure (figure a), the LITGS component is negligible and at the highest pressure (figure f), the DFWM component is relatively insignificant.

the best fit to the signal in this case. However careful modelling and knowledge of the gas dynamic parameters could enable isolation of the DFWM and LITGS contributions to signal and thus provide useful information about the target species simultaneously from these two techniques.

5.4 Combined DFWM and CW LITGS

In addition to identifying both DFWM and LITGS effects in a single signal as described above, with the addition of a continuous wave (CW) probe, a separate, continuous LITGS signal can be generated simultaneously to show the long-term behaviour of the LITGS signal. This is useful because very precise temperatures can be derived from continuous LITGS signals as described in Chapter 3 and these measurements are unaffected by competition with the DFWM process. Using these techniques simultaneously thus has the potential of providing additional information for calibration or corroboration with minimal additional equipment or optical access requirements. Little has been previously shown in the literature of using these two techniques together (rather than treating one as the parasite of the other) and the potential benefits to spectroscopy. Here we successfully use these techniques simultaneously and identify regimes in which both effects are present and describe how the combined technique could be further developed.

DFWM and cw LITGS signals were generated simultaneously in NO. The same 226 nm pump beams as above are used to generate the population grating and thermal grating. For DFWM, the grating is again probed by a third pulse at 226 nm in the forward folded BOXCARS geometry, resulting in the same pulsed DFWM

signal in the forward direction, separated by the small angle equal to that between probe and pumps. For CW LITGS, the grating is probed with a continuous beam at 671 nm incident at the Bragg angle appropriate to its wavelength and the signal detected at the Bragg equivalent angle.

Figure 5.10 shows these simultaneous signals for varying pressures of N_2 between 100 mbar and 4 bar. Above 200 mbar the oscillatory behaviour of the LITGS signal becomes sufficiently apparent to provide increasingly precise temperature measurement as the pressure is increased. The DFWM signal could be used here, for example, to derive NO concentration and the LITGS signal to derive temperature.

As described in the previous section, the behaviour of the signal strength of the two effects with increased pressure is opposite. The DFWM signal falls rapidly with increased pressure and then levels off as the signal becomes LITGS-dominated (Figure 5.11 (a)). The pure continuous LITGS signal strength can be seen to increase as pressure increases and then level off (Figure 5.11(b)). The pressure-induced collision rate in this case increases to a level so that the maximum energy transfer is achieved during the excitation pulse.

5.5 Effect of DFWM probe on CW LITGS signal

With the combined DFWM and cw LITGS experimental setup described above, another competition can be rendered visible between the DFWM process and the cw LITGS process. DFWM is a parametric process leaving molecules back in the ground state, which leaves fewer molecules in an upper state available to transfer their energy via collisions into a thermal grating. By blocking and unblocking the

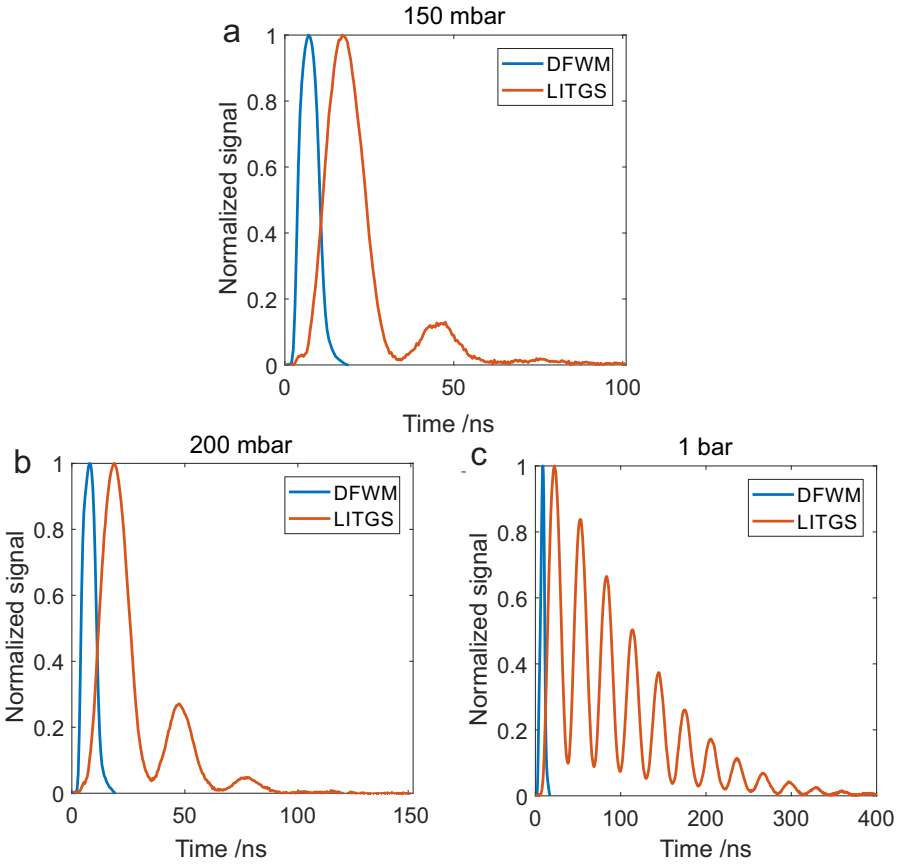


Figure 5.10: DFWM and LITGS signals recorded simultaneously for increasing pressure of N_2 buffer gas at (a) 100 mbar, (b) 200 mbar and (c) 1000 mbar. The data are averages over 100 single shots. The blue line shows the DFWM signal produced by a pulse intensity approximately equal to the saturation value at 1 bar.

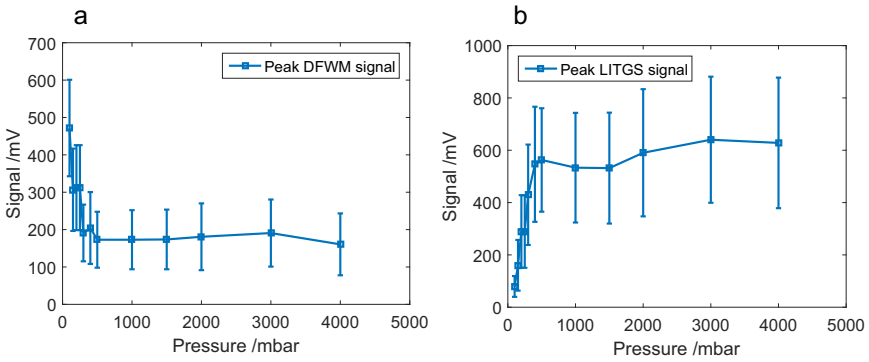


Figure 5.11: Amplitude of the (a) DFWM and (b) cw LITGS signals with increasing pressure, illustrating the opposite dependency on pressure.

third degenerate beam, and thus adding and removing this de-populating effect, the thermal grating is strengthened and weakened accordingly. We can see this in the form of the cw LITGS signal strength becoming larger when the DFWM probe beam is blocked and thus more energy is available in the thermal grating, and the signal becoming smaller when the DFWM probe is allowed to participate in the mixing process and thus the thermal grating is weaker.

When the degenerate probe pulse at 226 nm was incident on the induced grating at the same time as the LITGS probe beam at 671 nm the intensity of the LITGS signal was observed to decrease as shown in Figure 5.12. At a total pressure of 500 mbar with unsaturating pump and probe intensity the addition of the DFWM probe reduces the LITGS signal intensity by a factor of 1.7. When saturating pumps and probe are used the reduction factor is 1.1. In the unsaturated case the DFWM is relatively more effective in competing with collisional relaxation, thus reducing the amount of energy available for transfer to the thermal grating. Under saturating pump conditions, the excited state population is more effectively re-pumped thus allowing more energy to be transferred to the thermal grating.*

At the higher pressure of 3 bar the change in the LITGS signal intensity induced by the DFWM probe is not statistically significant relative to measurement error. At these higher pressures the population dynamics are dominated by the higher collision rate, and so the de-excitation by the degenerate DFWM probe is relatively insignificant. Furthermore, at the higher pressure the intensity required to saturate is higher, as described above, so when the same intensity is used at 500 mbar and 3 bar, the saturation effect is reduced at the higher pressure relative to the

*The measurements were performed at 500 μJ and 120 μJ.

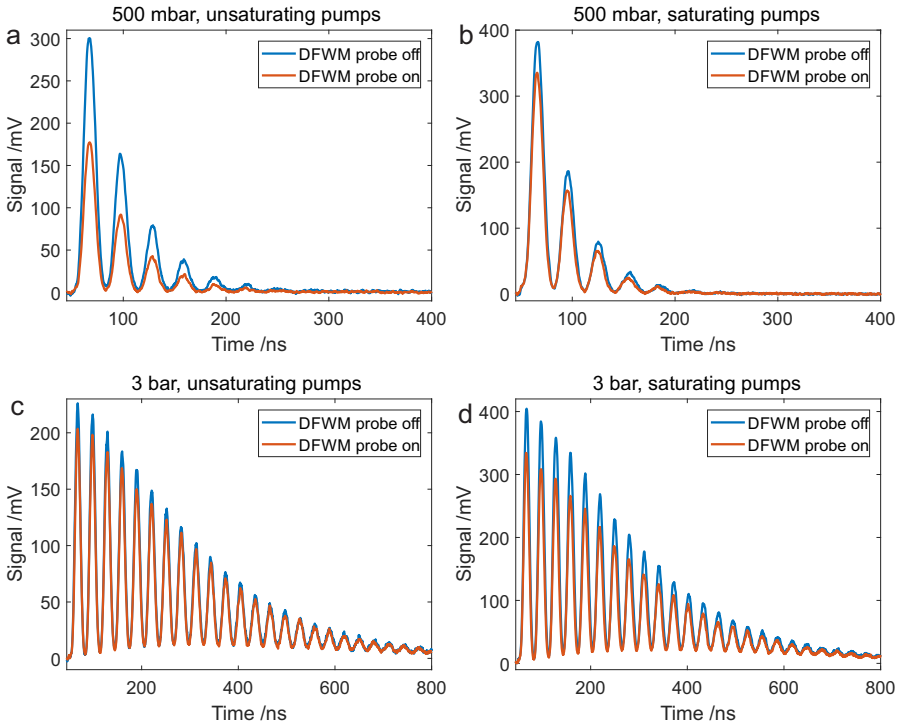


Figure 5.12: Simultaneously recorded DFWM and LITGS averaged signals showing the effect of the degenerate probe used for DFWM on the magnitude of the LITGS signals. The blue lines show the LITGS signal in the absence of the degenerate probe used for DFWM and the red line the signal in the presence of the degenerate probe. (a) and (b) show unsaturated and saturated pump conditions at 500 mbar. (c) and (d) show the effect of the DFWM probe at 3 bar where the observed difference in the LITGS signal is not statistically significant.

unsaturated case. As described above, an upper bound for the saturation intensity was calculated to be 650 μJ at 1 bar. It is likely that the 500 mbar case in Figure 5.12 is highly saturated and that the 3 bar case is mostly unsaturated.

5.6 Summary

The effects of pressure on a DFWM signal have been explored. The transition from DFWM- to LITGS-dominated signals have been rendered visible and the

role of saturation discussed. Intermediate scenarios where both effects are present have been shown and qualitative modelling shown how these effects could be distinguished from each other. DFWM and cw LITGS signals have been produced simultaneously in a pressurised NO optical cell and regimes identified where the two signals could be used simultaneously in experimental situations. Unfortunately, in the case of turbulent combustion within a gas turbine engine, which operate at high pressure, producing a DFWM signal simultaneously with a CW LITGS signal would be difficult owing to the very high energy requirements which would be needed to saturate the DFWM process and thus enable the signal to survive higher pressures. This was not practical in our setup and so further work was conducted with LITGS signals only in the work that follows in Chapters 6 and 7.

Chapter 6

LITGS in nitric oxide in non-combusting gas mixtures

6.1 Introduction

LITGS measurements were made in NO with an N_2 buffer gas in a non-combusting gas mixture in an optical cell. Signals were produced over a range of temperatures around ambient, with NO partial pressures of 0.5 mbar to 100 mbar and total chamber pressures, with N_2 buffer gas, ranging from 200 mbar to 5 bar. These measurements then served to validate the inherent limitations to accuracy and precision and to provide calibration for flame-based measurements of Chapter 7.

A known temperature and gas composition were used to derive the grating spacing using Equation 3.10. Temperature was varied around ambient conditions using a heating coil and temperature measurements were derived from LITGS signals. Precision and accuracy limitations of LITGS temperature measurements

with our setup were explored. Pressure was derived from signal shape using a fitting model and known gas dynamic parameters and, more simply, via the signal decay rate. The effects of NO concentration on signal strength were explored and a discussion presented of how these effects could be used to extract an indication, albeit imprecise, of species concentration simultaneously with temperature and pressure information and with no additional experimental cost.

6.2 LITGS thermometry in NO

6.2.1 Derived temperatures from FFT of LITGS signal

Obtaining a temperature measurement requires identifying the frequency of the acoustic oscillation of the signal. The Fourier transform of a signal is used to determine its characteristic frequency. Taking the Fourier transform of the signal enables information from the entire signal to be used, as it is encoded in the power spectrum, and avoids the need to identify the maximum peak of each oscillation and associated sources of error.

MATLAB offers Fast Fourier Transform (FFT) routines and this enables very fast processing of experimental data. A MATLAB based program for FFT analysis of LITGS signals was previously written by Rob Stevens and further developed by Ben Williams and used in this work [78, 84]. In this way, oscillation frequencies for many LITGS signals can be obtained in a matter of seconds making the processing of large data sets and finding average values quick and easy.

Figure 6.1 shows a representative LITGS signal and its Fourier transform. As can be seen in the figure, the Fourier transform consists of an exponential

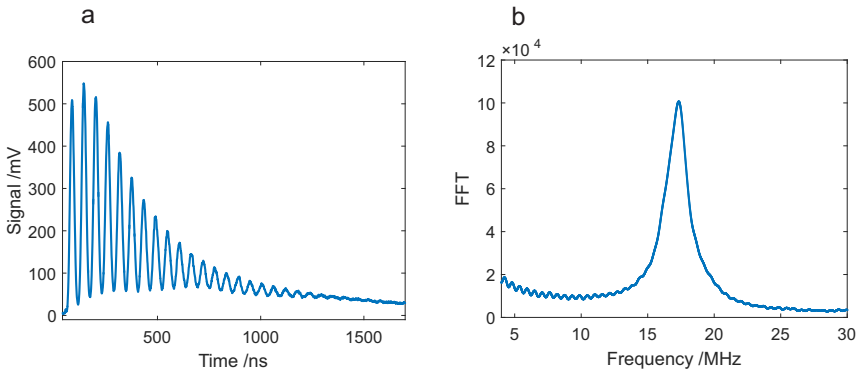


Figure 6.1: An example of a LITGS signal and its FFT. The temperature and gas composition were measured independently and from the frequency the grating spacing, Λ, was derived.

decay centred at the origin generated from the exponential decay of the overall LITGS signal, and a peak generated by the acoustic oscillation and centred at the oscillation frequency. Smaller, high frequency contributions can also be generated due to the finite duration of the signal and sharp leading edge. Where there are strong signals with many oscillations, the oscillation frequency of the signal can be determined with high precision from the FFT. For weaker signals with few oscillations, obtaining a clear maximum in the power spectrum can be more challenging and other methods are used, of which more will be said below.

6.2.2 Derived temperature in NO in an optical cell

LITGS signals were produced in the pressure chamber at various temperatures to demonstrate the setup for temperature measurements and to derive precision and accuracy limits. The cell temperature could be adjusted over a small range around ambient with a heating coil. Figure 6.2(a) shows averaged LITGS signals over 100 single-shots in the cell at four different temperatures. These measurements were

taken at 3 bar total chamber pressure.

The values of the acoustic modulation frequency are readily and accurately determined from the Fourier transforms shown in Figure 6.2(b). The temperature is calculated to range from $290 - 320$ K and is in close agreement with independent measurements obtained via thermocouple.

6.2.3 Temperature measurement uncertainty

The accuracy and precision of temperature measurements depends on evaluation of sources of systematic error and random fluctuations associated with variations in the measurement region and of the optical system.

The accuracy of the temperature value derived from the LITGS signal depends upon having an accurate measure of the grating spacing, Λ and an accurate value of the gas composition and thus values of γ/m upon which the derived temperature depends in accordance with equation 6.1

$$T = \frac{m\Lambda^2}{\gamma k_B} f^2 \tag{6.1}$$

The precision of the measurement depends on the degree to which the modulation frequency can be determined. Strong, stable and long lasting signals will result in more precise determinations of frequency whereas weak, short signals, with few oscillations, will introduce greater uncertainty. Precision can often be improved by averaging signals over time when average temperatures are sufficient rather than single shot signals which have the advantage of temporal resolution.

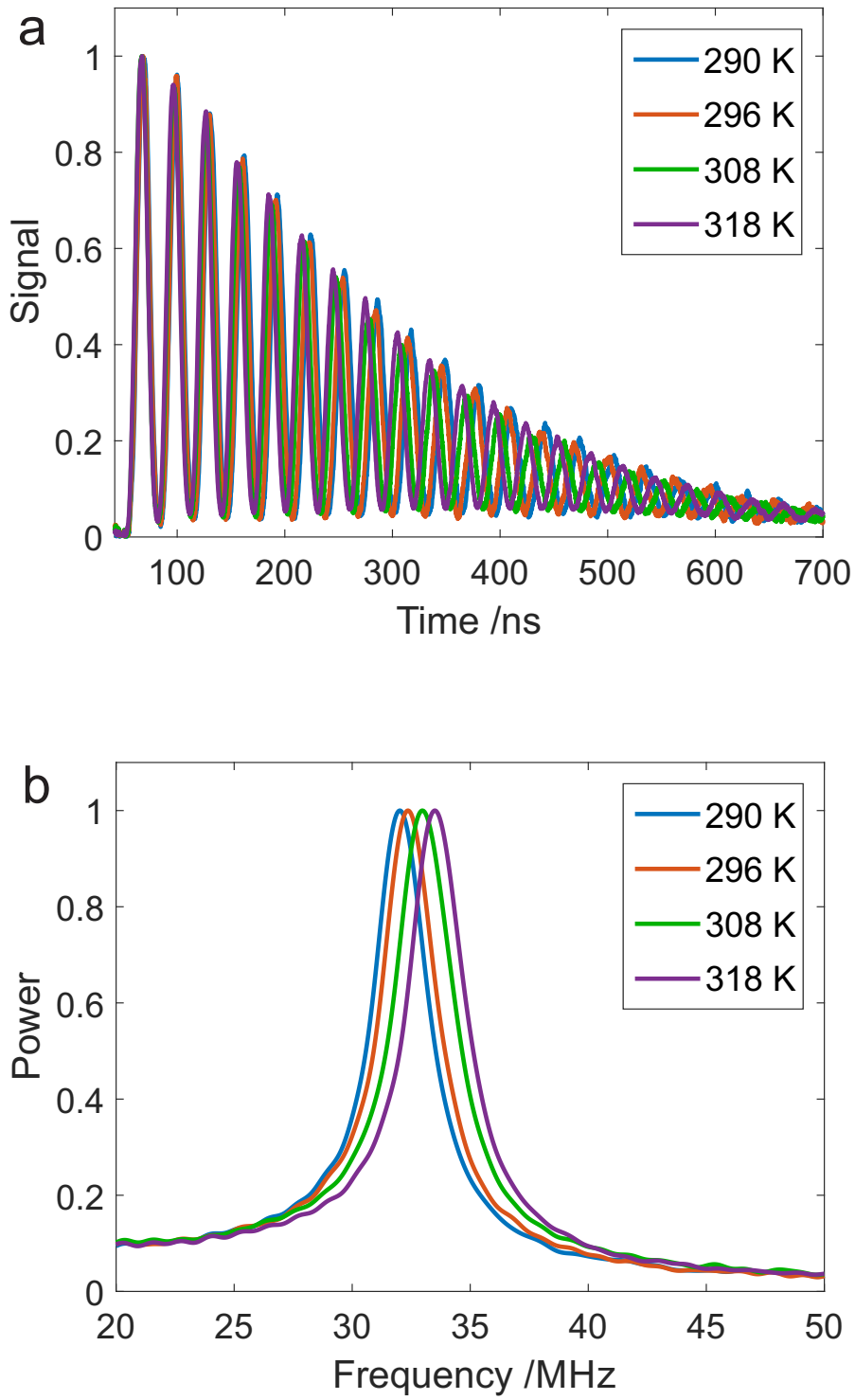


Figure 6.2: (a) Measurements in test cell with 20 mbar NO and 3 bar N_2, 100-shot averaged LITGS signals at temperatures between 290 and 320 K. (b) Fourier transform of signals showing good resolution of the fundamental acoustic frequency f.

Grating spacing, Λ, calibration

The spacing, Λ, between gratings in the interference pattern generated by the two pump beams can be estimated from measurement of the geometric arrangement of the beams. However doing so results in uncertainties that translate into large uncertainties in derived temperatures. A more accurate method for determining Λ is by use of calibration under known conditions. This calibrated value of Λ can then applied in subsequent measurements so long as the system setup is left unchanged.

Calibration measurements were carried out using the pressurised optical cell at temperatures around ambient but with elevated pressure to increase the accuracy in measuring the acoustic modulation frequency. The cell was filled with a gas mixture containing NO at a partial pressure of 20 mbar and 3 bar of N_2. The cell temperature was monitored using a Tenma K-Type (nickel chromium - nickel silicon) temperature probe. The signal-to-noise ratio for the cell-based measurements at ambient temperatures and at pressures in the range 1-3 bar were of sufficiently high quality to allow accurate determination of oscillation frequency from a Fourier transform of the signal.

The signal in Figure 6.1 is a room temperature LITGS signal and its Fourier transform that was generated in NO in the pressurised optical cell, with a known gas composition. The temperature was measured independently via the thermocouple to be 294 K. The oscillation frequency of the signal was determined to be 17.33 MHz. Using the gas constants for N_2 at room temperature, $\gamma = 1.401$ and $m = 28.01$ g/mole, the grating spacing was determined to be 20.25μm ($\pm$0.05μm). The remaining uncertainty in this value derives from instrument error associated with

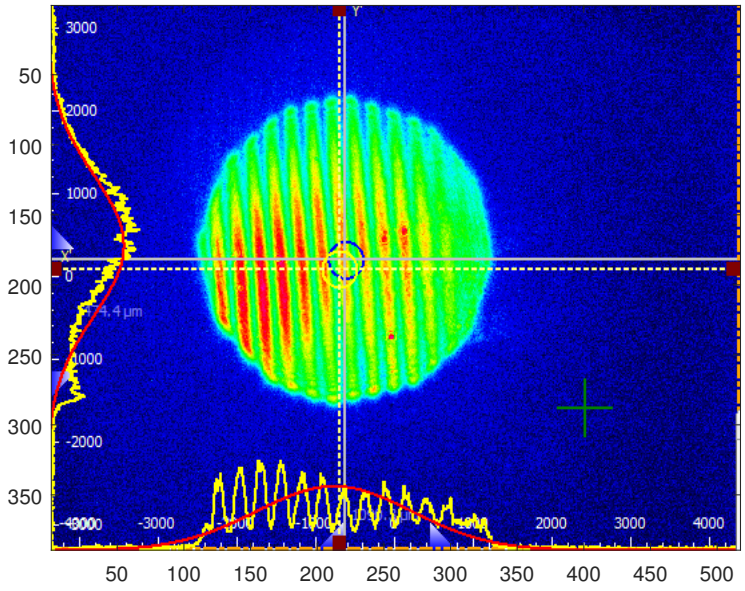


Figure 6.3: Image of the LITGS grating produced by pump beams used this work.

the temperature probe used for temperature calibration and uncertainty in the measured concentration of NO and N_2 buffer gas added to the optical cell. This grating spacing was applied in temperature derivations throughout much of the work that follows. In some cases, in which the setup was altered, a different grating spacing was used which was derived in the same way.

The grating spacing was also measured independently by imaging it with a Thorlabs BC106N-UV CCD Camera Beam Profiler and measuring the spacing between planes as shown in Figure 6.3. Using this less precise method, the grating spacing was confirmed to be approximately 20 μm. The grating was also observed under ambient and flame conditions using this approach and shown to remain constant over the full range of temperatures explored here.

The gas composition is known well in these cell-based measurements and therefore uncertainty of γ and m can be determined with a high degree of confidence and contributes negligible additional uncertainty to derived temperature measurements.

LITGS model

The precision of the temperature measurement depends on the consistency of the signal frequency from shot to shot and the ability to derive a precise frequency from the signal. Where there are strong, consistent signals with many oscillations, the FFT approach can provide high precision results. However, for weaker signals obtained at flame temperatures or lower pressures, there are often too few oscillation peaks and the decay rate is too great such that the FFT approach fails to yield a precise peak in frequency space.

An alternative to simply calculating the FFT of the signal to determine oscillation frequency, as described above, is to fit a theoretical model to the signal. This involves a fitting routine that repeatedly calculates a theoretical signal and compares to input data in an iterative loop. As a result, fitting is a much more computationally expensive method than the single FFT evaluation for extracting temperature information from a LITGS signal. The benefit, however, is the ability to extract temperature information from weak signals with rapid decay rates, such is often the case in high temperature combustion environments.

A best-fit model was developed by the group based on the approach of Paul *et al* [73]. The model was adapted for application to fit in the frequency domain by Stevens [84]. A brief overview of its primary features is given here. For further detail see the references above.

The model is designed to optimise up to five parameters including:

- Acoustic wave transit time between grating planes, τ
- Reynolds number, Re
- A "fast" quenching rate, Q_1
- A "slow" quenching rate, Q_2
- A branching ratio between Q_1 and Q_2

τ is the inverse of the acoustic oscillation frequency and is therefore the main parameter of interest for thermometry, since it is from the frequency of the signal that temperature is derived. The Reynolds number provides the mechanism for the model to represent the effect of pressure on the signal. The two quenching rates and their branching ratio characterise the collisional energy transfer to the thermal grating. While these factors influence the shape of the signal, their influence on signal frequency is minimal.

A non-linear least squares fitting function, standard in MATLAB, is used to identify the best fit values of these parameters. 95% confidence intervals are returned from the fitting routine for these parameters, which give an indication of the goodness of fit and the inherent error in determining signal frequency.

Cumulative error in optical cell temperature measurements

Figure 6.4 shows time-averaged LITGS signals and the model fit, described above. From these an oscillation frequency has been determined and temperature derived with associated error.

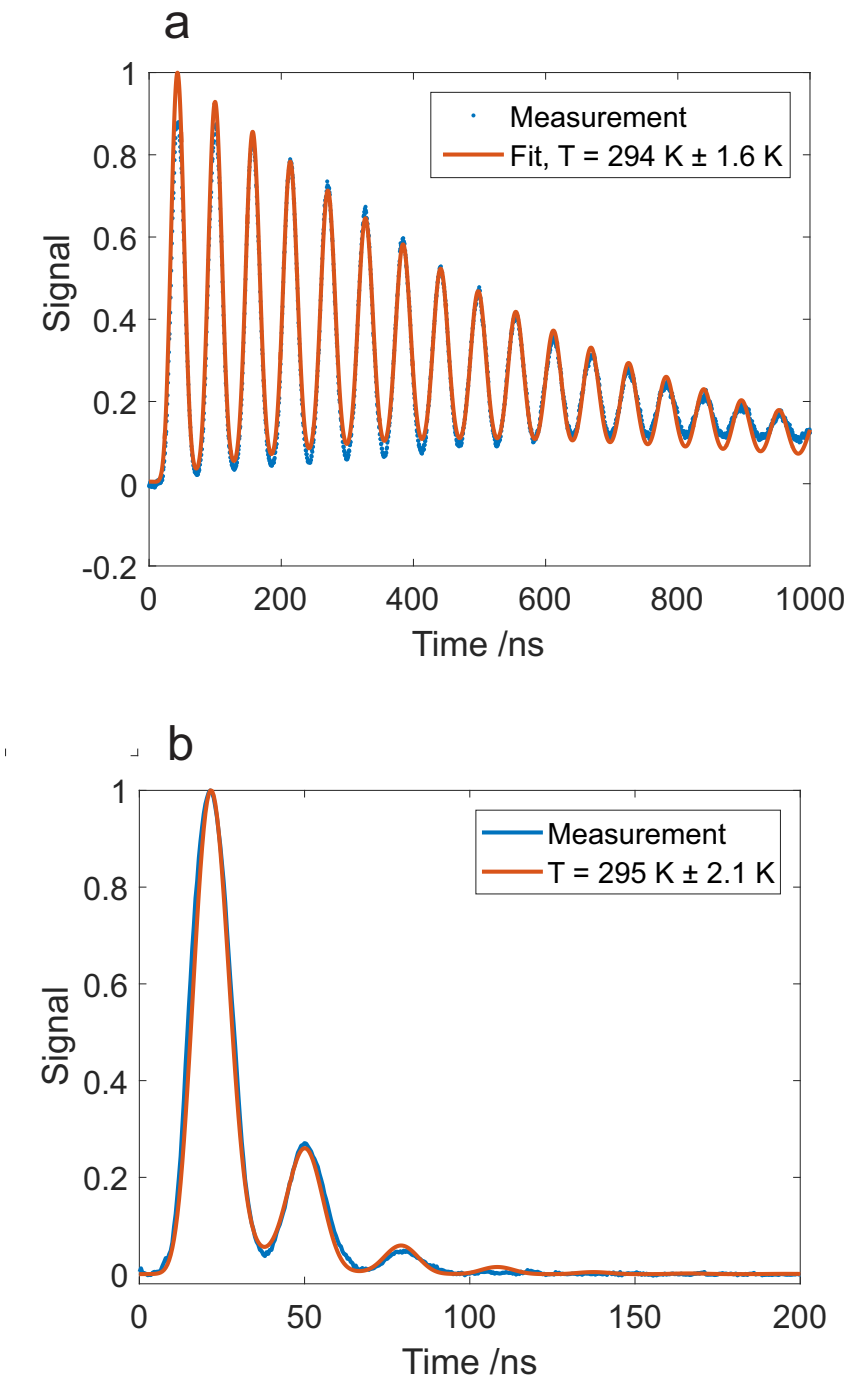


Figure 6.4: 100-shot averaged LITGS signals with best-fit model signal at (a) 3 bar and at (b) 200 mbar total pressure and room temperatures, 295 K. This signal duration of the 200 mbar signal is more typical of signals at flame temperatures and atmospheric pressure.

Figure 6.4 (a) shows a fitted LITGS signal recorded in a gas cell with 20 mbar NO and total pressure of 3 bar. Derived temperature is 294 K with a total uncertainty of 1.6 K or 0.5%. The strong, long lasting signal at high pressure means that oscillation frequency can be determined with a high degree of precision.

A corresponding measure of precision under simulated flame conditions was estimated by reducing the cell pressure to 200 mbar at room temperature, as shown in Figure 6.4 (b) to give a LITGS signal having a comparable duration to that at flame temperatures at 1 bar. This low-pressure room temperature signal has many fewer oscillations before the signal disappears. The signal in this case is an average of 50 shots. Shots with too low signal-to-noise ratios have been removed to increase reliability of the temperature fit.

The values for Λ and γ/m and inherent uncertainties associated with them remain the same in both conditions, however uncertainty associated with the goodness of fit and thus error in measured oscillation frequency has increased for the low pressure signal. Total measurement error as a result is 2.1 K for the 200 mbar case, or 0.7%.

The shot-to-shot variation in measured oscillation frequency in the cell gives a measure of the single-shot precision of the technique for measurements at a given temperature and pressure. Estimates of single-shot precision inherent in the technique were obtained from the standard deviations of batches of up to 100 single shots as shown in the histograms of figure 6.5. In this case, the model described above was used to fit each individual shot and the frequency, and thus temperature, was derived from the modelled signal. The red line shows the mean temperatures, plus and minus the standard deviation of the fitted temperatures.

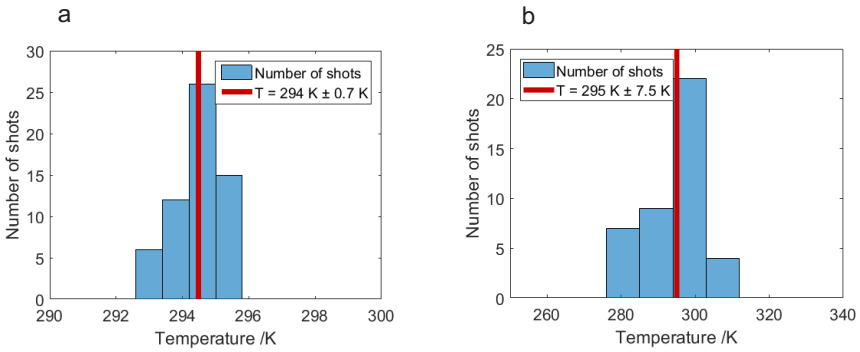


Figure 6.5: Histograms of single shot measurements at (a) 3 bar total cell pressure and (b) 200 mbar total pressure. The red line indicates the mean temperature value and line width indicates one standard deviation.

Figure 6.5 (a) shows the standard deviation of the temperature derived from 100 single shots at room temperature and 3 bar total pressure. At this high pressure, with strong signals and many oscillations, the shot-to-shot spread in the temperature is very small. The standard deviation of the single shots at room temperature, 295 K was ± 0.7 K, or 0.2%. At these high pressures and stable conditions, single shot precision is on par with that of time-averaged data.

For the simulated flame signals taken at 200 mbar total cell pressure, however, the standard deviation increased to $7.5K$, indicating the inherent precision for single-shot measurement with flame-like signals. In this case the average signal demonstrates a marked reduction in measurement uncertainty over the single-shot measurement. Uncertainties in measurements in flame conditions, however, will be affected by additional factors such as flame flicker.

The measurement error shown here is superior to what is possible with other optical techniques and shows promise of providing sufficient resolution for the measurement needs within gas turbine engines, described in Chapter 2. These measurements form the basis for temperature measurements using LITGS in NO

in a flame which will be described in the next chapter.

6.3 NO species concentration effects on LITGS signal

The effects of concentration on signal strength were explored in the optical cell. Measurements were taken at room temperature and using non-saturating pump beam energy. As shown in figure 6.6, the signal rises with increased NO concentration then peaks and falls as the medium is no longer optically thin. Total cell pressure has an affect on the behaviour as the peak is seen to appear at lower concentrations of NO at 3 bar total pressure compared with the 0.5 bar total pressure case. However, the general trend is the same.

Figure 6.7 shows that at low concentrations, for NO partial pressures below about 10 mbar, the signal is proportional to concentration squared. At higher concentration, the curve deviates from this behaviour. This is most likely due to absorption effects such as seen in similar experiments with DFWM, eg [119]. This deviation begins at lower NO partial pressure and is more pronounced at 3 bar compared to 0.5 bar.

At these lower concentrations it may be possible to derive species number density from the integral of the LITGS signal. The integral of the LITGS signal is approximately proportional to the square of the number density (N) and the unsaturated pump laser intensity and directly proportional to probe intensity, the absorption cross section, the interaction region volume and the total pressure, several of these parameters are also temperature dependent. The signal is also

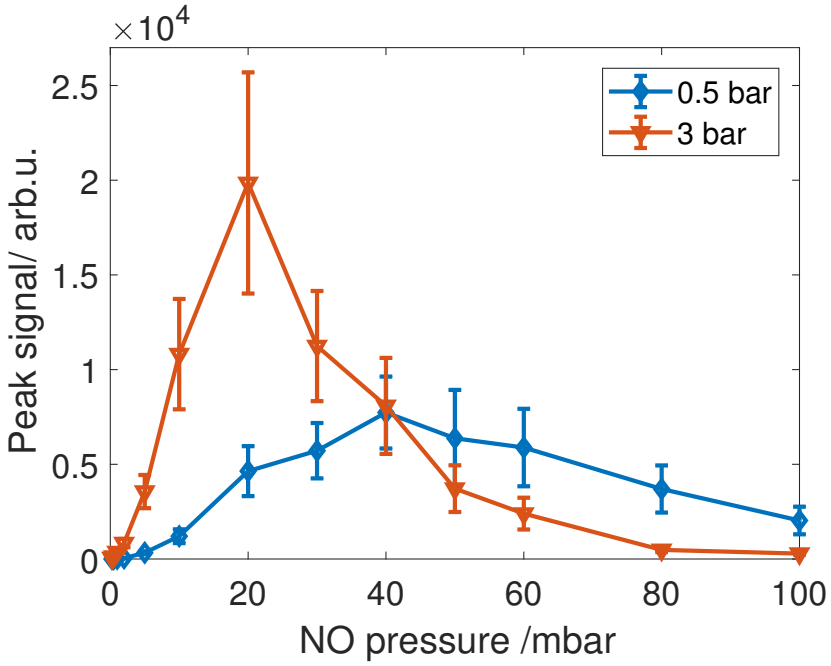


Figure 6.6: LITGS peak signal strength with increasing NO concentration from 1-100 mbar and N_2 buffer gas at 0.5 bar and 3 bar

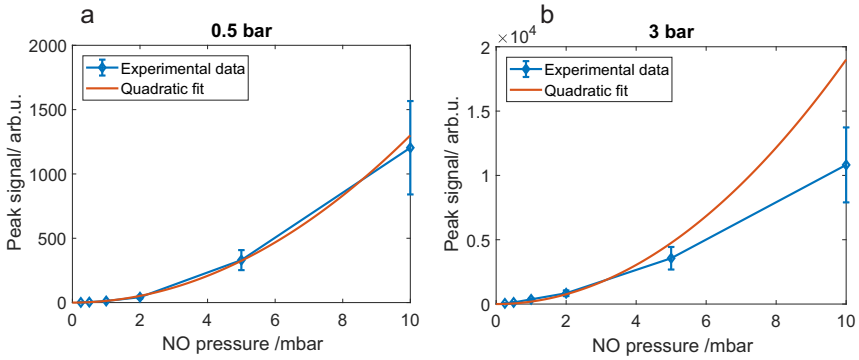


Figure 6.7: LITGS peak signal strength with increasing NO concentration from 0.1-10 mbar and N_2 buffer gas of (a) 500 mbar and (b) 3 bar fitted with quadratic $y = ax^2$

dependant on factors such as the goodness of the alignment and PMT gain. As a result, deriving an accurate concentration estimate from a LITGS signal is complicated by controlling for these many factors.

Nevertheless, it may be possible to estimate concentration from signal strength if these other variables affecting signal strength can be controlled or determined. The alignment and PMT gain settings can be held constant and therefore removed as a factor so long as a calibration measurement, at known concentration, can be taken. The pressure effects could also be corrected for via a prior calibration. The temperature can be derived from the LITGS signal itself and thus used to determine the correct value of σ. Depending on the transition lines of interest, this may or may not vary significantly across a broad range of temperatures. For NO at 226 nm, for example, the absorption cross section varies by less than 2% across the full range of flame temperatures that were measured [111]. The pump and probe laser intensity can be measured and any fluctuations corrected for in post-processing.

For unsaturated pump laser energies and at NO concentrations which show a quadratic dependence as shown in figure 6.7 this suggests that average number density could be estimated from the signal. Single shot number densities would require also correcting for any jitter in frequency from the laser which would introduce another source of error.

6.4 LITGS barometry in NO

We demonstrate the ability to derive pressure from the signal in the pressurised optical cell. Pressure affects the signal decay rate and we can use the LITGS model to fit our signals and then extract pressure information. We compare these to pressures from a pressure gauge to test our model accuracy in a cell and then later apply the same model to our combusting flow and to engine data [120]. While there has been some previous work done on deriving pressure from LITGS signals [85], it has been done at higher pressures. The present work also demonstrates how we might generate useful pressure data in a very computationally inexpensive way and applies the technique within two combustion applications.

6.4.1 Pressure derived from fitted model

LITGS signals were again generated experimentally at various total cell pressures, using N_2 as a buffer gas. In this case the experimental setup was modified to increase beam size and remove a potentially competing cause of signal decay - the time for the acoustic waves to transit the interaction region being shorter than the acoustic damping time. This resulted in a fringe grating spacing of 8.4 μm.

The signal shape (decay rate) can be observed in Figure 6.8 to change over a range of pressures from 500 mbar to 5 bar, as measured with a pressure gauge, with the signal decaying more quickly at low pressure.

The theoretical LITGS model described earlier was again used to obtain a "best fit" to the experimental data and from the model a value for the Reynolds number was obtained. The Reynolds number is dependent upon the underlying gas kinetic

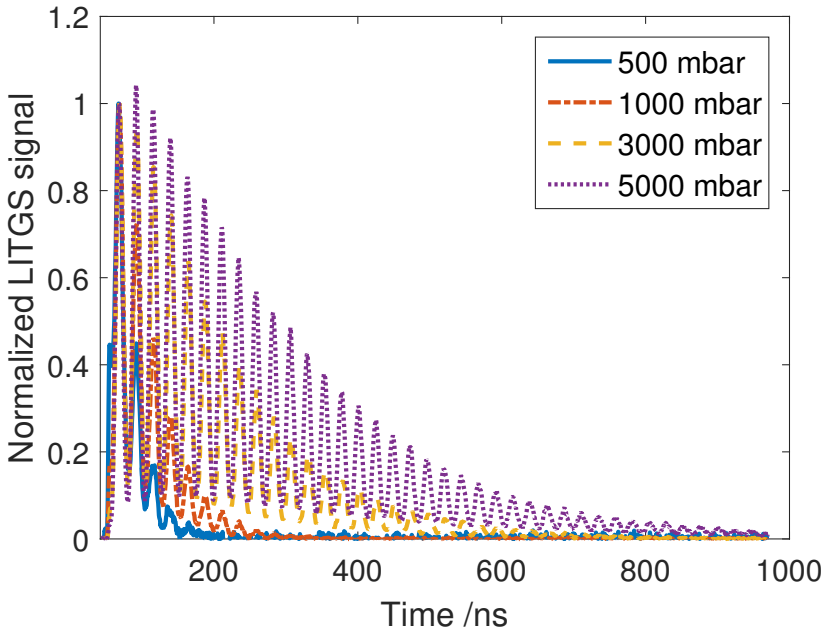


Figure 6.8: LITGS signals generated in NO with N_2 buffer gas from 500 mbar to 5 bar total pressure.

parameters and so long as these, the temperature and gas composition can be reasonably known, a value for pressure can be obtained from the following relation:

$$P = \frac{\mu k_B T Re}{c_s \Lambda m} \tag{6.2}$$

where μ is the dynamic viscosity of the gas, c_s is the sound speed, m is the mean molecular mass of the gas, k_B is Boltzmann's constant and Λ is the grating spacing. The value for temperature can be determined from the LITGS signal itself. In general, and especially at elevated pressures, the use of the ideal gas law to derive thermodynamic parameters becomes problematic and so an iterative optimisation procedure was used with data provided from the NIST Reference Fluid Thermodynamic and Transport Properties (REFPROP) database for the

relevant kinetic parameters [121] to take account of the pressure-dependence of these parameters.

Fitting method

As described previously, the LITGS model seeks to fit the oscillation period, τ, the Reynolds number, two quenching rates, Q_1 and Q_2, and the split between them. One challenge with the fitting routine is that not all parameters are orthogonal. The Reynolds number affects the decay of the LITGS signal but so too does the quench rates, especially Q_2. To account for this, a sensitivity study was conducted in order to identify a range of values for Q_2 and for the split between quenching rates and it was found that these vary little with pressure and temperature across the range of conditions of this work. The second quench rate, Q_2, has therefore been fixed in this case and was solved for from one known pressure calibration point which was measured independently (i.e. ambient pressure).

Average LITGS signals from 100 single shots are shown in Figure 6.9 along with the fitted model. Q_2 has been fixed at 60 ns and the split between Q_1 and Q_2 of 95% to 5%.

Derived pressure

Measurements were performed in the optical cell with 3.5 mbar of NO and N_2 buffer gas ranging from 500 mbar to 5 bar. Figure 6.10 shows the cell pressure calculated from the fitted signals compared to measured gauge pressure. Each point represents 100 single shots and the error bars indicate the standard deviation. A good agreement was achieved along the full pressure range measured with maximum

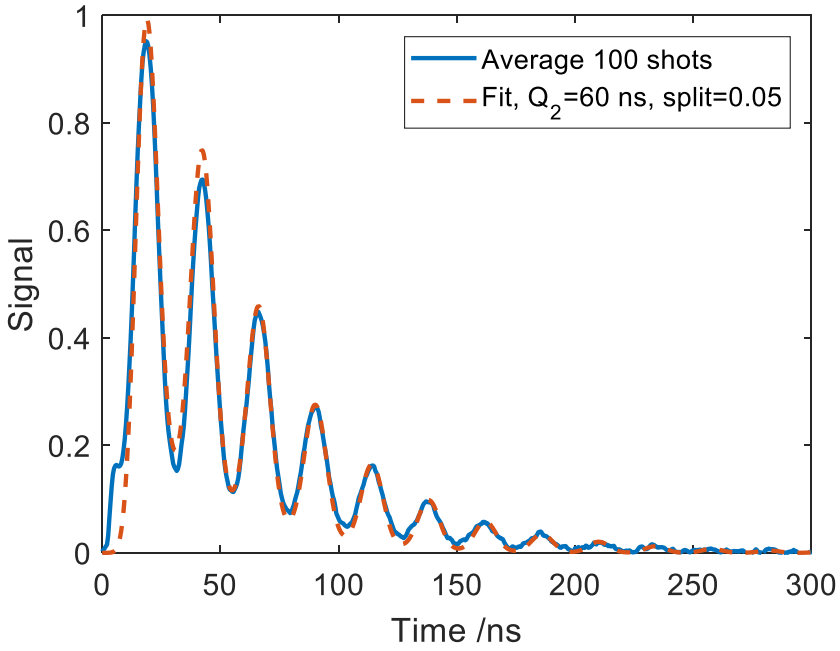


Figure 6.9: Average LITGS signal produced from 100 shots and theoretical best fit with fixed quench rate, Q_2 and split between quench rates

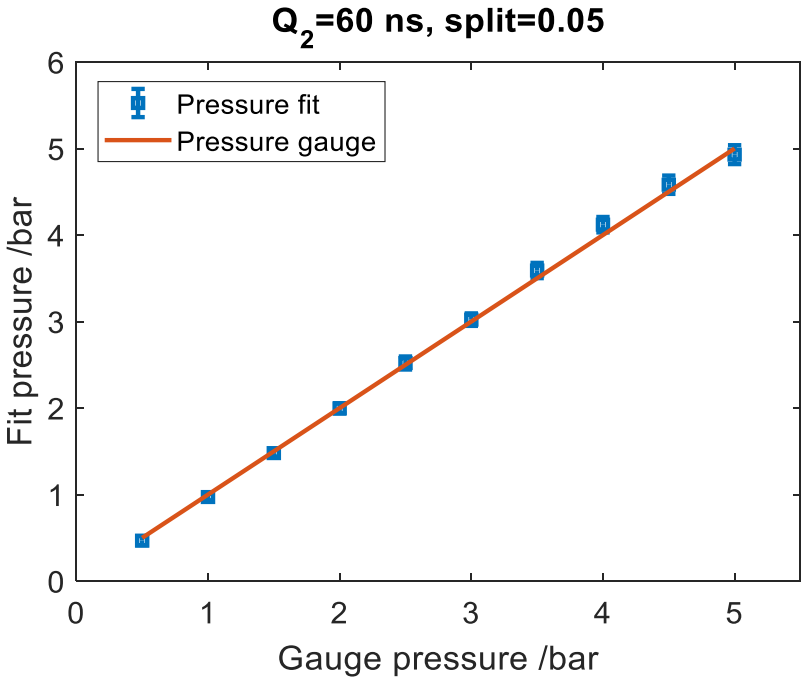


Figure 6.10: Derived pressure from LITGS signals in an optical cell with increasing N_2 buffer gas versus measured gauge pressure for 100 shots and standard deviation

deviation of 0.12 bar or 6%. As described above, the dependance upon the value of Q_2 was tested and shown that changing the value by ± 10 ns only affects the pressure by ± 0.02 bar.

These measurements and approach serve as a basis for measurements conducted in a flame (described in Chapter 7) and in an optical engine [120].

6.4.2 Pressure derived from signal decay

A complementary approach, developed by Willman *et al* [120], is also demonstrated using a "gradient method" to derive pressure directly from the rate of decay of the LITGS signal by extracting a nominal 'gradient' value which can be associated

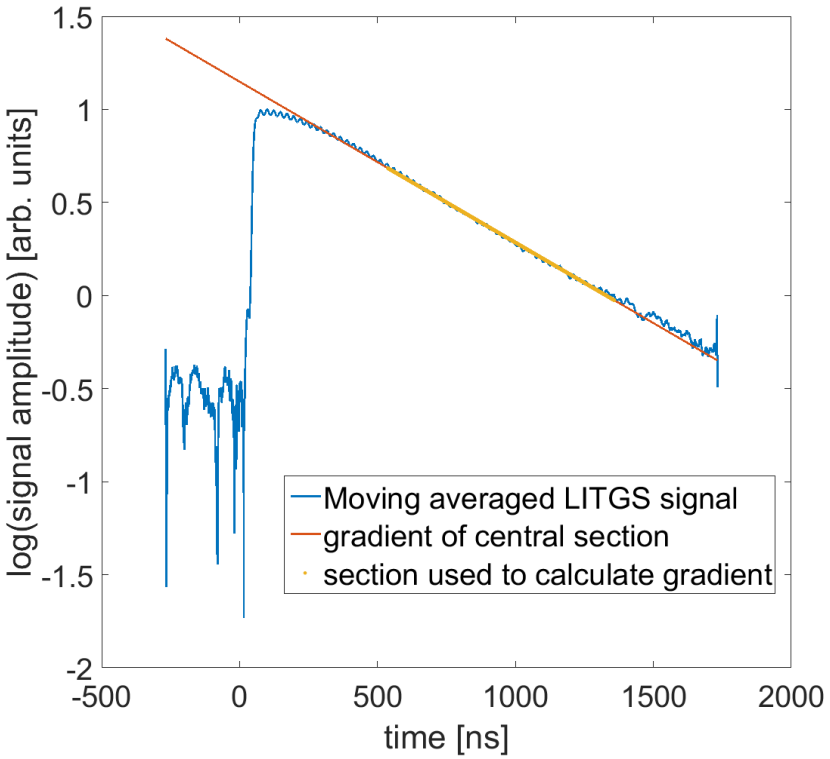


Figure 6.11: Smoothed LITGS signal with gradient fit to the exponential decay of the signal.

with the decay constant of the exponential decay. Where a full calibration along the range of temperatures and pressures of interest can first be made, either from experimental data or via modelled signals, this technique can then enable fast processing of real time pressures measurements within this range of application.

In this method, the signal is first smoothed in post processing with a moving average to remove acoustic oscillations. The window width is set to match the peak-to-peak separation to leave only the underlying decay. The log of the smoothed signal is then taken and a region defined over which to calculate the gradient. This is shown in Figure 6.11. In practice this means removing the first part of the signal in which quenching effects complicate the signal shape and the later tail of

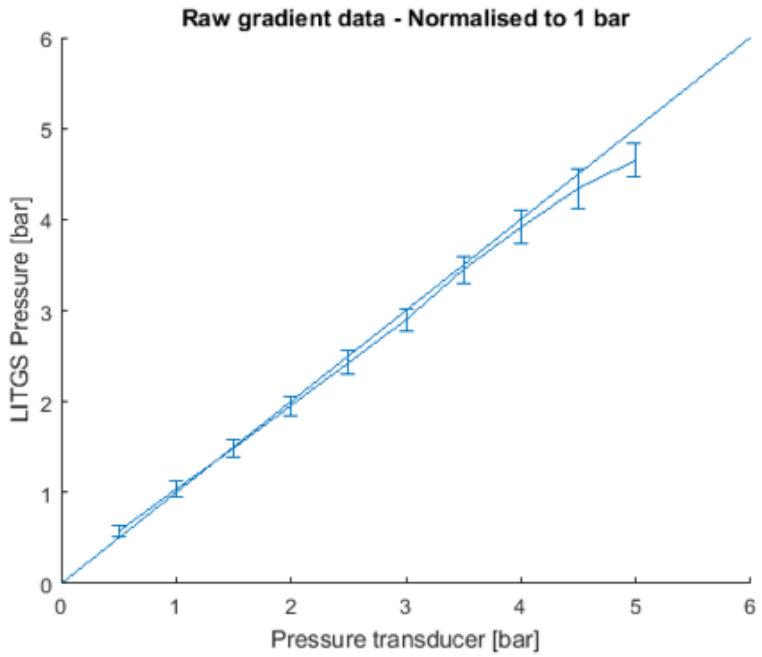


Figure 6.12: Derived pressure using the gradient approach with a single point calibration compared to measured gauge pressure.

the signal in which noise begins to become a factor. This gradient can then be considered an un-calibrated pressure measurement.

Once the gradient value has been established a calibration must be applied to convert to pressure. This can be accomplished in a number of ways which may have advantages or disadvantages to different experimental needs. In cases where the gas composition and temperature are held constant with increasing pressure a single calibration point is found to produce reasonable results across a limited range of pressures. Figure 6.12 again shows derived pressure versus gauge pressure, this time using the gradient method with a single point calibration. The results are similar to those of the full fitting method described above but produced in a much more computationally efficient manner.

In more complex environments, this single-point calibration is insufficient to produce accurate results. In these cases an alternative approach would be to perform a "self-calibration" in which data is taken across a full range of pressures of interest and the full LITGS fitting model approach described in the section above or an independent measure of pressure is used to define a calibration for each gradient point. The value of the gradient approach described here is then no longer predictive but useful in cases where intermediate pressures or fast-processing is valuable.

Finally, calibration of the gradient approach can be achieved by modelling signals over a broad range of temperatures and pressures of interest. In this case, pre-calculated kinetic parameters data, generated from the NIST REFPROP database [121] covering the relevant range of temperatures and pressures are used to generate a calibration surface as shown in Figure 6.13. A LITGS signal is modelled for each relevant combination of temperature and pressure using this data.

6.5 Summary

In this chapter, the ability to generate LITGS signals in NO in a pressurised chamber over a range of temperatures, pressures, and concentrations has been demonstrated. Temperature calibration measurements have been made which will apply to flame based measurements in the next chapter. The inherent accuracy and precision of the technique has been examined and the setup validated to provide confidence that flame-based measurements of sufficient accuracy and precision may be possible. The signal shape and decay rate has been used to derive pressure and

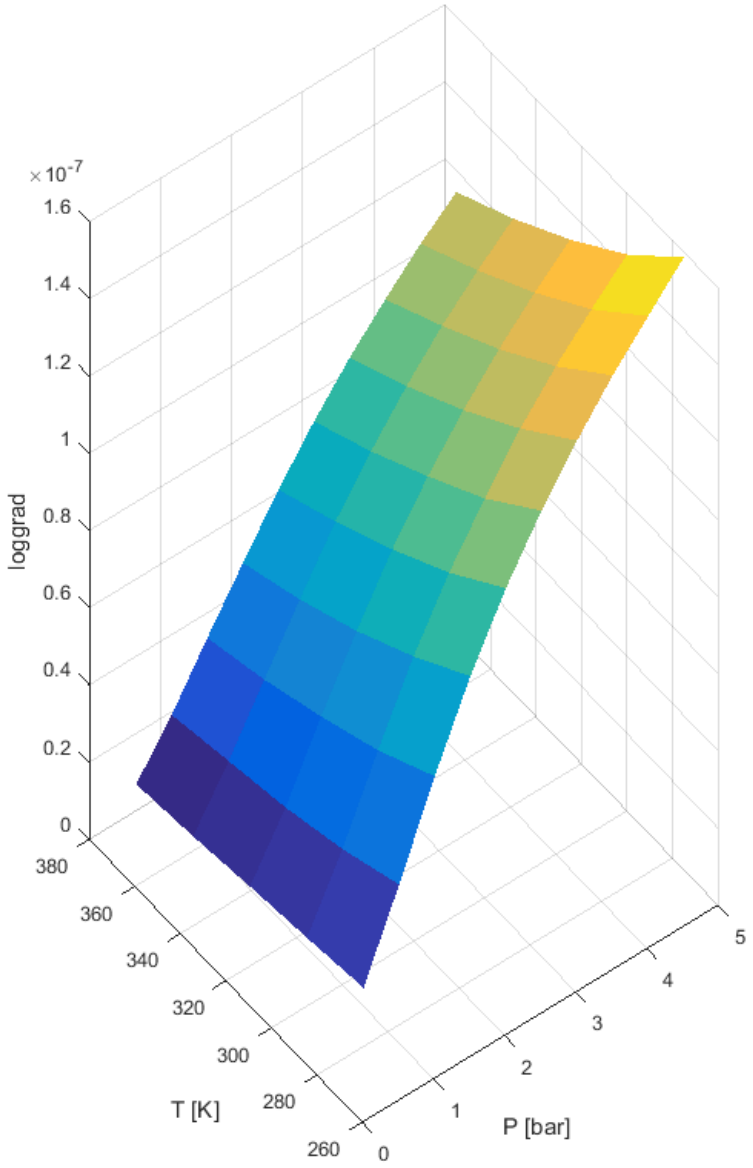


Figure 6.13: Surface plot of LITGS signal gradient values for a range of temperatures and pressures generated from known kinetic data and a LITGS theoretical model.

been shown to agree closely with pressures measures from a pressure gauge. The affects of concentration on signal have been examined. This work serves as the basis for flame-based temperature measurements as well as a proof of concept for pressure and concentration measurements in flame and engine conditions (see next chapter and [120, 122].

Chapter 7

LITGS in nitric oxide in a combusting flow

7.1 Introduction

The technique and experimental setup described in the previous chapter is extended here to a pressurised combustion environment. LITGS signals are produced in a premixed $CH_4/O_2/N_2$ flame which is operated over a range of pressures. Temperature measurements are made under a range of conditions and temperature accuracy and precision are discussed. The effects of NO concentration on the signal are discussed. Pressure measurements are again derived from LITGS signal shape as described in the previous chapter and compared with gauge pressure.

7.2 Flame temperature measurements

LITGS signals were generated over conditions designed to demonstrate the technique's ability over a range of temperatures, pressures and NO concentrations. Because the temperature of pre-mixed flames is strongly affected by oxygen content, the O_2 mole ratio was made to vary from 20% to 40% to produce a range of test temperatures. And because NO formation is highly temperature dependent, as discussed in Chapter 2, the variation in O_2 mass fraction results in a variation in NO concentration as well. The height of the interaction region above the burner (HAB) was made to vary such that measurements were taken in different parts of the flame. The pressure was made to vary from 1-2.5 bar to test the ability to measure temperature over a range of pressures.

7.2.1 Measurement error

As with last chapter, accuracy depends on certainty in the values of Λ and γ/m. Λ was calibrated in the same way as described in the previous chapter and with the same associated uncertainty. Uncertainty in γ/m arises from uncertainty in the burnt gas composition in the flame. The flame composition, and thus γ/m, was derived from flame equilibrium models in the literature. Specifically, the concentrations of the various species present in a $CH_4/O_2/N_2$ flame were based on a chemical equilibrium calculation as a function of temperature using the NASA-CEA simulation of Gordon and McBride [123]. This composition was used to calculate a weighted mean value of m and γ for an adiabatic flame temperature and this value was used to derive the flame temperature from the measured value of the

oscillation frequency for the LITGS signal in the flame. It was found that the difference in γ/m over the range covering the adiabatic flame temperature and the values derived from the LITGS measurements was insignificant relative to other experimental uncertainties. Consequently, the value of γ/m for adiabatic flames was used in the derivation of temperature in all subsequent measurements.*

Since the flame being investigated in this case was a stable laminar flow it is more appropriate to use averaged data over many single shots to arrive at a more meaningful estimate of the experimental uncertainty as more accurate and precise values are obtained by using averages over many shots to improve the signal-to-noise ratio. Figure 7.1 illustrates LITGS measurements recorded at 2 mm HAB in a stoichiometric flame at pressures of (a) 1 bar and (b) 2.5 bar, with an O_2:N_2 mass ratio of 25:75. The signals shown are averaged over 50 shots and the derived temperatures are obtained from the temperature corresponding to the best-fit model to the averaged signal.

In the case of the measurement at 1 bar, figure 7.1 (a), the error of $\pm$42 K on the value 2277 K consists of an uncertainty in the value of Λ of $\pm$10 K and an error in γ/m of $\pm$20 K associated with uncertainty in the mass flow measurements determining the gas composition. The remaining contribution to the error arises from the "goodness of fit" to the average of data, derived from the confidence interval of the fit parameter τ and having a value of $\pm$20 K.†

Figure 7.1 (b) shows measurements taken at 2.5 bar. Here the uncertainty in Λ

*In turbulent flames, where there are more unknowns and assumptions of a kinetic equilibrium model are less likely to hold, this source of error will become more significant. Here, however, a range of uncertainties could be assumed and the minimum and maximum error bounds estimated in a manner similar to that used by Williams et al [80].

†note that error in Λ and γ/m was added together in quadrature as these sources of error are independent, while the "goodness of fit" error was added directly.

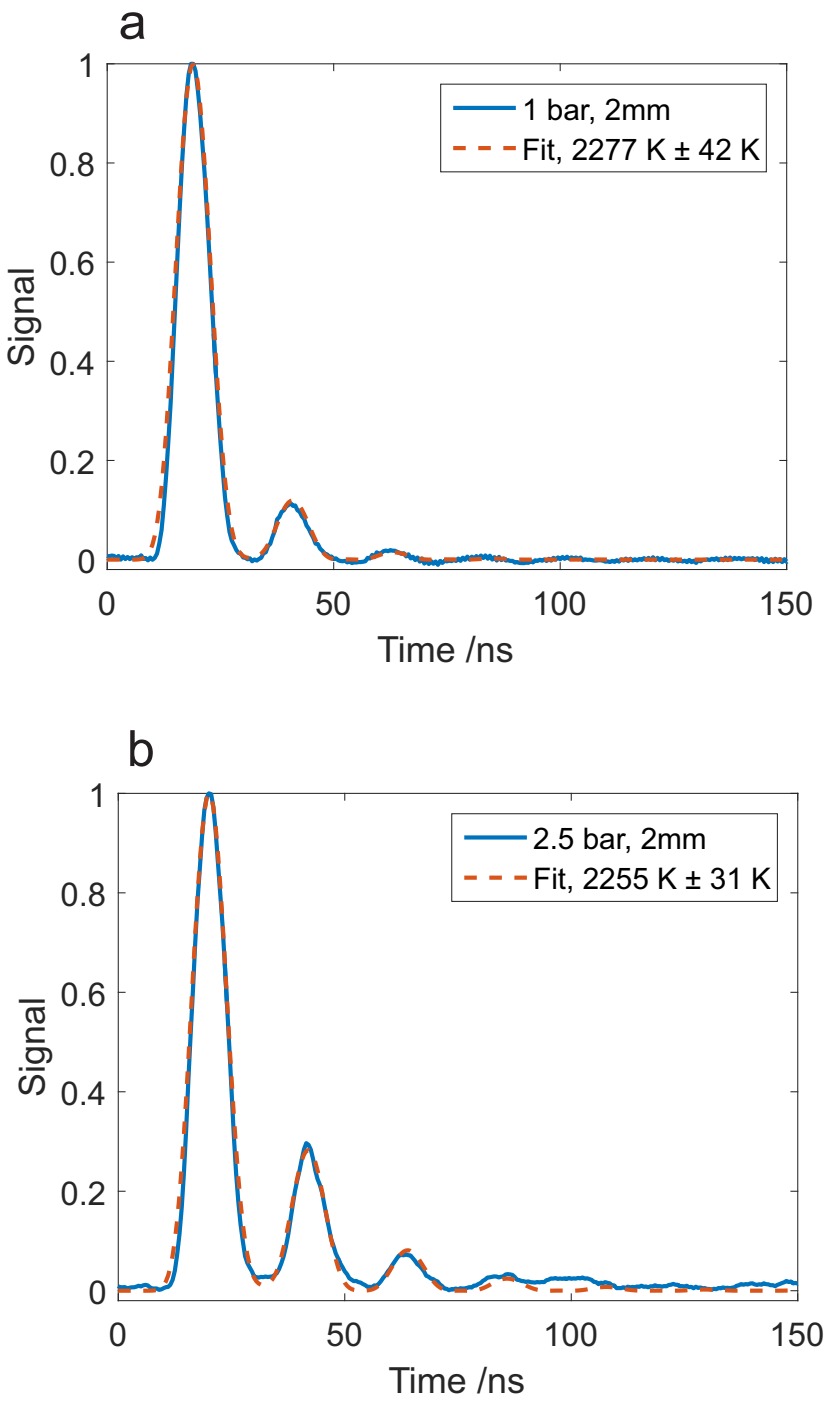


Figure 7.1: LITGS signals (average of 50 single shots) from flame at 2 mm HAB and (a) 1 bar and (b) 2.5 bar . The red curve shows the fitted simulated LITGS signal with temperature derived from the best fit to the data. The error reflects the confidence interval of the fitted temperature, as well as the uncertainty in Λ and γ/m.

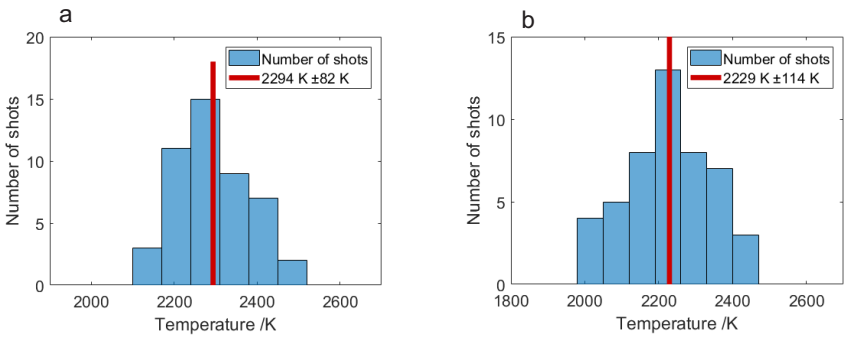


Figure 7.2: Histograms of fitted temperatures to 50 single shot signals at (a) 1 bar and (b) 2.5 bar. The red line represents the mean value and the error shows the standard deviation of the fitted temperatures.

and γ/m is the same but the goodness of fit error is reduced due to the presence of additional oscillations. The goodness of fit error was determined to be ± 9 K and the total error was estimated to be ± 31 K, an experimental uncertainty of $\pm 1.4\%$. The increase in uncertainty as compared with the optical cell data presented in the last chapter is most likely due to the presence of fluctuations in the temperature arising from flame flicker that are not present in the cell data.

The histograms in Figure 7.2 again, as described in chapter 6, give an indication of the variation in temperatures derived from single shots. A temperature was derived from the best-fit model corresponding to each individual shot and the standard deviations determined from batches of single shots. In the case of the flame at 1 bar the standard deviation in the single shot measurements was ± 82 K. In the 2.5 bar case the standard deviation was ± 114 K.

The slight reduction in temperature at 2.5 bar compared to that at 1 bar is explained by the reduced height of the flame at higher pressure. This results in the measurement region being further from the flame front which sits closer to the burner with consequent increase in heat loss to the burner surface. The higher value

Table 7.1: Gas flow rates and ratios used in methane flame

O_2/N_2 **ratio**	CH_4 **(ml/min)**	O_2 **(l/min)**	N_2 **(l/min)**	**Total (l/min)**
20/80	150	0.3	1.02	1.47
25/75	200	0.4	1.2	1.8
30/70	250	0.5	1.17	1.92
35/65	300	0.6	1.11	2
40/60	350	0.7	1.05	2.1

for the standard deviation at higher pressure, where signal strength and number of oscillations is increased, is also explained by a higher temperature gradient and the effect of flame flicker.

Measurements under varying conditions

Figure 7.3 shows the results of signals produced with a gas mixture with an O_2 mass ratio of 25%. The temperature was measured as a function of height above burner (HAB), at 1 bar and 2.5 bar. Typical signals, averaged over 100 single shots, are shown for two positions, 2 mm and 5 mm HAB. At the flame temperatures and across the relatively low range of pressures, the signals typically show only about 2 or 3 cycles of the acoustic oscillations. The experimental data is shown as the blue line and the model fit as the red line. These data illustrate the effect of hot, low density media compared to cooler higher density media by the increase in the number of observable oscillations in the signals in going from a temperature of 2294 K at 2mm HAB and 1 bar to 1693 K at 5 mm HAB and 2.5 bar.

Figure 7.4 shows temperatures derived from LITGS measurements at 2 mm HAB

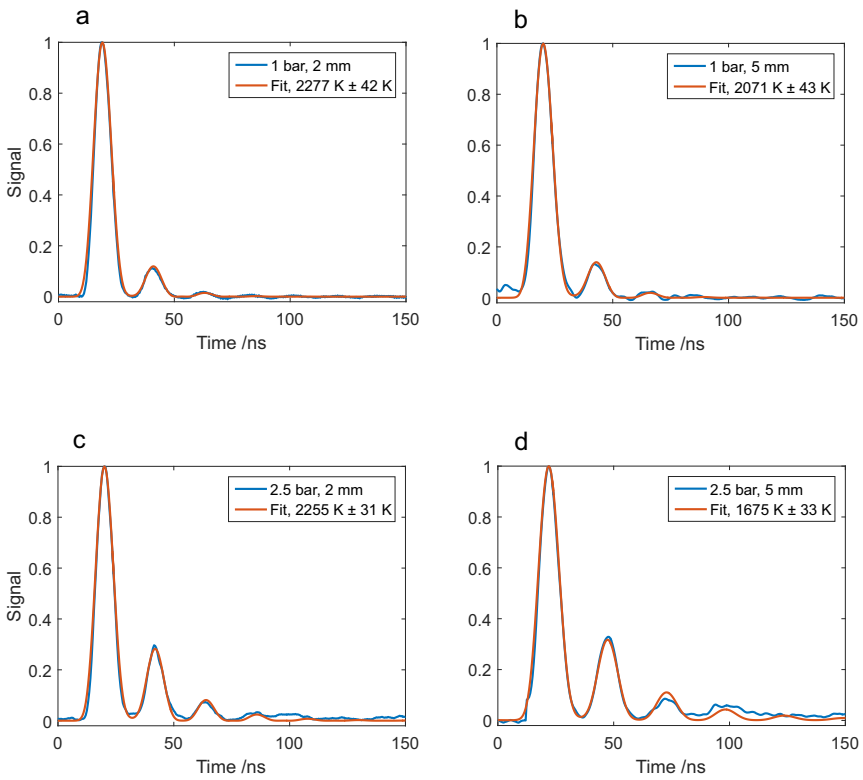


Figure 7.3: LITGS signals from flame at (a) 2 mm HAB and (b) 5 mm HAB at 1 bar total pressure and at (c) 2 mm HAB and (d) 5 mm HAB at 2.5 bar total pressure.

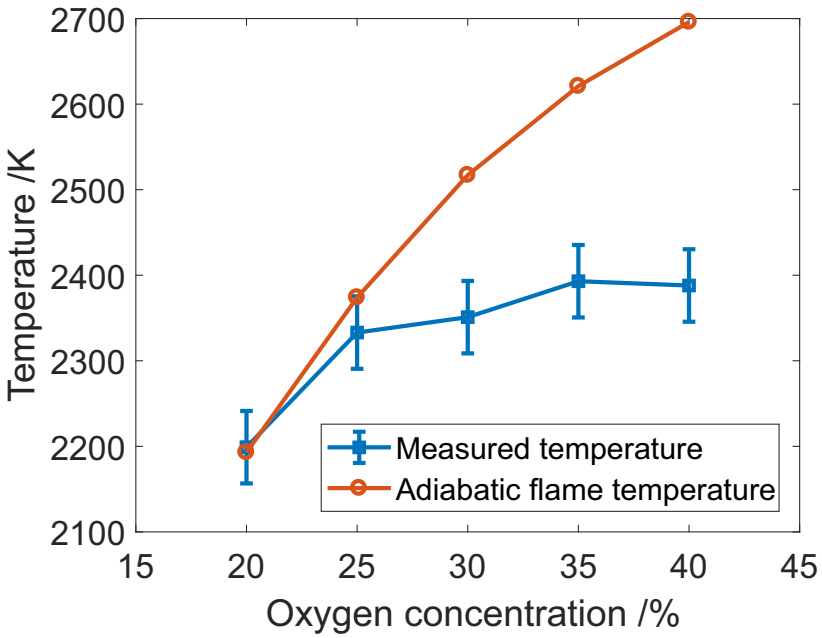


Figure 7.4: Flame temperature at 2 mm HAB as a function of oxygen content. The error bars indicate the total uncertainty based on the "goodness of fit" to averaged signals from 50 single shots and uncertainties in γ/m and Λ.

for differing O_2:N_2 ratios in stoichiometric flames as listed in Table 7.1. Temperature values are plotted as a function of O_2 concentration and the calculated adiabatic flame temperature for these gas mixtures is shown as well. The deviation from the adiabatic temperature is likely due largely to heat loss to the burner surface. This heat loss is increased at higher pressures as the flame is compressed and sits closer to the surface and the measurement region is therefore further away from the flame front.

Figure 7.5 shows temperature plotted with increasing HAB for the two conditions of 1 bar and 2.5 bar total pressure and having an O_2:N_2 molar ratio of 25:75. Temperature is shown to decrease with increasing HAB as the interaction region of the pump and probe beams is moved away from the flame front. Again, the high pressure case shows a more rapid decrease in temperatures with increasing HAB, likely due to the flame sitting closer to the burner in this case and therefore further from the interaction region and closer to the heat sink of the burner itself.

7.2.2 NO concentration effects on signal

The concentration of NO for different O_2 content in the gas mixture was calculated to be in the range 2000 to 5000 ppm and the LITGS signal strength, S, plotted as a function of the calculated concentration, N_{NO}. The result is shown in Figure 7.6 (a) and indicates that, as expected from the theory, S is proportional to N_{NO}^2. The technique therefore appears to scale favourably for high pressure measurements in the product gases of engines and gas turbines. In the case of engines, where peak pressures can reach $50 - 100$ bar, this means that temperature measurements using NO concentrations of up to 1000 ppm are feasible with probe volumes of the order

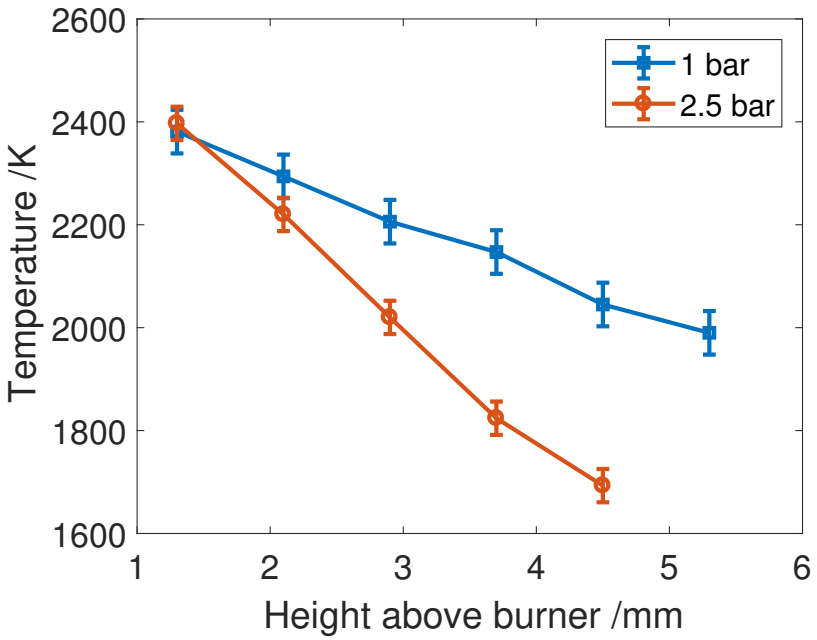


Figure 7.5: Temperatures at different HAB for flame pressures of 1 bar and 2.5 bar with 25 : 75 O_2:N_2 content in the premixed methane air flame. Error bars are based on the "goodness of fit" uncertainty and uncertainties in γ/m and Λ.

of cubic millimetres. The error bars indicate the standard deviation of single-shot values. With a typical noise level of 10 mV on the single-shot signals extrapolation to a $S/N = 1$ gives an estimate of the minimum detection limit of 125 ppm for single shot measurements. However, using averages over 50 single shots gives a lower noise level resulting in a minimum detection limit for a 5-second average measurement (10 Hz repetition rate of the laser) of 80 ppm, as shown in figure 7.6 (b).

As described in the previous chapter, the signal dependence on species number density means that concentration information could be extracted if other variables which affect signal can be accounted for or calibrated. A similar method as described in the previous chapter could be applied. In this case, a calibration measurement could be made using a kinetic model to estimate NO formation under controlled conditions and the LITGS tool could then be applied in more complicated combustion environments such as turbulent flames and gas turbine combustors. Doing so would require quite complicated models and calculations, similar to that done for other techniques, such as Polarisation spectroscopy [124, 125].

7.2.3 Flame barometry

The technique for estimating pressure from signal shape described in chapter 6 was applied here to the flame signals. It was applied also to signals taken in a Jaguar AJ133 5.0 L V8 optical engine [120].

A 25:75 ratio of O_2 to N_2 was used in this case and the pressure was made to vary from 1 bar to 2.5 bar on 0.5 bar increments. 100 single shots were averaged and

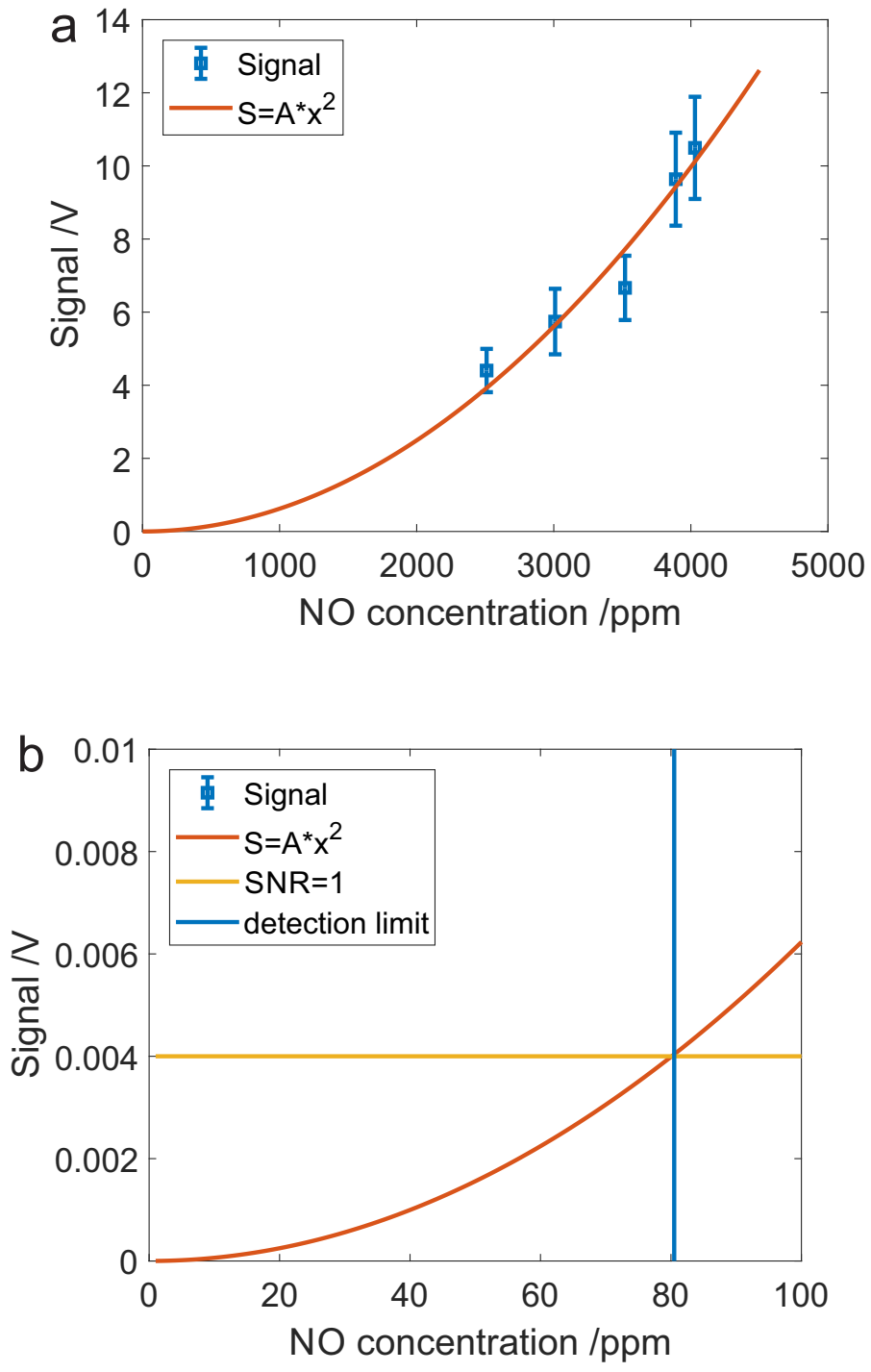


Figure 7.6: (a) Peak LITGS signal vs. simulated concentration of NO in the flames with different O_2 concentrations. The points follow a $S = Ax^2$ curve. (b) Extrapolation of the fitted curve down to the point where the signal to noise ratio is 1, and the resulting detection limit.

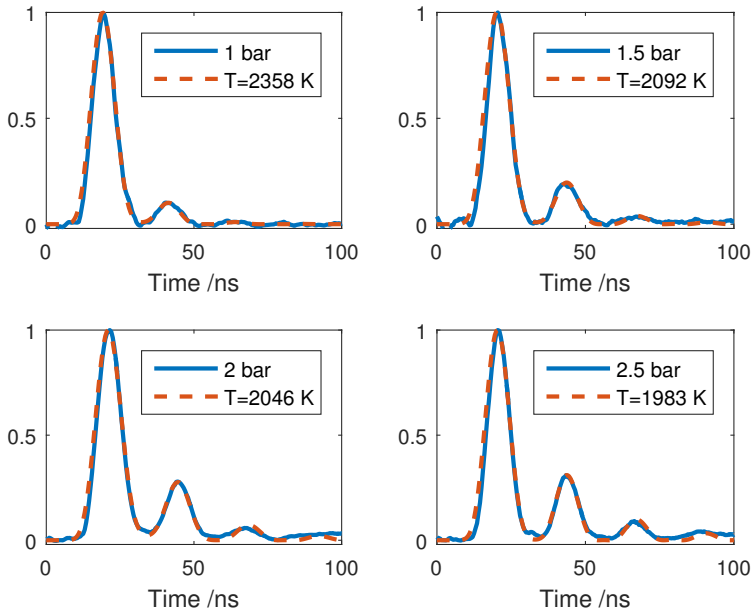


Figure 7.7: LITGS signals fitted using model of Paul et al to derive pressure

the resulting signals were fitted with the LITGS model. Figure 7.7 shows signals fitted with the model from Paul et al described earlier along with temperatures calculated from the oscillation frequency. Figure 7.8 shows the Reynolds number from the fitted LITGS signals at each pressure in the flame (left-hand side) and the derived pressure versus measured pressure with a pressure gauge (right-hand side).

In contrast to the chamber and engine data, a good fit was not achieved from the flame data. This is likely due to the very short life of the signal which means that quenching effects from the early part of the signal are more prominent and due to the fact that reliable viscosity values are harder to obtain at flame temperatures.

The viscosity, and thus the Reynolds number from which pressure is derived, is strongly dependent on both temperature and gas composition. The NIST REFPROP database [121], from which viscosity vales were obtained, does not

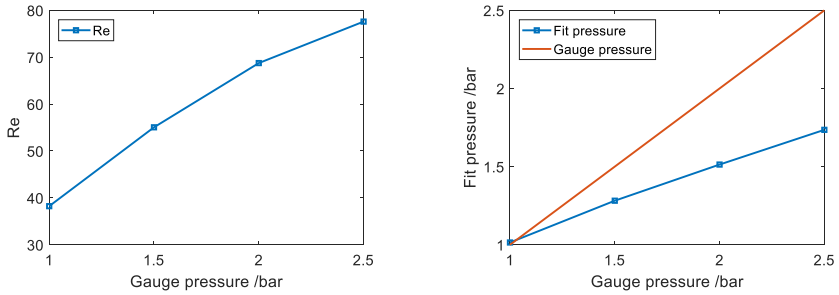


Figure 7.8: Derived Re number from 100 averaged LITGS signals at pressures from 1 to 2.5 bar. Derived pressures from LITGS signals compared with gauge pressure

produce reliable values at flame temperatures and cannot calculate viscosity for mixtures containing high concentrations of water vapour. Pressure estimates could likely be greatly improved with improved values for μ at flame temperatures.

The fact that these relatively low pressure and high temperature signals are very short-lived and with few oscillations means extracting an accurate Reynolds number is difficult. It may, however, be possible to obtain more accurate pressure measurements in high pressure flames which exhibit longer-lived signals (see for example [95] which would be the case in gas turbine combustors which operate at very high pressure.

7.3 Summary

Measurements of temperature have been demonstrated using LITGS signals in NO in a stable, laminar, pre-mixed CH_4 / O_2 / N_2 flame at moderate pressures around 1 bar. A relatively high degree of accuracy and precision was obtained versus traditional probe-based and alternative optical measuring techniques. As in

previous studies, it is found that the precision improves with increasing pressure. The variation of flame temperature with oxygen content and position in the flame has been measured with good precision sufficient to detect fluctuations arising from flame flicker or other external perturbations.

Temperature measurements have been shown to be possible over a range of pressures and locations in the flame. Although a relatively large probe volume has been used in the present experiments at low pressures, the dependence of the signal on the square of the density suggests that good signals could be produced with a smaller probe volume, and thus better spatial resolution, in high pressure flames typical of combustors and engines.

Measurements were taken over a range of concentrations and a detection limit of 80 ppm was achieved for average signals, sufficient for many combustion environments of interest. This value could likely be reduced further with more work to reduce noise and by working at higher pressure. A way forward was also indicated for how NO concentration measurements could be made from LITGS signals in future studies.

Pressure measurements using LITGS signals have been less successful at flame temperatures in this experimental setup than was found in the ambient temperature pressurised cell and in an optical engine. However the technique is validated and can be readily improved for better performance in flames by operating at higher pressures which would result in longer-lasting signals which in turn would enable more accurate fits and Reynolds number estimates.

Chapter 8

Conclusions and future work

8.1 Summary and conclusions

This chapter summarises the achievements of this work with combined DFWM and LITGS techniques and LITGS temperature, pressure and concentration studies in NO in a methane flame and describes the future direction of the work.

8.1.1 Simultaneous DFWM and LITGS

This work has investigated the use of simultaneous DFWM and LITGS signal generation for measurements in flames. The relative contribution of DFWM effects and LITGS effects have been illustrated by the time behaviour and shape change of the signals showing the transition from signals dominated by the coherent, population gratings at low pressures to those dominated by thermal gratings at higher pressures under unsaturated and saturated pump conditions. These results confirm and elaborate previous studies made using a variable-delay, pulsed probe

to record the signals [74]. It has been shown that under suitable conditions it is possible to isolate each contribution and thus, in principle, to use DFWM to monitor NO concentration and LITGS to obtain accurate and precise values of temperature in the same region of interest. Increasing pump laser energy would enable use of the combined techniques at higher pressure by continuing to saturate the NO transition as pressure increases and thus retain a pure DFWM signal. Modelling may also be possible to distinguish the relative contribution of each process.

8.1.2 Temperature, pressure and concentration measurements in NO

It has been demonstrated in this work that accurate and precise measurements of temperature can be made using LITGS signals from NO in stable, laminar, pre-mixed $CH_4/O_2/N_2$ flames at moderate pressures around 1 bar. As in previous studies, it is found that the precision improves with increasing pressure. The variation of flame temperature with oxygen content and position in the flame has been measured with good precision sufficient to detect fluctuations arising from flame flicker or other external perturbations. Although a relatively large probe volume has been used in the present experiments at low pressures, the dependence of the signal on the square of the density suggests that at higher pressures, typical of gas turbine combustors, a finer spatial resolution would be possible.

8.2 Future work

Building upon the achievements of this work and the experimental setup, a number of clear next steps will enable advancement toward a deeper understand of the technique and practical use for applications within gas turbine combustion environments. These include further improvement in temperature calibration and error reduction, particularly in single-shot measurements, working at higher pressures and under more realistic flame conditions, and other further advancements toward a practical device for use within high pressure turbulent environments of gas turbine combustors.

8.2.1 Temperature calibration and further error reduction

Current work is on-going to utilise the existing experimental setup and further explore temperature precision and accuracy in a National Physical Laboratory (NPL) standardised flame [126]. This is a pre-mixed propane-air flame in a portable system based on the Hencken flat flame burner design and with a well characterised temperature field above the burner. Temperatures measurements at ambient conditions will further enable us to test our setup and temperature measurements in known conditions and provide a traceable standard for measurements in flames or at flame temperatures.

Further work at higher pressures, which more closely mirror the conditions within a gas turbine should also be done. These would likely show longer lasting signals that would result in reduced error in average temperature measurements and improved ability to produce precise single-shot measurements.

8.2.2 High repetition rate measurements

Extending the work to a high repetition rate pump laser system would enable higher temporal resolution in single-shot measurements. The current work was done with a 10 Hz repetition rate. KHz or even MHz repetition rate lasers would enable further time-scale resolution between shots.

Initial work has been initiated in this direction. Förster et al made measurements in NO_2 at 10 kHz repetition rate in a cell at 1 kHz in a seeded flow subject to rapid compression with a measurement precision of 1.4% [100]. Separately, A non-uniform flow field has been seeded with biacetyl. The third harmonic (355 nm) of a Nd:YAG laser has been used to form the LITGS grating, operating at a repetition rate of 1 KHz and temperature and, separately, composition measurements have been made.

8.2.3 Multipoint measurements

Multi-point measurements using LITGS have been demonstrated by Willman and Ewart in a toluene-seeded flow [98]. This could be extended to the present work to extend point temperature measurements and enhance the usefulness of a potential future device to provide temperature profiles within gas turbine combustors or model turbulent combustion environments.

8.2.4 Pressure and concentration measurement

The work presented in the present thesis to capture pressure information along with temperature information from LITGS signals should be further developed. The technique should be explored at higher pressure with NO in flames which will result

in longer lasting signals to validate the technique's ability in high temperature flames.

Software, based on the work done with the full LITGS model and fast processing method described in chapter 6 should be made ready for use by other research or commercial groups to complement temperature measurements and thereby provide real-time simultaneous pressure and temperature measurements.

The ability to extract useful concentration information from signal strength data could also be further advanced. A carefully controlled setup would be required to isolate the effects of target molecule number density on signal strength from other factors and calibration demonstrated where the technique is used under more well known concentration conditions (i.e, optical cell or laminar flame) and then applied in a less controlled environment (ie a NO flow or turbulent flame). Alternatively, as shown in chapter 5, further work using DFWM simultaneously with cw LITGS could be done using higher energy in order to produce saturating pump beams at higher pressures and thus retain a pure DFWM signal for use in deriving concentration. More detailed modelling of the combined DFWM and LITGS effect could also be done to assist in deriving concentration information from the DFWM component.

Bibliography

[1] U.S. Energy Information Organization. *EIA - International Energy Outlook 2017*. Tech. rep. U.S. Energy Information Adminisitration (eia), 2017, p. 9.

[2] Forecast International. *The Market for Gas Turbine Electrical Power Generation*. Tech. rep. 2014.

[3] A. C. Eckbreth. *Laser Diagnostics For Combustion Temperatures And Species*. Second Edi. Gordon and Breach, 1996.

[4] K. Kohse-Höinghaus and J. Jefferies. *Applied Combustion Diagnostics*. 1st Ed. London: Taylor & Francis, 2002.

[5] M. V. Heitor and J. H. Whitelaw. 'Velocity, temperature, and species characteristics of the flow in a gas-turbine combustor'. *Combustion and Flame* 64.1 (1986), pp. 1–32. DOI: 10.1016/0010-2180(86)90095-7.

[6] N. Docquier and S. Candel. 'Combustion control and sensors: A review'. *Progress in Energy and Combustion Science* 28.2 (2002), pp. 107–150. DOI: 10.1016/S0360-1285(01)00009-0.

[7] T. C. Williams, R. W. Schefer, J. C. Oefelein and C. R. Shaddix. 'Idealized gas turbine combustor for performance research and validation of large eddy

simulations'. *Review of Scientific Instruments* 78.3 (2007). DOI: 10.1063/1.2712936.

[8] F. E. Marble and S. M. Candel. 'Acoustic disturbance from gas non-uniformities convected through a nozzle'. *Journal of Sound and Vibration* 55.2 (1977), pp. 225–243. DOI: 10.1016/0022-460X(77)90596-X.

[9] W. Polifke, C. O. Paschereit and K. Paschereit. 'Constructive and Destructive Interference of Acoustic and Entropy Waves in a Premixed Combustor with a Choked Exit'. *The International Journal of Acoustics and Vibration* 6.3 (2001), p. 85747. DOI: 10.20855/ijav.2001.6.382.

[10] A. S. Morgans and I. Duran. 'Entropy noise: A review of theory, progress and challenges'. *International Journal of Spray and Combustion Dynamics* 8.4 (2016), pp. 285–298. DOI: 10.1177/1756827716651791.

[11] J. L. Kerrebrock. *Aircraft Engines and Gas Turbines*. Second Edi. MIT Press, 1992.

[12] L. Rayleigh. 'The Theory of Sound'. *On the instability of jets* 10 (1878), pp. 4–13.

[13] E. P. A. (EPA). *EPA Federal Register 38, Statute 106*. 1973.

[14] F. E. C. Culick. *Unsteady Motions in Combustion Chambers for Propulsion Systems*. Vol. 323. December. 2006, pp. 1–664.

[15] A. Dowling and S. Stow. 'Acoustic Analysis of Gas Turbine Combustors'. *Journal of Propulsion and Power* 19.5 (2003), pp. 751–764.

[16] F. De Domenico, E. O. Rolland and S. Hochgreb. 'Detection of direct and indirect noise generated by synthetic hot spots in a duct'. *Journal of Sound and Vibration* 394 (2017), pp. 220–236. DOI: 10.1016/j.jsv.2017.01.004.

[17] P. Weigand, W. Meier, X. Duan and M. Aigner. 'Laser-Based Investigations of Thermoacoustic Instabilities in a Lean Premixed Gas Turbine Model Combustor'. *Journal of Engineering for Gas Turbines and Power* 129.July 2007 (2007), p. 664. DOI: 10.1115/1.2718224.

[18] A. Ehn, J. Zhu, X. Li and J. Kiefer. 'Advanced Laser-Based Techniques for Gas-Phase Diagnostics in Combustion and Aerospace Engineering'. *Applied Spectroscopy* 71.3 (2017), pp. 341–366. DOI: 10.1177/0003702817690161.

[19] J. Kiefer and A. L. Cromwell. 'Analysis of single malt Scotch whisky using Raman spectroscopy'. *Anal. Methods* 9.3 (2017), pp. 511–518. DOI: 10.1039/C6AY02907H.

[20] C. Schulz, A. Dreizler, V. Ebert and J. Wolfrum. 'Combustion Diagnostics'. In: *Springer Handbook of Experimental Fluid Mechanic*. Ed. by C. Tropea, A. Yarin and J. Foss. Springer Berlin Heidelberg, 2007, pp. 1241–1315.

[21] R. W. Boyd. *Nonlinear Optics*. 3rd editio. Academic Press, Inc., 1992.

[22] J. Kiefer and P. Ewart. 'Laser diagnostics and minor species detection in combustion using resonant four-wave mixing'. *Progress in Energy and Combustion Science* 37.5 (2011), pp. 525–564. DOI: 10.1016/j.pecs.2010.11.001.

[23] P. Maker and R. Terhune. 'Study of Optical Effects Due to an Induced Polarization Third Oder in the Electric Field Strength'. *PHysical Review* 137 (3A) (1965), pp. 801–818.

[24] S. Roy, J. R. Gord and A. K. Patnaik. 'Recent advances in coherent anti-Stokes Raman scattering spectroscopy: Fundamental developments and applications in reacting flows'. *Progress in Energy and Combustion Science* 36.2 (2010), pp. 280–306. DOI: 10.1016/j.pecs.2009.11.001.

[25] J. a. Shirley, R. J. Hall and a. C. Eckbreth. 'Folded BOXCARS for rotational Raman studies.' *Optics letters* 5.9 (1980), p. 380. DOI: 10.1364/OL.5.000380.

[26] S. A. J. Druet, B. Attal, T. K. Gustafson and J. P. Taran. 'Electronic resonance enhancement of coherent anti-Stokes Raman scattering'. *Physical Review A* 18.4 (1978), pp. 1529–1557. DOI: 10.1103/PhysRevA.18.1529.

[27] B. Attal-Tretout, P. Berlemont and J. Taran. 'Three-colour CARS spectroscopy of the OH radical at triple resonance'. *Mol. Phys.* 70.1 (1990).

[28] J. P. Kuehner, S. V. Naik, W. D. Kulatilaka, N. Chai, N. M. Laurendeau, R. P. Lucht, M. O. Scully, S. Roy, A. K. Patnaik and J. R. Gord. 'Perturbative theory and modeling of electronic-resonance-enhanced coherent anti-Stokes Raman scattering spectroscopy of nitric oxide'. *The Journal of Chemical Physics* 128.17 (2008), p. 174308. DOI: 10.1063/1.2909554.

[29] W. D. Kulatilaka, N. Chai, S. V. Naik, N. M. Laurendeau, R. P. Lucht, J. P. Kuehner, S. Roy and J. R. Gord. 'Measurement of nitric oxide concentrations in flames by using electronic-resonance-enhanced coherent anti-

Stokes Raman scattering'. *Optics Letters* 31.22 (2006), pp. 3357–3359. DOI: Doi10.1364/Ol.31.003357.

[30] J. Jonuscheit, A. Thumann, M. Schenk, T. Seeger and A. Leipertz. 'One-dimensional vibrational coherent anti-Stokes Raman-scattering thermometry'. *Optics Letters* 21.19 (1996), pp. 1532–1534. DOI: Doi10.1364/Ol.21.001532.

[31] A. Bohlin and C. J. Kliewer. 'Single-shot hyperspectral coherent Raman planar imaging in the range 0-4200 cm-1'. *Applied Physics Letters* 105.16 (2014), pp. –5. DOI: 10.1063/1.4900477.

[32] A. Bohlin and C. J. Kliewer. 'Diagnostic imaging in flames with instantaneous planar coherent Raman spectroscopy'. *Journal of Physical Chemistry Letters* 5.7 (2014), pp. 1243–1248. DOI: 10.1021/jz500384y.

[33] A. Bohlin, B. D. Patterson and C. J. Kliewer. 'Communication: Simplified two-beam rotational CARS signal generation demonstrated in 1D'. *Journal of Chemical Physics* 138.8 (2013), pp. –4. DOI: 10.1063/1.4793556.

[34] A. Bohlin and C. J. Kliewer. 'Communication: Two-dimensional gas-phase coherent anti-Stokes Raman spectroscopy (2D-CARS): Simultaneous planar imaging and multiplex spectroscopy in a single laser shot'. *Journal of Chemical Physics* 138.22 (2013). DOI: 10.1063/1.4810876.

[35] J. R. Gord, T. R. Meyer and S. Roy. 'Applications of ultrafast lasers for optical measurements in combusting flows.' *Annual review of analytical chemistry (Palo Alto, Calif.)* 1 (2008), pp. 663–87. DOI: 10.1146/annurev.anchem.1.031207.112957.

[36] S. F. Hanna, W. D. Kulatilaka, Z. Arp, T. Opatrný, M. O. Scully, J. P. Kuehner and R. P. Lucht. 'Electronic-resonance-enhanced coherent anti-Stokes Raman spectroscopy of nitric oxide'. *Applied Physics Letters* 83.9 (2003), pp. 1887–1889. DOI: 10.1063/1.1604947.

[37] R. Palmer. *The CARSFT computer code for calculating coherent anti-Stokes Raman spectra*. 1989.

[38] T. Dreier, B. Lange, J. Wolfrum and M. Zahn. 'Determination of temperature and concentration of molecular nitrogen, oxygen and methane with coherent anti-stokes raman scattering'. *Applied Physics B Photophysics and Laser Chemistry* 45.3 (1988), pp. 183–190. DOI: 10.1007/BF00695289.

[39] T. Seeger and A. Leipertz. 'Experimental comparison of single-shot broadband vibrational and dual-broadband pure rotational coherent anti-Stokes Raman scattering in hot air'. *Applied Optics* 35.15 (1996), pp. 2665–2671.

[40] P. Snowdon, S. Skippon and P. Ewart. 'Improved precision of single-shot temperature measurements by broadband CARS by use of a modeless laser'. *Applied Optics* 30.9 (1991), pp. 1008–1010.

[41] P. E. Bengtsson, L. Martinsson, M. Aldén, B. Johansson, B. Lassesson, K. Marforio and G. Lundholm. 'Dual-broadband rotational cars measurements in an IC engine'. *Symposium (International) on Combustion* 25.1 (1994), pp. 1735–1742. DOI: 10.1016/S0082-0784(06)80822-2.

[42] C. Brackmann, J. Bood, M. Afzelius and P.-E. Bengtsson. 'Thermometry in internal combustion engines via dual-broadband rotational coherent anti-

Stokes Raman spectroscopy'. *Measurement Science and Technology* 15.3 (2004), R13–R25. DOI: 10.1088/0957-0233/15/3/R01.

[43] A. Eckbreth. 'Laser Diagnostics for Gas Turbine Thermometry and Species Measurements'. In: *Instrumentation for Combustion and Flow in Engines*. Ed. by J. Whitelaw and P. Witze. Springer, Dordrecht, 1989.

[44] C. Wieman and T. Hänsch. 'Doppler-free laser polarization spectroscopy'. *Physical Review Letters* 36.20 (1976), pp. 1170–1173.

[45] K. Nyholm, R. Maier, C. Aminoff and M. Kaivola. 'Detection of OH in flames by using polarisation spectroscopy'. *Applied optics* 32 (1993), pp. 919–924.

[46] M. New, P. Ewart, A. Dreizler and T. Dreier. 'Multiplex Polarization Spectroscopy of OH for Flame Thermometry'. *Applied Physics B* 65 (1997), pp. 633–637.

[47] K. Nyholm, R. Fritzon and M. Alden. 'Single-pulse two-dimensional temperature imaging in flames by degenerate four-wave mixing and polarization spectroscopy'. *Applied Physics B* 59.1 (1994), pp. 37–43.

[48] B. Löfstedt, R. Fritzon and M. Alédn. 'Investigation of NO detection in flames by the use of polarization spectrosopy'. *Applied Optics* 35.12 (1996), pp. 2140–2146.

[49] R. L. Farrow and D. J. Rakestraw. 'Detection of Trace Molecular Species Using Degenerate Four-Wave Mixing'. *Science* 257.5078 (1992), pp. 1894–1900. DOI: 10.1126/science.257.5078.1894.

[50] P. Ewart and S. V. O'Leary. 'Detection of OH in a flame by degenerate four-wave mixing.' *Optics letters* 11.5 (1986), p. 279. DOI: 10.1364/OL.11.000279.

[51] T. Dreier and D. J. Rakestraw. 'Measurement of OH rotational remperatures in a flame using degenerate four-wave mixing'. 15.1 (1990), pp. 72–74.

[52] R. L. Abrams and R. C. Lind. 'Degenerate four-wave mixing in absorbing media.' *Optics letters* 2.4 (1978), p. 94. DOI: 10.1364/OL.2.000094.

[53] R. T. Bratfalean, G. M. Lloyd and P. Ewart. 'Degenerate four-wave mixing for arbitrary pump and probe intensities'. *Journal of the Optical Society of America B* 16.6 (1999), p. 952. DOI: 10.1364/JOSAB.16.000952.

[54] K. Nelson, D. Lutz, M. Fayer and L. Madison. 'Laser-induced phonon spectroscopy'. *Physical Review B* 24.6 (1981), pp. 3261–3275.

[55] W. Hubschmid, B. Hemmerling and a. Stampanoni-Panariello. 'Rayleigh and Brillouin modes in electrostrictive gratings'. *Journal of the Optical Society of America B* 12.10 (1995), p. 1850. DOI: 10.1364/JOSAB.12.001850.

[56] R. L. Abrams and R. C. Lind. 'Degenerate four-wave mixing in absorbing media: errata.' *Optics letters* 3.5 (1978), p. 205. DOI: 10.1364/OL.3.000205.

[57] T. A. Reichardt, R. P. Lucht, P. M. Danehy and R. L. Farrow. 'Theoretical investigation of the forward phase-matched geometry for degenerate four-wave mixing spectroscopy'. *Journal of the Optical Society of America B* 15.10 (1998), p. 2566. DOI: 10.1364/JOSAB.15.002566.

[58] T. A. Reichardt and R. P. Lucht. 'Effect of Doppler broadening on quantitative concentration measurements with degenerate four-wave mixing spectroscopy'. *Journal of the Optical Society of America B (Optical Physics) Publ: Opt. Soc. America June* 13.6 (1996), pp. 1107–1119.

[59] P. M. Danehy, E. J. Friedman-Hill, R. P. Lucht and R. L. Farrow. 'The effects of collisional quenching on degenerate four-wave mixing'. *Applied Physics B Photophysics and Laser Chemistry* 57.4 (1993), pp. 243–248. DOI: 10.1007/BF00325202.

[60] T. A. Reichardt and R. P. Lucht. 'Interaction of closely spaced resonances in degenerate four-wave-mixing spectroscopy'. 14.10 (1997), pp. 2449–2458.

[61] G. M. Lloyd and P. Ewart. 'High resolution spectroscopy and spectral simulation of C2 using degenerate four-wave mixing'. *Journal of Chemical Physics* 110.1999 (1999), pp. 385–392. DOI: 10.1063/1.478070.

[62] K. Bultitude, R. Bratfalean and P. Ewart. 'Saturation effects in molecular spectroscopy using degenerate four-wave mixing'. *Journal of Raman Spectroscopy* 34.12 (2003), pp. 1030–1036. DOI: 10.1002/jrs.1100.

[63] G. Dieke and H. Crosswhite. 'The Ultraviolet Bands of OH'. *Journal of Quantitative Spectroscopy and Radiative Transfer* 2 (1961), pp. 97–199.

[64] A. Goldman and J. R. Gillis. 'Spectral line parameters for the A2Sigma-X2Pi/0,0/ band of OH for atmospheric and high temperatures'. 25.2 (1981). DOI: 10.1016/0022-4073(81)90004-2.

[65] G. Lloyd. 'Four Wave Mixing Techniques and Applications in Combustion Diagnostics'. PhD thesis. University of Oxford, 1997.

[66] D. Rakestraw, R. Farrow and T. Dreier. 'Two-dimensional imaging of OH in flames by degenerate four-wave mixing'. *Optics letters* 15.2 (1990), pp. 709–711.

[67] P. Ewart and M. Kaczmarke. 'Two-dimensional mapping of temperature in a flame by degenerate four-wave mixing in OH'. *Applied Optics* 30.27 (1991), pp. 3996–3999.

[68] B. Yip, P. Danehy and R. Hanson. 'Degenerate four-wave mixing temperature measurements in a flame'. *Optics letters* 17.10 (1992), pp. 751–753.

[69] P. Ewart, P. Snowdon and I. Mangusson. 'Two-dimensional phase-conjugate imaging of atomic distributions in flames by degenerate four-wave mixing'. *Optics letters* 14.11 (1989), pp. 563–565.

[70] R. Vander Wal, R. Farrow and D. Rakestraw. 'High-resolution investigation of degenerate four-wave mixing in the $\gamma(0,0)$ band of nitric oxide'. In: *Twenty-fourth symposium (international) on combustion*. Pittsburgh, PA, 1993, pp. 1653–1659.

[71] A. J. Grant, P. Ewart and C. R. Stone. 'Detection of NO in a spark-ignition research engine using degenerate four-wave mixing'. *Applied Physics B: Lasers and Optics* 74.1 (2002), pp. 105–110. DOI: 10.1007/s003400100740.

[72] R. Stevens, P. Ewart, H. Ma and C. R. Stone. 'Measurement of nitric oxide concentration in a spark-ignition engine using degenerate four-wave mixing'. *Combustion and Flame* 148 (2007), pp. 223–233. DOI: 10.1016/j.combustflame.2006.11.002.

[73] P. H. Paul, R. L. Farrow and P. M. Danehy. 'Gas-phase thermal-grating contributions to four-wave mixing'. *Journal of the Optical Society of America B* 12.3 (1995), p. 384. DOI: 10.1364/JOSAB.12.000384.

[74] P. Danehy, P. Paul and R. Farrow. 'Thermal-grating contributions to degenerate four-wave mixing in nitric oxide'. *Journal of the Optical Society of America B* 12.9 (1995), pp. 1564–1576.

[75] E. B. Cummings. 'Laser-induced thermal acoustics: simple accurate gas measurements.' *Optics letters* 19.17 (1994), pp. 1361–1363. DOI: 10.1364/OL.19.001361.

[76] H. Eichler, P. Günter and D. Pohl. *Laser-induced Dynamic Gratings*. Springer-Verlag, Berlin Heidelberg, 1986.

[77] F. Hansen. *Approximations for the thermodynamic and transport properties of high-temperature air*. Tech. rep. Moffett Field, CA: United States National Advisory Committee for Aeronautics. Ames Aeronatuical Lab, 1958. DOI: 19930084937.

[78] B. A. O. Williams. 'Quantitative Laser Diagnostics for Combustion'. *Thesis, University of Oxford* (2009).

[79] A. Stampanoni-Panariello, D. N. Kozlov, P. P. Radi and B. Hemmerling. 'Gas phase diagnostics by laser-induced gratings I. Theory'. *Applied Physics B: Lasers and Optics* 81.1 (2005), pp. 101–111. DOI: 10.1007/s00340-005-1852-z.

[80] B. Williams, M. Edwards, R. Stone, J. Williams and P. Ewart. 'High precision in-cylinder gas thermometry using Laser Induced Gratings: Quantitative measurement of evaporative cooling with gasoline/alcohol blends in a GDI optical engine.' *Combustion and Flame* 161.1 (2014), pp. 270–279. DOI: 10.1016/j.combustflame.2013.07.018.

[81] M. Edwards. 'The effect of uncertainty in omposition on laser-induced grating thermometry'. MPhil. University of Oxford, 2011.

[82] C. Willman. 'Laser Diagnostics for Spatially Resolved Thermometry in Combustion and Flows'. PhD thesis. University of Oxford, 2016.

[83] N. Wijeyasinghe. 'Laser-induced grating spectroscopy in non-uniform temperature fields and flames'. MPhil. University of Oxford, 2013.

[84] R. Stevens. 'Laser-Induced Grating Techniques for Combustion Diagnostics'. PhD thesis. University of Oxford, 2004.

[85] R. Stevens and P. Ewart. 'Single-shot measurement of temperature and pressure using laser-induced thermal gratings with a long probe pulse'. *Applied Physics B: Lasers and Optics* 78 (2004), pp. 111–117. DOI: 10.1007/s00340-003-1282-8.

[86] B. Hemmerling, D. N. Kozlov, O. M. Stel'makh and B. Attal-Trétout. 'Diagnostics of water-containing gas mixtures using thermal laser-induced gratings'. *Chemical Physics* 320.2-3 (2006), pp. 103–117. DOI: 10.1016/j.chemphys.2005.06.048.

[87] S. Williams, L. A. Rahn, P. H. Paul, J. W. Forsman and R. N. Zare. 'Laser-induced thermal grating effects in flames.' *Optics letters* 19.21 (1994), pp. 1681–1683. DOI: 10.1364/OL.19.001681.

[88] E. B. Cummings. 'Laser-induced thermal acoustics: simple accurate gas measurements.' *Optics letters* 19.17 (1994), pp. 1361–1363. DOI: 10.1364/OL.19.001361.

[89] E. Cummings, I. Leyva and H. Hornung. 'Laser-induced thermal acoustics (LITA) signals from finite beams'. *Applied Optics* 34.15 (1995), pp. 3290–3302.

[90] R. Stevens and P. Ewart. 'Simultaneous single-shot measurement of temperature and pressure along a one-dimensional line by use of laser-induced thermal grating spectroscopy.' *Optics letters* 31.8 (2006), pp. 1055–1057. DOI: 10.1364/OL.31.001055.

[91] S. Schlamp and T. Sobota. 'Measuring concentrations with laser-induced thermalization and electrostriction gratings'. *Experiments in Fluids* 32.6 (2002), pp. 683–688. DOI: 10.1007/s00348-002-0419-6.

[92] B. Hemmerling, W. Hubschmid and P. S. Institut. 'Temperature and mixture fraction measurements in gases by laser-induced electrostrictive gratings' (1998), pp. 69–75.

[93] B. Roshani, A. Flügel, I. Schmitz, D. N. Kozlov, T. Seeger, L. Zigan, J. Kiefer and A. Leipertz. 'Simultaneous measurements of fuel vapor concentration and temperature in a flash-boiling propane jet using laser-induced gratings'. *Journal of Raman Spectroscopy* 44.10 (2013), pp. 1356–1362. DOI: 10.1002/jrs.4315.

[94] D. J. Walker, R. B. Williams and P. Ewart. 'Thermal grating velocimetry.' *Optics letters* 23.16 (1998), pp. 1316–1318. DOI: 10.1364/OL.23.001316.

[95] H. Latzel, a. Dreizler, T. Dreier, J. Heinze, M. Dillmann, W. Stricker, G. Lloyd and P. Ewart. 'Thermal grating and broadband degenerate four-wave

mixing spectroscopy of OH in high-pressure flames'. *Applied Physics B: Lasers and Optics* 67 (1998), pp. 667–673. DOI: 10.1007/s003400050563.

[96] M. Brown and W. Roberts. 'Single-point thermometry in high-pressure, sooting, premixed combustion environments'. *Journal of Propulsion and Power* 15.1 (1999), pp. 119–127.

[97] T. Seeger, J. Kiefer, M. C. Weikl, A. Leipertz and D. N. Kozlov. 'Time-resolved measurement of the local equivalence ratio in a gaseous propane injection process using laser-induced gratings.' *Optics express* 14.26 (2006), pp. 12994–13000. DOI: 10.1364/OE.14.012994.

[98] C. Willman and P. Ewart. 'Multipoint temperature measurements in gas flows using 1-D laser-induced grating scattering'. *Experiments in Fluids* 57.191 (2016).

[99] A. Hell, F. Förster and B. Weigan. 'Validation of laser-induced thermal acoustics for chemically reacting H2/air free jets'. *Journal of Raman Spectroscopy* 47.9 (2016), pp. 1157–1166.

[100] F. J. Förster, C. Crua, M. Davy and P. Ewart. 'Time-resolved gas thermometry by laser-induced grating spectroscopy with a high-repetition rate laser system'. *Experiments in Fluids* 58.7 (2017), pp. 1–8. DOI: 10.1007/s00348-017-2370-6.

[101] A. L. Sahlberg, D. Hot, J. Kiefer, M. Aldén and Z. Li. 'Mid-infrared laser-induced thermal grating spectroscopy in flames'. *Proceedings of the Combustion Institute* 36.3 (2017), pp. 4515–4523. DOI: 10.1016/j.proci.2016.07.017.

[102] Z. W. Sun, Z. S. Li, B. Li, M. Aldén and P. Ewart. 'Detection of C2H2 and HCl using mid-infrared degenerate four-wave mixing with stable beam alignment: Towards practical in situ sensing of trace molecular species'. *Applied Physics B: Lasers and Optics* 98 (2010), pp. 593–600. DOI: 10.1007/s00340-009-3798-z.

[103] S. V. Polyakov. 'Photomultiplier Tubes'. *Experimental Methods in the Physical Sciences* 45 (2013), pp. 69–82. DOI: 10.1016/B978-0-12-387695-9.00003-2.

[104] P. Ewart. 'A modeless, variable bandwidth, tunable laser'. *Optics Communications* 55.2 (1985), pp. 124–126. DOI: 10.1016/0030-4018(85)90314-1.

[105] K. Richard, P. Manson and P. Ewart. 'A widely tunable, high power, single-mode laser for linear and nonlinear spectroscopy'. *Measurement Science and Technology* 19.1 (2008), p. 015603. DOI: 10.1088/0957-0233/19/1/015603.

[106] K. Bultitude, R. Stevens and P. Ewart. 'High-resolution degenerate four-wave-mixing spectroscopy of OH in a flame with a novel single-mode tunable laser'. *Applied Physics B: Lasers and Optics* 79.6 (2004), pp. 767–773. DOI: 10.1007/s00340-004-1641-0.

[107] M. New and P. Ewart. 'High Power Single Mode Radiation by Narrow-band Amplifiction of a Diode Laser'. *Optics Communications* 123 (1996), pp. 139–142.

[108] G. Lloyd, I. Hughes, R. Bratfalean and P. Ewart. 'Broadband Degenerate Four-Wave Mixing of OH for Flame Thermometry'. *Applied Physics B: Lasers and Optics* 67.1 (1998), pp. 107–113.

[109] K. L. Richard. 'Development of a Laser System for High Resolution Non-Linear Infrared Spectroscopy' (2007).

[110] K. Richard and P. Ewart. 'High-resolution infrared polarization spectroscopy and degenerate four wave mixing spectroscopy of methane'. *Applied Physics B: Lasers and Optics* 94.4 (2009), pp. 715–723. DOI: 10.1007/s00340-009-3363-9.

[111] W. G. Bessler, C. Schulz, V. Zick and J. W. Daily. 'A versatile modeling tool for nitric oxide LIF spectra'. *Proceedings of the Third Joint Meeting of the U.S. Sections of The Combustion Institute* December (2003), P105.

[112] P. R. Hammond. 'Laser dye DCM, its spectral properties, synthesis and comparison with other dyes in the red'. *Optics Communications* 29.3 (1979), pp. 331–333. DOI: 10.1016/0030-4018(79)90111-1.

[113] M. Meyer and J. C. Mialocq. 'Ground state and singlet excited state of laser dye DCM: Dipole moments and solvent induced spectral shifts'. *Optics Communications* 64.3 (1987), pp. 264–268. DOI: 10.1016/0030-4018(87)90390-7.

[114] G. Lavoie, J. Heywood and J. Keck. 'Experimental and Theoretical Study of Nitric Oxide Formation in Internal Combustion Engines'. *Combustion Science and Technology* 1.4 (1970), pp. 313–326.

[115] Y. Zeldovich. 'The Oxidation of NItrogen in Combustion Explosues'. *Acta Physicochimica, U.S.S.R.* 21 (1946), pp. 577–628.

[116] P. G. Handbook, D. E. Library and T. M.-h. Companies. 'Gas turbine combustors' (2004).

[117] J. Kiefer, A. L. Sahlberg, D. Hot, M. Aldén and Z. Li. 'Misalignment Effects in Laser-Induced Grating Experiments'. *Applied Spectroscopy* 70.12 (2016), pp. 2025–2028. DOI: 10.1177/0003702816653128.

[118] T. B. Settersten, B. D. Patterson and W. H. Humphries IV. 'Radiative lifetimes of NO A2Sigma+ (v'=0,1,2) and the electronic transition moment of the A2Sigma-X2Pi system'. *Journal of Chemical Physics* 131.2009 (2009), pp. 1–11. DOI: 10.1063/1.3227520.

[119] S. O'Leary and P. Ewart. 'Absorption and saturation effects on degenerate four-wave mixing in excited states formed during collisions'. *Journal of Physics B : Atomic and Molecular Physics* (1984).

[120] A. Luers, A.-L. Sahlberg, C. Willman, B. Williams and P. Ewart. 'Optical measurement of gas pressure using laser induced grating spectroscopy in nitric oxide'. *In Preparation* (2017).

[121] E. Lemmon, M. Huber and M. McLinden. *NIST Standard Reference Database 23: Reference Fluid Thermodynamic and Transport Properties Database-REFPROP*. Tech. rep. Gaithersburg, 2013. DOI: http://dx.doi.org/10.18434/T4JS3C.

[122] A. Luers, A.-L. Sahlberg, S. Hochgreb and P. Ewart. 'Flame thermometry using laser induced grating spectrosopy of nitric oxide'. *Applied Physics B* ().

[123] S. Gordon and B. McBride. *Computer Program for Calculation of Complex Chemical Equilibrium Compositions and Applications*.

[124] Z. W. Sun, Z. S. Li, B. Li, Z. T. Alwahabi and M. Aldén. 'Quantitative C2H2 measurements in sooty flames using mid-infrared polarization spectroscopy'. *Applied Physics B: Lasers and Optics* 101.1-2 (2010), pp. 423–432. DOI: 10.1007/s00340-010-4057-z.

[125] Z. W. Sun, Z. S. Li, A. A. Konnov and M. Aldén. 'Quantitative HCN measurements in CH4/N2O/O2/N2 flames using mid-infrared polarization spectroscopy'. *Combustion and Flame* 158.10 (2011), pp. 1898–1904. DOI: 10.1016/j.combustflame.2011.03.008.

[126] G. Sutton. *The NPL Standard Flame*. Tech. rep. Hampton Road, Teddington, Middlesex: National Physical Laboratory (NPL), 2016.